EPFL

Thèse n° 9398

Investigation of Lead-free perovskites for Optoelectronic Application

Présentée le 29 octobre 2021

Faculté des sciences de base
Groupe SCI SB MN
Programme doctoral en science et génie des matériaux

pour l'obtention du grade de Docteur ès Sciences

par

Alexander FEDOROVSKIY

Acceptée sur proposition du jury

Prof. C. Hébert, présidente du jury
Prof. M. K. Nazeeruddin, directeur de thèse
Dr V. Shvartsman, rapporteur
Prof. P. Gao, rapporteur
Prof. J.-E. Moser, rapporteur

École
polytechnique
fédérale
de Lausanne

2021

Acknowledgments

Prof. Mohammad Khaja Nazeeruddin

Thank you for becoming my thesis director and allowing me to receive valuable and independent research experience during my doctoral study in EPFL.

Prof. Giulia Grancini

Thank you for guiding me during the start of my doctorate and for further great research help.

Dr. Nikita Drigo, Dr. Valentin Queloz, Nadja Klipfel, Dr. Albertus Sutanto, Cansu Igci, and Mousa Abuhelaiqa

Thank you for an endless number of discussions, advice, help, and fun. I am grateful that you were my comrades and friends in the doctorate.

Dr. Cristina Roldán Carmona, Dr. Maria Cristina Momblona Rincón, Dr. Hiroyuki Kanda, Dr. Iwan Zimmerman, Dr. Hobeom Kim, Dr. Bin Ding, Dr. Robin Humphry-Baker, and Dr. Keith Gregory Brooks

Thank you for your guidance and help as senior researchers.

Ms. Isabel Wild and Ms. Géraldine Gfeller

Thank you for your work and support in all questions about paperwork.

All staff members of the EPFL Valais

Thank you for your help. The research would not be possible without your everyday work.

All scientific visitors and ex-colleagues who I did not mention above

Thank you for the great experience and knowledge exchange.

Dr. Mikhail Bunin

Thank you for your leadership during my first steps in science and all following consultations.

My family and friends

Thank you for your support in any kind of situation.

My thesis committee members

Thank you for your time to evaluate my thesis. I would appreciate any feedback from you.

All other collaborators, colleagues, and teachers

Thank you for all knowledge and experience that you ever shared with me.

Abstract

The search for new energy sources and materials is at the foundations of scientific and technological progress. These two, often interconnected, fundamental elements open a way to create novel designs and improve existing ones for all types of machines and devices.

Perovskite solar cells (PSCs) are a great example of this kind of system. Achievements in halide perovskite materials research made a remarkably rapid growth of energy conversion efficiency in PSC technology possible. In turn, a manufacturing process for the technology is potentially cheaper and more straightforward (relative to Si-based). As a result, the PSCs can be a solid background for producing the next generation of solar cells.

However, unfortunately, PSCs are still not ready for a market, primarily because of three problems: large-scale production, stability, and toxicity. The first problem is mainly a result of the rawness of the technology, requires mostly resolving engineering tasks, and is not a fundamental barrier. The second problem – stability has a deeper connection to the properties of the material itself. The nature of degradation processes in PSCs is not completely clear. Still, different studies have found some promising ways to stabilize PSCs for a range of thousands of hours. Thus, a combination of engineering and material research can solve this problem, despite its deeper basis.

The third problem, toxicity, is a fundamental property of the high efficient PSCs because of its lead-based compound. Lead is one of the critical components of halide perovskites used in the technology, and at the same time, this metal has confirmed toxicity. The water solubility of lead in halide perovskites (primarily as PbI_2 and $PbBr_2$) complicates the situation for the whole lifecycle of the devices - from production to recycling. The toxicity of the materials used in PSCs can affect one of the main goals of solar energy: to be produced safe, clean, and sustainable.

Taking into account these facts, I focused this thesis on searching for lead-free alternatives for PSCs.

Initially, I focused on searching for a model to predict promising vacancy-ordered double perovskites' formability as part of initial screening. I demonstrated the applicability of the geometrical approach based on Goldschmidt's Tolerance Factor for a simple, easy-to-use formability prediction technique for this class of materials. During this part of the study, I also demonstrated a difference between using the method for classic and vacancy-ordered perovskites.

In the next part, I used a novel approach based on deep learning to design a new model of perovskite formability. As a result, I successfully forecast perovskite formability with an accuracy of over 98% for the best case. Moreover, I found that the resulting models were able to find some inaccuracies in the original data.

Following, I synthesized and researched the structure and properties of tellurium-based vacancy-ordered perovskites. During the research, I found an unexpected complex situation of the optical gap determination for the materials. To solve this challenge, I demonstrated different approaches of absorption spectra fitting and cross-referenced it with other experimental data.

Keywords

Photovoltaic, perovskites, perovskite solar cells, lead-free perovskites, vacancy-ordered perovskites, machine learning, deep learning, tellurium-based perovskites, crystal formability prediction, structure prediction, band gap determination.

Résumé

La recherche de nouvelles sources d'énergie et de nouveaux matériaux est à la base du progrès scientifique et technologique. Ces deux éléments fondamentaux, souvent interconnectés, ouvrent la voie à la création de nouveaux modèles et à l'amélioration des modèles existants pour tous les types de machines et de dispositifs.

Les cellules solaires à pérovskite (PSC) sont un excellent exemple de ce type de système. Les progrès réalisés dans la recherche sur les matériaux pérovskites à base d'halogénure ont permis une croissance remarquablement rapide de l'efficacité de la conversion énergétique dans la technologie PSC. En retour, le processus de fabrication de cette technologie est potentiellement moins cher et plus simple (par rapport à celui basé sur le Si). Par conséquent, les PSC peuvent constituer une base solide pour la production de la prochaine génération de cellules solaires.

Cependant, les PSC ne sont malheureusement pas encore prêts à être commercialisés, principalement en raison de trois problèmes: la production à grande échelle, la stabilité et la toxicité. Le premier problème résulte principalement du caractère rudimentaire de la technologie, il nécessite essentiellement la résolution de tâches d'ingénierie et ne constitue pas un obstacle fondamental. Le deuxième problème - la stabilité - est davantage lié aux propriétés du matériau lui-même. La nature des processus de dégradation dans les PSC n'est pas complètement claire. Néanmoins, différentes études ont trouvé des moyens prometteurs de stabiliser les PSC pendant des milliers d'heures. Ainsi, une combinaison d'ingénierie et de recherche sur les matériaux peut résoudre ce problème, malgré sa base plus profonde.

Le troisième problème, la toxicité, est une propriété fondamentale des PSC à haut rendement en raison de leur composition à base de plomb. Le plomb est l'un des composants essentiels des pérovskites d'halogénure utilisées dans la technologie, et en même temps, ce métal a une toxicité confirmée. La solubilité

dans l'eau du plomb dans les pérovskites halogénures (principalement sous forme de PbI_2 et $PbBr_2$) complique la situation pour l'ensemble du cycle de vie des dispositifs - de la production au recyclage. La toxicité des matériaux utilisés dans les PSC peut affecter l'un des principaux objectifs de l'énergie solaire : être produite de manière sûre, propre et durable.

En tenant compte de ces faits, j'ai concentré cette thèse sur la recherche d'alternatives sans plomb pour les PSCs.

Dans un premier temps, je me suis concentré sur la recherche d'un modèle permettant de prédire la formabilité des pérovskites doubles ordonnées à vacance prometteuses dans le cadre d'une sélection initiale. J'ai démontré l'applicabilité de l'approche géométrique basée sur le facteur de tolérance de Goldschmidt pour une technique de prédiction de la formabilité simple et facile à utiliser pour cette classe de matériaux. Au cours de cette partie de l'étude, j'ai également démontré une différence entre l'utilisation de la méthode pour les pérovskites classiques et les pérovskites à vacance ordonnée.

Dans la partie suivante, j'ai utilisé une nouvelle approche basée sur l'apprentissage profond pour concevoir un nouveau modèle de formabilité des pérovskites. En conséquence, j'ai réussi à prévoir la formabilité des pérovskites avec une précision de plus de 98 % pour le meilleur cas. De plus, j'ai constaté que les modèles résultants étaient capables de trouver certaines inexactitudes dans les données originales.

Ensuite, j'ai synthétisé et étudié la structure et les propriétés des pérovskites à base de tellurium à vacance ordonnée. Au cours de la recherche, j'ai trouvé une situation complexe inattendue dans la détermination de la bande interdite optique pour les matériaux. Pour résoudre ce problème, j'ai démontré différentes approches d'ajustement des spectres d'absorption et les ai croisés avec d'autres données expérimentales.

Mots-clés

Photovoltaïque, pérovskites, cellules solaires en pérovskite, pérovskites sans plomb, pérovskites à vacance ordonnée, apprentissage automatique, apprentissage profond, pérovskites à base de tellure, prédiction de la formabilité des cristaux, prédiction de la structure.

Table of Contents

List of figures and tables

Chapter 1. Introduction

1.1 Energy, materials & perspectives

Throughout the complete history of humankind, discoveries of new materials and energy sources were the engine of all the most significant achievements of technological progress. It is difficult to overemphasize their importance: from using simple campfires in ancient times to giant solar farms and perspectives of controllable fusion in the near future, from using woods and stones to nanocomposites and complex semiconductor materials, the complete historical epochs were named because of materials, and these materials were fabricated thanks to available energy sources.

We can consider civilization progress as a constant process of energy consumption growth. The level of available technologies at a single point in time perfectly correlates to the available amount of energy production, transmission, distribution, and use.[1] Moreover, we can connect current perceptions about the future of the progress with the future increase of energy consumption, e.g., the Kardashev scale.[2]

In parallel, the production of new materials might require increasing energy use. Growing demands to all life cycle steps from ingredients purification to recycling need support via extra energy.

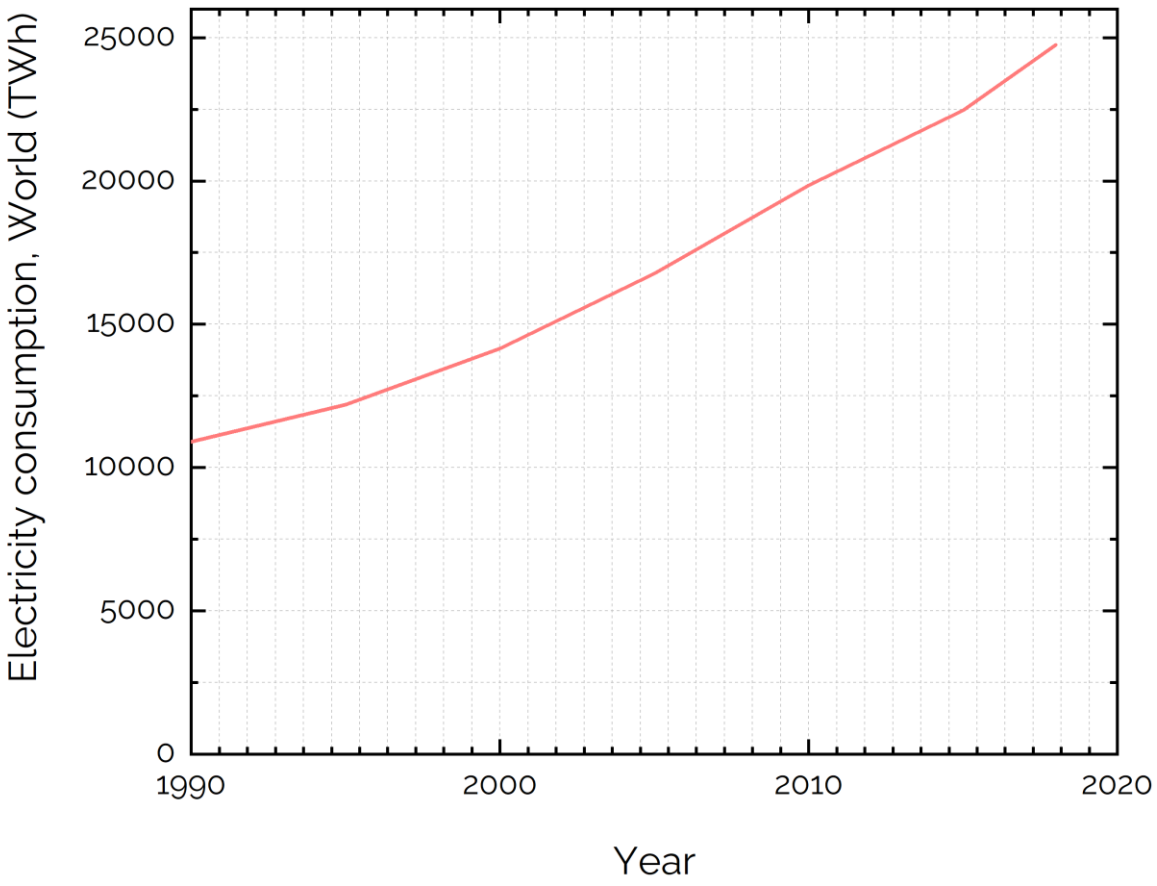

Figure 1. The world electricity consumption.[3]

According to the International Energy Agency (IEA), the world electricity consumption reached 24738.9 TWh in 2018 (Figure 1). Following IEA's Stated policies scenario, the total energy demand will increase by ~10% with a growing share of electricity (up to 21%).[4,5] At the same time, the real growth rate of electricity consumption for the last 10 years (2008-2018 period) was about 32% (Figure 1).[3] Based on that, the approximate growth of electricity consumption only during the next decade will require extra supply from ~2500 TWh to ~7500 TWh.

Fossil-based generating capacity nowadays makes up more than 65% of the total electricity supply (Figure 2), and it corresponds to around one-third of CO_2 emissions.[3] Regarding Yangyang Xu et al. and the Intergovernmental Panel on Climate Change (IPCC), the process of global warming might have an acceleration character.[6,7] The IPCC special report on the impacts of global warming of 1.5 °C shows that the difference between 1.5 °C and 2 °C increases in temperature will at least redouble the number of people with water shortage.

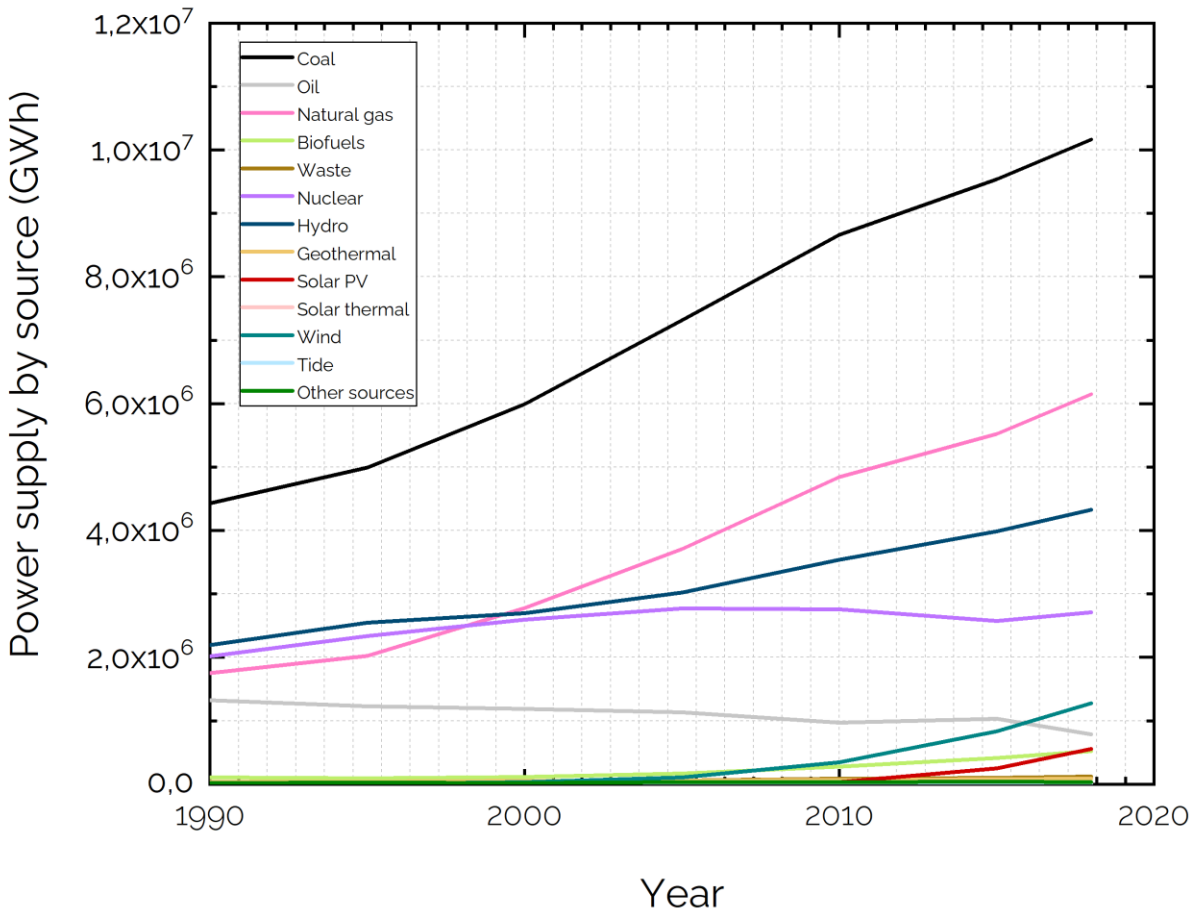

Figure 2. The world electricity generation by source.[3]

These facts show need not only to minimize extra emissions from new power sources but also to look for a way to replace widely used fossil fuels in the generation sector.

Modern research of carbon-free energy sources has two big branches: nuclear energy and renewable energy sources.

Nuclear energy, despite many positive aspects, has some substantial limitations. For example, scalability - most existing fission reactors require an expensive and large-scale infrastructure, which limits their use only for regions with a high-density population or industry hubs. The problematic reputation of nuclear technology within society and the necessary disposal of atomic waste might also be a source of problems. However, one of the more severe difficulties is the limitation of available fission fuel.[8] Fusion-based nuclear energy is still not available, and, unfortunately, the research progress in this topic does not have a precise forecast.[9]

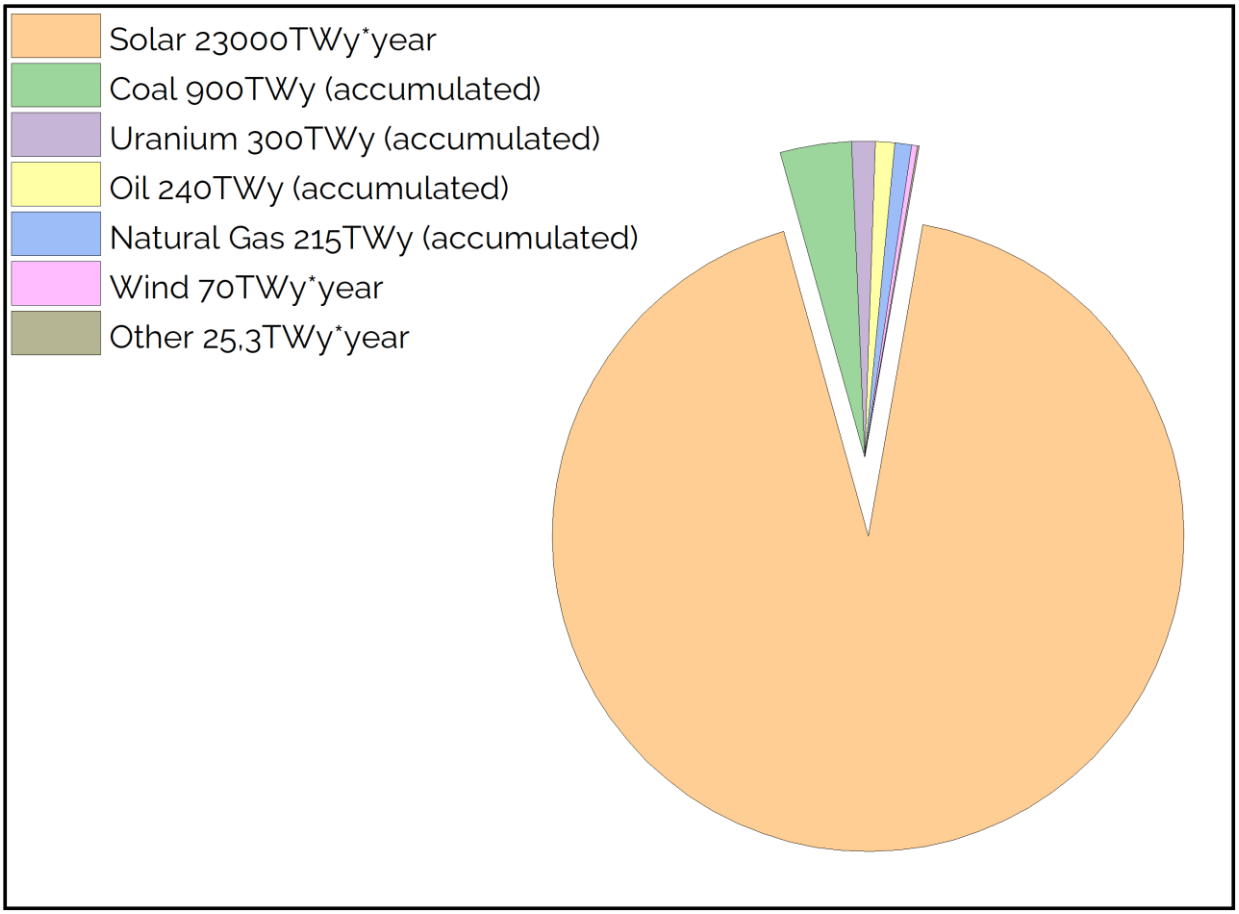

Figure 3. Available energy sources.[8]

Among renewable energy sources, solar energy has the most extensive available potential (~23000TWy).[8] Generators based on solar energy can be located independently from the grid. It is possible to integrate them into existing constructions (e.g., roofs), and they can be used for a broad scaling from wearable devices to large power plants and more.[10,11]

Solar energy also has many deficiencies. I would like to highlight the most critical ones, such as instability over time (day and year cycles, weather dependency), what leads to the necessary use of batteries, and the relatively low " energy return on investment" (EROI) index. Besides, the limitations might include occupation of large areas, panels cleaning, aesthetic impact on the landscape, etc.

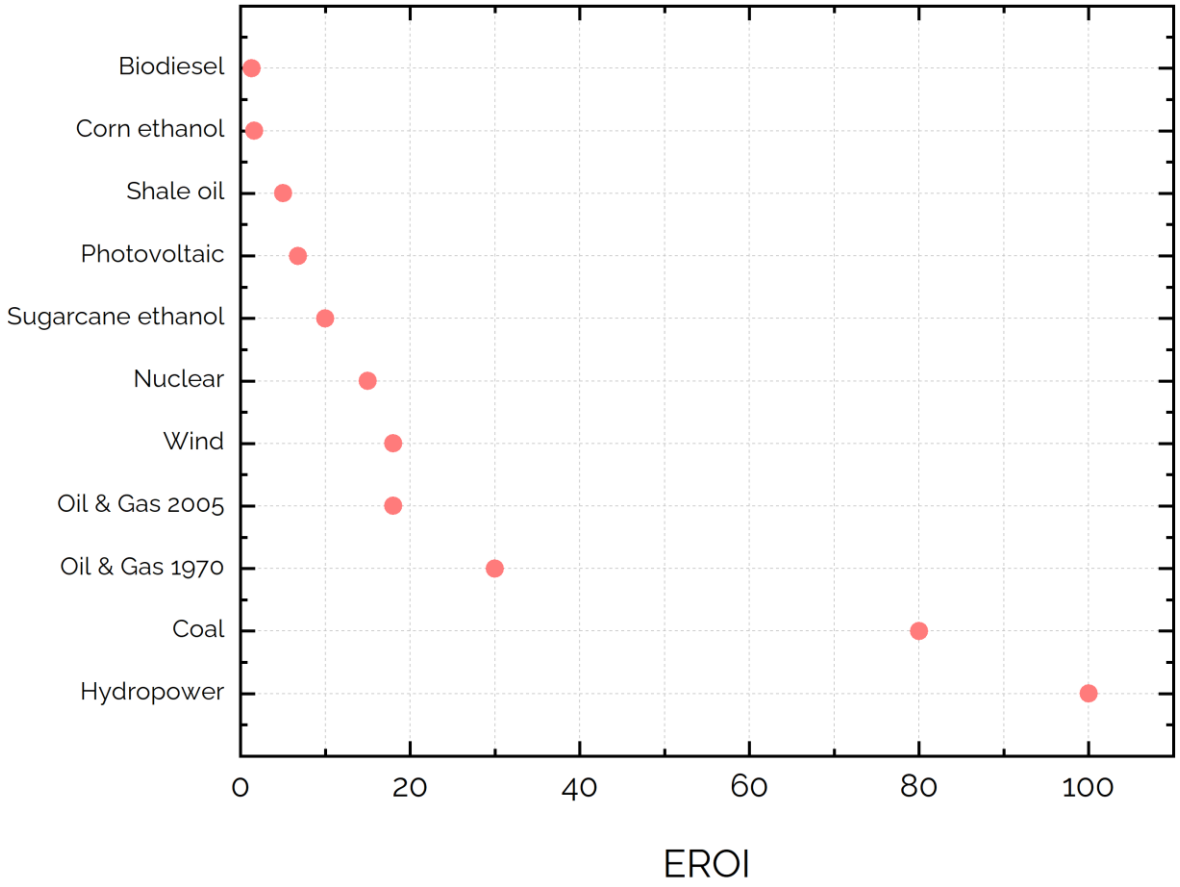

Figure 4. EROI indexes for various energy sources.[12]

Based on the above problems, most research in solar energy is related to increasing the EROI index and reducing price via improvement of the design of solar energy-based generators and the optimization of the manufacturing processes. Most of these studies are related to material sciences and photovoltaic (PV) topics. First, I would like to introduce the solar energy principles in the next section to discuss them in detail.

1.2 Solar energy

The concept of solar energy is to convert the energy of solar radiation to usable form, generally energy of chemical bonds, heat, or electricity.

Accumulation of energy of light via the formation of chemical bonds is the basis of the photosynthesis process. Photosynthesis in living organisms is the essence of complex life on Earth and the primary source of many fuels, from woods to fossils. Production of some organic fuels, e.g., biodiesel, is based on using natural

photosynthesis. Unfortunately, the efficiency of the process is limited to 8-9% at optimal conditions.[13] Such a low conversion rate is especially critical, considering losses at converting organic fuels to electricity. There are many ongoing studies about artificial photosynthesis to increased efficiency; however, their results and application usage are a question of the future.[14]

Also, the generation of hydrogen fuel by using sunlight is a part of the branch. Sustainable hydrogen-based energy systems have many advantages, and direct conversion of solar energy to hydrogen fuel looks like a perspective target.[15] Unfortunately, like photosynthesis, the efficiency of energy conversion is small: only up to 7.8% for photoelectrolysis and less for other direct light-to-hydrogen methods.[16] Associated losses during hydrogen usage make the situation worse.

Solar thermal energy is widespread around the globe. Devices such as solar water heaters, steam generators, ovens, etc., have a small price and are relatively effective, especially in regions located at lower latitudes. Concentrated solar power (CSP) is one of the ways to generate electricity from sunlight. CSP is based on using a heat engine powered by heat converted from sunlight energy. Its conversion efficiency of light energy to electricity in real-world cases might achieve up to 30%, but most are in the range of 7-20%.[17] CSP power plants have high sensitivity to unstable weather and require a high-scale size to achieve efficiency. However, they found its application in dry lower latitude regions, and cumulative generation capacity has a trend to grow.[18]

Photovoltaic (PV) is a technology for direct energy conversion of sunlight into electricity based on using photovoltaic. The fundamental principle of the photovoltaic effect is generation free carriers by excitation of electrons via the energy of absorbed photons. However, only the photovoltaic effect is not enough for power generation. The design of solar cells also includes a mechanism for separating carriers with different charge signs.

A wide variety of absorber materials from solid-state monocrystals like Si to organic polymers makes it hard to describe and completely understand all physicochemical phenomena behind the photovoltaic effect.

Theoretical efficiency limit of PV energy conversion depends on a light source: its size (or using light concentrator), its optical spectrum peculiarities, etc. As standard, the sunlight conditions are defined by spectra of the sun, the intensity at a distance to Earth (1 AU), and the light conditions depending on the equivalent air mass (AM).

In that case, theoretical limits of PV efficiency in thermodynamics are 86.8% for concentrated and 68.7% for non-concentrated sunlight radiation (in case of the light source equal to the size of the sun on the sky and multi-junction device).[19–21] Of course, the current practical limits are far from these values. In the case of a single-junction device, the Shockley–Queisser limit (Figure 5) is up to around 33.7% for typical sunlight conditions (non-concentrated, AM 1.5).[22]

Based on NREL data, today's efficiency records are 29.1% for single-junction cells (GaAs thin-film crystal technology) and 47.1% for six-junctions cell (III-V technology).[23] In the case of modules, the highest recorded efficiencies are 25.1% for single-junction GaAs module (800-6500cm^2) and 40.6% for hybrid four-junction module (area 200-800cm^2).

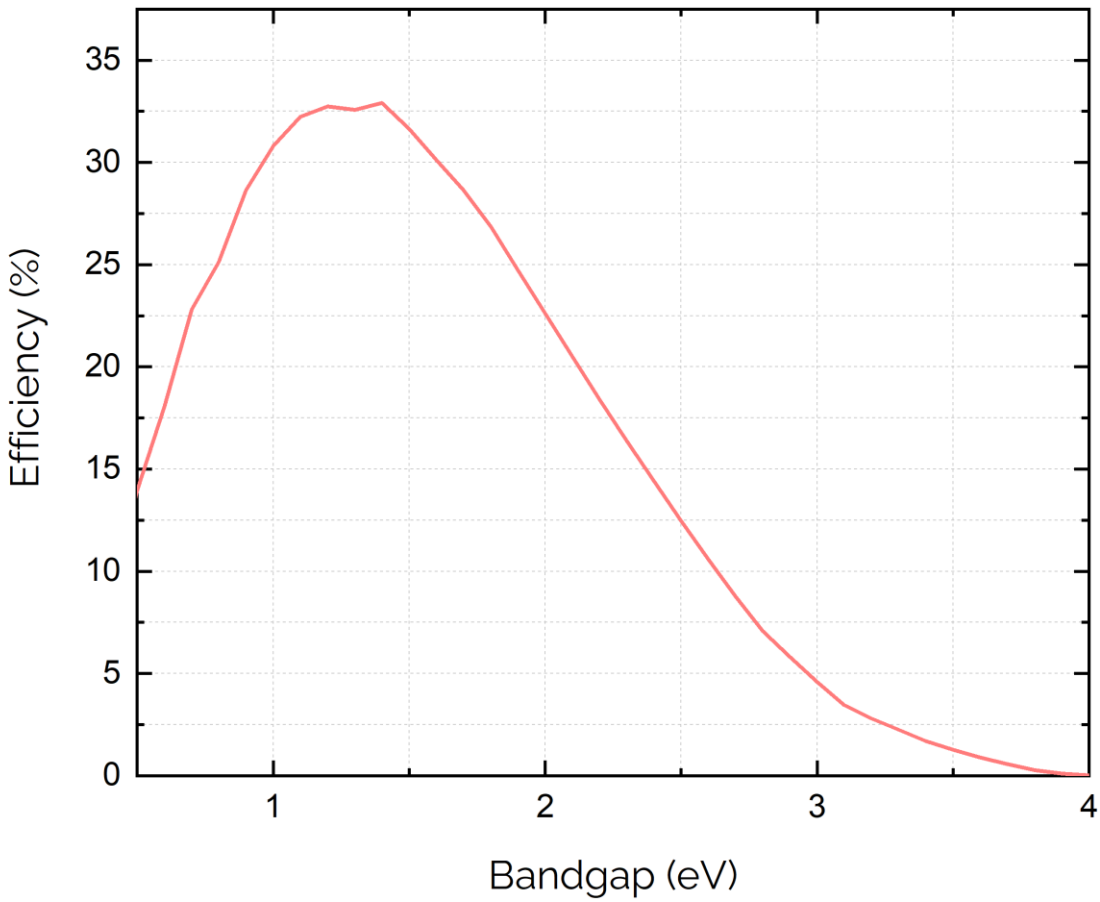

Figure 5. Shockley–Queisser efficiency limit for single-junction solar cells.[24]

Despite the efficiency values approaching the theoretical barrier in single-junction cells, other parameters should also be considered. In the case of using PV as a regular power source, stability, and conventional power per price and EROI, are equally important. In some cases, e.g., using on transport on limited areas, power per mass (kW/kg) and power per surface (kW/m^2) might be critical. Besides, targeted economic sustainability requires reducing limited resource usage, improving the manufacturing process's environmental friendliness, and recycling-friendly device designing.

Unfortunately, none of the modern PV technologies can fit all of the above requirements. Therefore, searching for the optimal materials and solar cell design to suit the needs is a fundamental target for PV research.

1.3 Perovskites & perovskite solar cells

In recent years, halide perovskites have shown great potential in the optoelectronic field, especially in the role of materials for solar cells and light-emitting diodes.[25,26] Perovskite solar cells (PSCs) have amazing fast progress from 4% in 2009 to the highest recorded efficiency 25.5% today.[23,25]

PSC technology is an evolution of dye-sensitized solar cells, where crystalline halide materials with perovskite and perovskite-like crystal structures replaced dye and electrolyte.[27]

Perovskite is a typical crystal structure with general structure ABX_3 initially described for $CaTiO_3$ minerals. Figure 6a demonstrates perovskite unit cell in the "ideal" cubic case (space group $Pm\bar{3}m$). However, cubic perovskites are relatively rare, and orthorhombic (e.g., $Pnma$) and tetragonal (e.g., $I4/mcm$) are common non-cubic variants (Figure 6b, 6c). Perovskite might undergo temperature-induced phase transitions between noted phases but not limited to.[28,29]

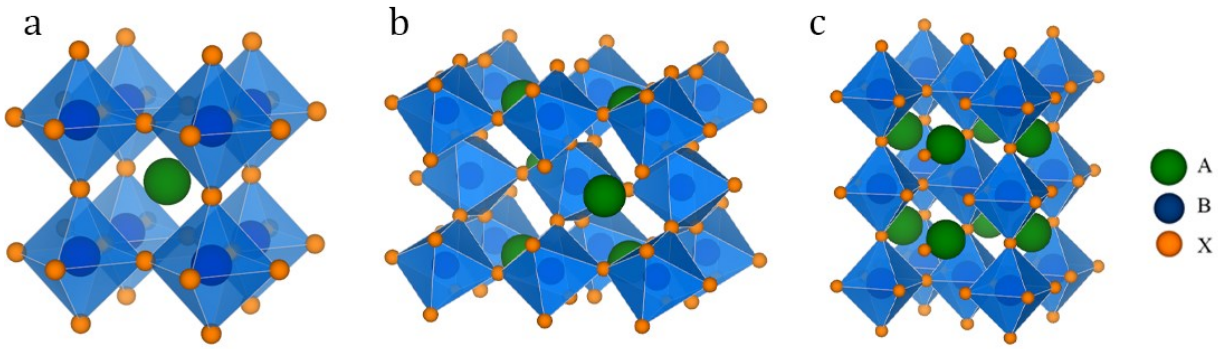

Figure 6. Examples of perovskite unit cells. a) Ideal cubic $Pm\bar{3}m$ unit cell, b) orthorhombic $Pnma$ unit cell, c) tetragonal $I4/mcm$

PSC is not the first technology that uses materials with this type of structure. Early, perovskites structures (primarily oxides) have widely used solid-state electrical devices, e.g., capacitors, piezo elements, sensors, etc.[30,31]

In PSC, there is a massive variation of compounds, from full inorganic to hybrid metal-organic crystals.[32,33] Actually, it makes it possible to tune properties such as bandgap width, which is an excellent advantage of the technology.

Another critical benefit of using the halide perovskites in PSC is a remarkably high level of defect tolerance, which simplifies manufacturing. The concept of defect tolerance identifies materials that are insensitive to charge localization due to intrinsic defects.[34] It is one of the essential properties of $APbX_3$ compounds.[35] Using a solution-based deposition process and the relatively low costs of most precursors complement the advantage.

The sum of high energy conversion efficiency and noted advantages stipulates the application potential of PSCs. But unfortunately, PSCs also have a list of significant unresolved problems. We can highlight three of them.

The first one is the scalability problem. The efficiency values noted above relate to a small effective area of a PSC (few square millimeters).[23] Chart for scaled-up modules displays lower values.[36] Scaling the manufacturing process and its optimization is a task of engineering masterpieces and does not have a fundamental barrier. Some recent studies showed successful producing enough big and effective perovskite-based modules using industrial methods such as spraying, roll-to-roll, and slot-die.[37,38] It is expected that this problem will be solved entirely in the near future by design a few alternative industrial-scale manufacturing protocols.

The second problem is the live-time stability of PSC. Instability (expressed in efficiency drop over time) is related to the properties of the perovskite material itself. The nature of the degradation processes is not completely clear yet. Some publications report the fundamental thermodynamical origin of halide perovskites instability.[39,40] Different researchers have found some promising ways to stabilize PSCs for a range of thousands of hours with an acceptable drop of efficiency. Most of these ways are based on complex design and optimization of PSC layers, such as adding extra layers of low-dimensional perovskites and surface passivation.[41,42]

Also, searching for high-stable hole & electron transport materials (HTMs, ETMs) displays progress in the stabilization of cells. In this way, a combination of engineering and material research has a chance to solve this problem, despite its deeper basis.

The third problem is toxicity. All high-efficient PSCs are lead-based ($APbX_3$), and this is compounded by the water-solubility/degradation of the halide perovskite compounds and their precursors (mostly PbI_2 and $PbBr_2$) with higher toxicity.[43,44] At the current stage of research, lead in the perovskite compound is an integral component. As a result, lead-induced toxicity is a fundamental property of existing high-efficient PSCs.

1.4 Scale of the lead problem

Lead is noted as "forbidden" or "limited to use" in an extensive list of countries that include Switzerland & the European Union.[45,46]

It's easy to show the scale of the lead problem for PSCs. Calculation of the total primary energy supply forecast ~146 PWh by 2040th.[3] Equivalent power through the year is ~18TW. To cover it only by solar energy, need to use surface ~$7{,}85 * 10^{11}\ m^2$ (With power conversion efficiency ~8%. This efficiency shows the total harvest by power plants, and it should include total losses, e.g., transportation, solar modules efficiency drop under dust, service space between modules, etc.).[47,48]

To understand the scale of the lead in a perovskite solar cell better, first, it is necessary to calculate how much lead is used in a lead-based perovskite solar cell with a surface of 1 m^2 (for example, solar cell-based at $(CH_3NH_2)PbI_3$). The thickness of the perovskite layer ~300nm, the density of $MAPbI_3$ perovskite ~4.22 g/cm^3, lead mass is 37,8%.[49,50] As a result, we can easily calculate and see that 1 m^2 of perovskite solar cells contains ~ 0,48 g of lead. To cover all necessary surfaces, we have to use $3{,}8 * 10^8$ kg. That mass is enough to exceed the safety limit of lead for $3{,}8 * 10^5\ km^3$ of water.[51] It is more than all easy-accessible sources of fresh water (rivers and lakes).[52]

The calculation is truly optimistic - it shows the amount of lead in case of a small thickness of the perovskite layer, 100% efficiency of the production process; also, we ignored the necessity of solar panels periodical renew. Moreover, precursor and breakdown product PbI_2 shows much higher toxicity.[53] In addition, it does not include the possible use of lead-based perovskites to produce LED and other optoelectronic devices.

1.5 Materials screening

The only way to solve the toxicity problem is by searching for novel environmentally friendly materials suitable for PSC or PSC-like technology. Noted above fast progress in PSC based on halide perovskites and a goal to save most of the advantages of the lead-based halide perovskites were arguments to search for novel lead-free compounds inside perovskite & perovskite-like class of materials.

To date, more than 1622 distinct crystals with perovskite structures (classic and double) have been described.[54] Forecast based on known crystal structures and geometrical factors gives ~100000 unknown compounds that might have perovskite structure.[54] It means that only ~1.6% of all perovskite compounds are known to date.

The great number of potential candidate materials is an amazing opportunity for research, but screening such a big number of compounds is a challenge. Synthesis and experimental characterization for all of them require incredible and practically unavailable resources.

The approach noted above is not the only one. Many publications show results based on elaborate ab initio methods, e.g., density functional theory (DFT), molecular dynamics (MD), etc.[55–57] However, these methods demand considerable computing resources and may require individual consideration for each compound. Such complex and resource-intensive calculations are often performed at the middle and final stages of research; their use makes no sense for a wide search for unknown substances.

Based on these facts, I focused a significant part of the thesis on searching for new moderately simple ways to forecast the structure of potentially interesting compounds and to limit the number of candidates for the future experimental check.

1.6 Motivation

The above-stated concepts and problems are the basis of my motivation for the study made in the thesis. The global objective was to search for novel environmentally friendly materials that could display high performance for photovoltaic applications.

To reach this aim, I have analyzed existing experimental data by using geometrical factors and deep learning techniques. As well, I have chosen an experimental checklist of Te-based vacancy-ordered perovskite-like compounds as the target materials.

1.7 Thesis outline

In the second chapter, I demonstrated the possibility of using Goldschmidt's tolerance factor t for the prediction formability of vacancy-ordered perovskite-like compounds. I described the similarities and differences of the approach relative to classic ABX_3 perovskites.

In the third chapter, I displayed an extension of a simple geometrical approach based on t factor and octahedral factor μ to an n-dimensional analysis of compounds' features via deep learning for prediction formability ABX3 perovskites (halides and oxides).

In the fourth chapter, I described an experimental trial of some vacancy-ordered Te-based perovskite-like candidate materials for optoelectronic application. I approach the question of their synthesis, thin film deposition, and characterization.

Chapter 2. The role of Goldschmidt's tolerance factor in the formation of A_2BX_6 double halide perovskites and its optimal range

Abstract

Vacancy-ordered double perovskites is a new branch of lead-free halide perovskites with properties promising for photovoltaic application. In this study, data about the crystal structure of 170 known A_2BX_6 ($X = I, Br, Cl, F$) were collected and analyzed to solve a question of applicability the Goldschmidt's tolerance factor & octahedral factor to double perovskites. It was found that Goldschmidt's tolerance factor is applicable for double perovskites in analog with ABX_3 perovskites. Suggested optimal ranges of Goldschmidt's factor expand the geometrical approach from ABX_3 perovskites to of A_2BX_6 double perovskites. The result is useful for up to 796 new full inorganic compounds having double perovskite structure and design new hybrid organic-inorganic double perovskites.

This chapter is based on the following published article:

Fedorovskiy, Alexander E., Nikita A. Drigo, and Mohammad Khaja Nazeeruddin. "The role of Goldschmidt's tolerance factor in the formation of A_2BX_6 double halide perovskites and its optimal range." Small Methods 4.5 (2020): 1900426. DOI: 10.1002/smtd.201900426

In this work, I collected and analyzed data for all the discussed compounds. Nikita Drigo consulted and supported the process of the study, Mohammad Khaja Nazeeruddin supervised the process.

2.1 Introduction

Over the last few years, halide perovskites have become a hot topic in the field of optoelectronics. From first publication to today, research achieved results up to 23.7% of power conversion efficiency (PCE) of perovskite solar cells[25,58] and 21.6% external quantum efficiency (EQE) of perovskite light-emitting diodes.[59] One of the circular reasons for such great results is related to the unique properties of the hybrid halide perovskites: long carrier diffusion lengths[60], panchromatic light absorption[61], and unusually low energy defect physics[62] leads to defect tolerance[63].

In addition, PSCs manufacturing is realizable by low-temperature solution processing techniques using readily available starting materials.[64,65] Thanks to these factors, PSCs have high manufacturability and can be a potential cost-efficient alternative to wide common silicon solar cells.

However, halide perovskites still have three main drawbacks that prevent them from entering the photovoltaic market: scalability, stability, and toxicity.[66] Recent research achieved significant advances in terms of the first two. Various authors reported the fabrication of large-area perovskite cells and small modules using industry compatible methods such as chemical vapor deposition[67], screen-printing[68], inkjet-printing[69], or slot die coating[70]. The stability was improved by using special cell designs such as carbon-based mesoscopic electrodes[71], compositional engineering (including 2D perovskite layers), [42]and molecularly engineered charge extracting materials.[72] However, the toxicity of lead[44] is an intrinsic property of lead-based halide perovskites and affects all stages of the device lifecycle, from production to recycling. The only way to address the lead toxicity is to enter the research of novel lead-free absorber materials based on less toxic elements.

Within this field, among the most researched lead-free perovskites, tin(II) based PSCs demonstrate the highest power conversion efficiencies of 10%.[73] However,

tin(II) is very prone to oxidation[74], which makes these perovskites difficult to process. In addition, oxidation negatively influences their long-term stability. As a result, the search for new materials without these limitations motivates a high interest in halide A_2BX_6 materials having double-perovskite structure.

Before the future discussion, we have to note the confusion of nomenclature in the field. Some authors name A_2BX_6 (K_2PtCl_6 prototype structure) as "vacancy-ordered double perovskite";[75–77] at the same time, there is an opinion that these structures should be named as perovskites.[78] Moreover, $A_2B'B''X_6$ are also named as double perovskite.[77–79]

In the text below, we name and discuss as "double perovskite" only A_2BX_6 compounds with K_2PtCl_6 prototype structure due to the fairly similar disposition of $[BX_6]$ octahedrons and A cations and their potential application as a lead-free version of lead-based halide perovskite. However, we concede that it is a premise for future correctly renaming "perovskite-like" systems include the object of our research.

As calculated by Cai et al. wide range of bandgap values[80] for double perovskites and recent publications with experimental data have suggested new A_2BX_6 materials for photovoltaics. Briefly, Cs_2TiBr_6 displays moderate efficiency of about 3% and excellent device stability – less than 15% efficiency drop over 350 hours of environmental stress.[76] A_2TeX_6 ($A = methylammonium\ (MA)$, $formamidinium\ (FA)$; $X = Br, I$) hybrid compounds have promising properties: optimal tunable bandgaps (1.42-2.02eV), long carrier diffusion lengths (up to 38.19 μm) and high stability in air.[81]

However, these compounds are not ideal for a number of reasons, such as complicated thin-film processing in the case of A_2TiX_6 and non-zero toxicity and high price in case A_2TeX_6. Looking for optimal materials having double perovskite opens a problem of choice.

Until now, the existing data describe ~1622 distinct compounds with the perovskite crystal structure (including classic ABX_3 and double A_2BX_6 perovskites).[54] At the same time, according to the last prediction, as many as ~90000 materials potentially have a perovskite structure.[54] It means that nowadays, only ~1.8% of all perovskites are known.

Figure 7 illustrates ABX_3 and A_2BX_6 perovskite structures. Relative to regular perovskite, double perovskite has 50% periodic vacancies on the $[BX_6]^{-2}$ octahedrons positions (it's a reason to name double perovskite structure "vacancy ordered").[82,83]

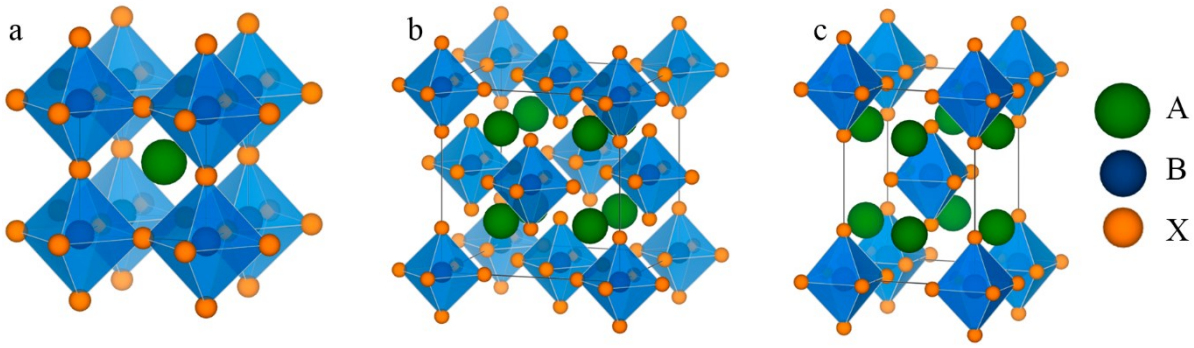

Figure 7. Comparison of crystal structures. (a) 'Classic' ABX_3 perovskite, (b) Cubic double A_2BX_6 perovskite, (c) Disorder double A_2BX_6 perovskite. Double perovskites have high-symmetric cubic[84] and disordered[82] phases. In analog with 'classic' perovskites, disordered double perovskites(c) might demonstrate phase transition to cubic double perovskites (b) with increasing temperature.[85,86]

Experimental research or high-quality simulations are demanding for such a large number of compounds. Reducing the complexity of choice and limiting the number of compounds potentially interesting for optoelectronics is a reason to look for an empirical prediction of double perovskites structural parameters. Here we are interested in the evaluation of the geometrical factors: Goldschmidt's tolerance factor ($t = (r_A + r_X)/(\sqrt{2}[r_B + r_X])$[87] and octahedral factor ($\mu = r_B/r_X$)[88] (where r_A, r_B, r_X are ionc radii for ions in A, B, X sites). Derived from simple geometrical principles, they are useful parameters for any new materials with targeting

perovskite structure as an easy way for basic formability prediction. Li et all. shown for "classic" ABO_3 & ABX_3 perovskites that t factor is a necessary condition to form perovskite structures and this factor has an optimal range.[88,89] Together with μ they limit stability region that used to predict formability of ABX_3 with accuracy of 96%.[89] In result, the approach with using geometrical factors has wide range of use.[66,90] In the same manner, Gregor Kieslich et al. extended this approach for organic-inorganic ABX_3 compounds.[91]

However, the applicability of t and μ factors for A_2BX_6 halide perovskites have never been widely discussed and so far limited.[82,92–95] Information about the applicability of the geometrical factors are limited to A_2BO_6[96] and in a few cases, to $A_2B'B''X_6$.[82,92–95] Importantly, the lack on the existence of a theoretical model on this family limits their synthesis and study to a labor-consuming trial and error approach. As a result, the research into looking for new materials having double perovskite structure is slowed down.

The difference between classic and double perovskites opens the following question: Are t and μ geometrical factors valid for A_2BX_6 double perovskites? If yes, what are their optimal ranges?

In this work, we aim to summarize the existing experimental data about the crystal structure of $A_2^{+1}B^{+4}X_6^{-1}$ ($X = F, Cl, Br, I$) compounds. We define the roles of the geometrical parameters, which govern the formation of potential stable candidates within the family of double-perovskites. In addition, we reveal a number of potentially unknown full-inorganic double perovskites, which can be explored both experimentally and theoretically.

2.2 Results and discussion

To solve the question, 170 compounds A_2BX_6 from ICSD database[97] have been studied. We limited the dataset by defined experimental conditions, which are: data given at atmospheric pressure and room temperature, and listed all these compounds in Table A1.1. Values of effective ionic radii (Ions are 6-coordinate) from Shannon et al.[98]

To clarify, we show an example one of analyzing compounds: K_2SnCl_6 (№89 in Table A1.1). This compound is a bright representative of vacancy-ordered double perovskites with suitable (relative ABX_3) tolerance and octahedral factors ($t = 0{,}9023, \mu = 0{,}3812$). At room temperature, this compound has K_2PtCl_6 prototype structure. [99,100] When cooled, the compound changes crystal structure to disordered: (K_2SnCl_6 prototype at $T = 265K$ and $K_2SnCl_6(LT)$ prototype at $T = 190K$). According to reports [101–104], this type of temperature-induced phase transition is widely distributed in the family of vacancy-ordered perovskites.

Figure 8 presents the number of published A_2BX_6 compounds per different halides ions. The significant difference of explored compounds for different halides might have two different explanations. First, it might be a result of synthesis problems. Jolly[104] noted a trend of increasing synthesis difficulty in the row $F \rightarrow Cl \rightarrow Br \rightarrow I$. Second explanation is related to the abundance of the chemical elements.[105] Chances to get new compounds from an environment (minerals and etc.) are proportional to the abundance of its components. These two possible explanations are not mutually exclusive; the resultant dataset might be a combination of their contributions.

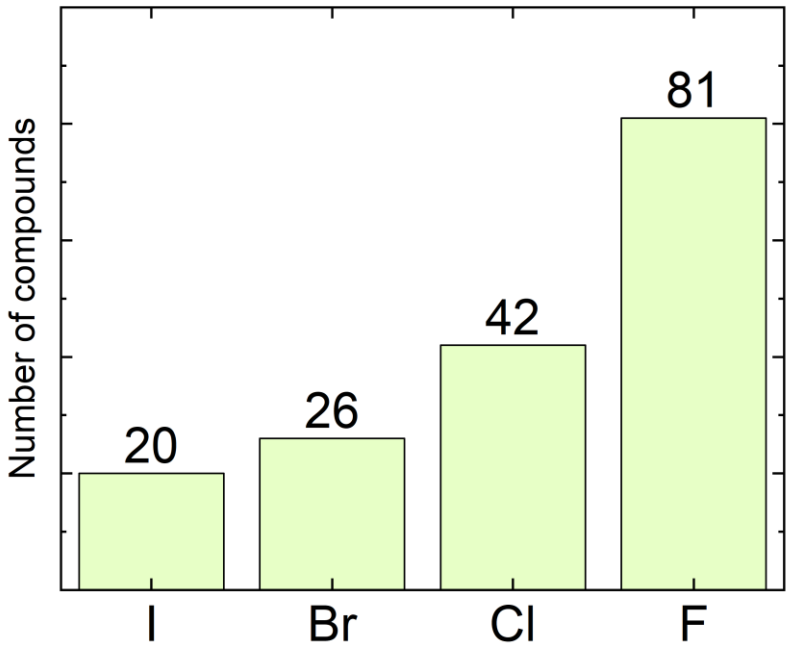

Figure 8. Number of A_2BX_6 compounds per different halides ions.

Figure 9 displays the general structure map in axes of t and μ parameters for A_2BX_6 compounds. Most of cubic (K_2PtCl_6 type) and disordered perovskites (K_2SnCl_6type) is located in the finite stability area (limited by dashed lines). However, the area of perovskites on the structural map is not definitively limited because it has significant overlapping with non-perovskite at borders of perovskite's stability area. Fuzzy boundaries of the double perovskite stability region are not able to clearly determine optimal ranges of the geometrical factors as it was done by Li et al. for ABX_3 perovskites.[89] On the other hand, the dataset does not contain any extra data splitting. At this rate, a separation to groups based on different halides. The separation per different halides is also driven by publication W. Travis et al. about the revised set of ionic radii for cations that is anion dependent. [106]

Figure 10 illustrates structural maps of A_2BX_6 compounds with the separation per halides. In this case, it is easier to find clear t boundaries of double perovskites stability regions for A_2BF_6 (dashed lines). It is interesting to note that the slope of

borders might be a result of interconnections between t and μ or display an insufficiency of μ factor. t factor is the geometrical parameter with a hard fixed optimal value. The value $t = 1$ corresponds to a right triangle in 'ideal' cubic perovskite, but μ doesn't have a fixed 'ideal' value and strict binding to the cubic structure. We can conclude that μ factor might not be hard related to the formation of cubic double perovskites.

Due to noted dataset unevenness, borders of other groups are complicated to note in this map configuration. However, we can notice that areas of known double perovskite regions are shifted on t axis relative to each other.

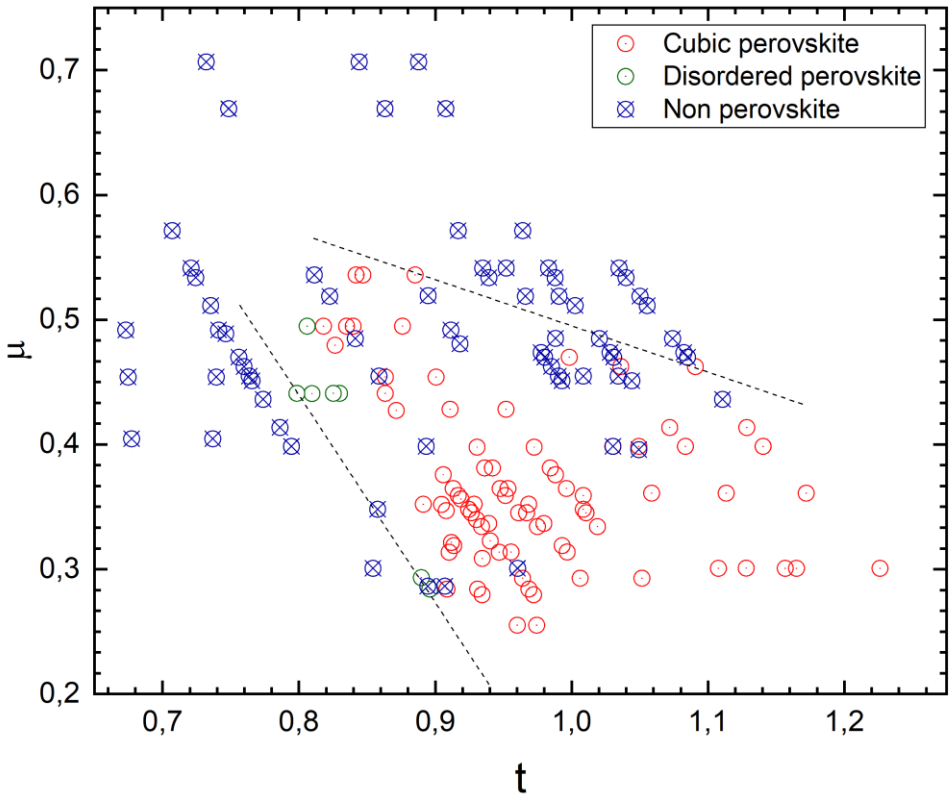

Figure 9. General structure map of A_2BX_6. Dash lines are approximately borders of double perovskites stability area.

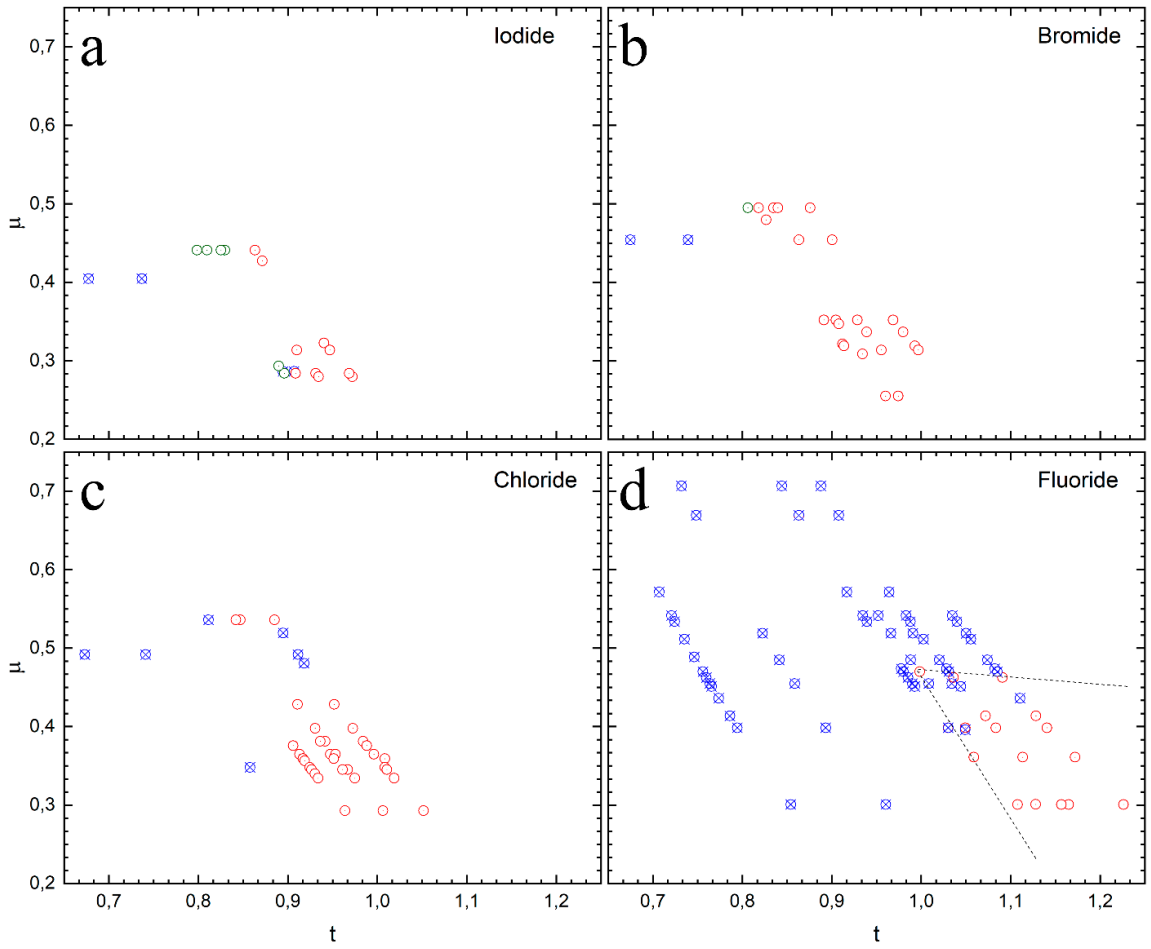

Figure 10. Structure maps separated by halide. a) Iodide, b) Bromide, c) Chloride, and d) Fluoride. Dashed lines limit approximately borders of double perovskites stability area.

In view of the noted shifted positions of stability regions and possible irrelevance of μ, it is necessary to analyze values of the shift on t axis. Figure 11 displays a chart of double perovskites separated by halides and ordered by its value of t factor. In the chart configuration, optimal range borders are clear for $I, Br,$ and Cl. In the case of F, the border is still fuzzy. However, the stability area of F based perovskites is compact and could be distinguished. Minimal border position of the optimal t factor has a trend to change from poorly distinguishable high-value ($t > 0{,}99$) in case of fluoride to clear low-value ($t \sim 0{,}79$) in case of iodide.

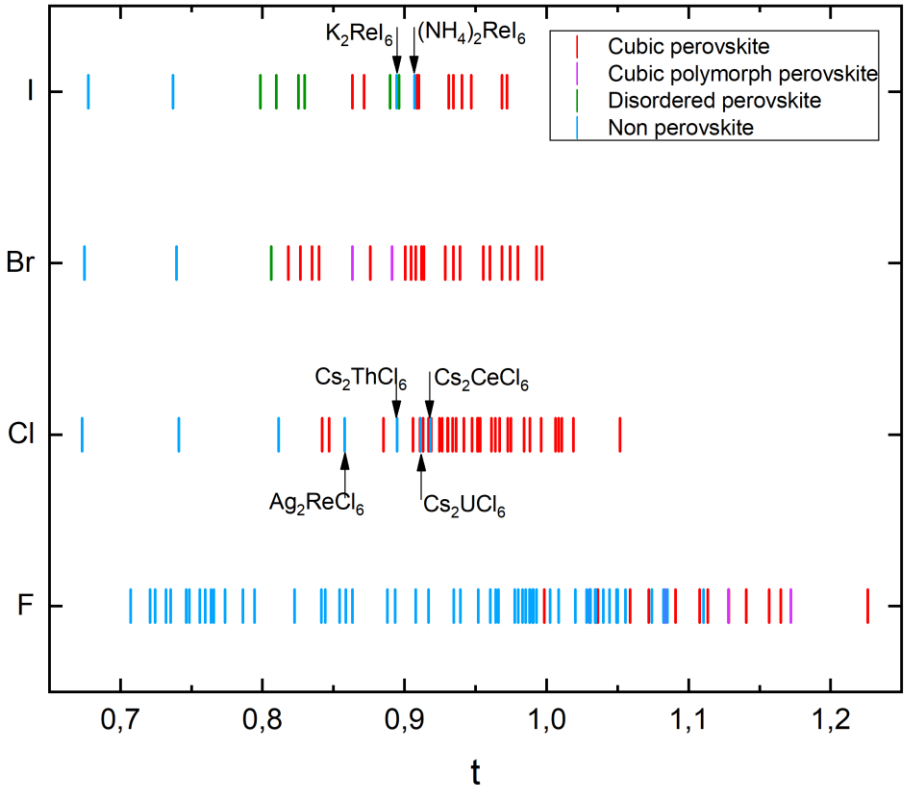

Figure 11. A_2BX_6 compounds separated by halides and ordered by its value of t factor. Values of the left border for stability regions: t~0,79 for I, t~0,8 for Br, t~0,84 for Cl, and $t > 0{,}99$ for F.

Existing of these stability regions demonstrate the applicability of t factor to vacancy-ordered double halide perovskites. Despite separation per halides, the general rule seems similar to ABX3 halide perovskites. The borders noted above are limited stability regions with accuracy over 92% for I, Br, Cl and 53% for F cases.

It is instructive to discuss the boundary cases and the exceptions as noted by arrow keys.

In the case of A_2BF_6, the fuzzy border follows an unusually big number of polymorphs (18 compounds) in standard ambient conditions. The polymorphism indicates a number of minimums of Gibbs free energy and relatively small

potential barriers between phases.[107] As a result, the area with a large number of stable and quasi-stable crystal phases forming the poorly distinguishable border. In other words, the perovskite phase might exist, but its formation energy might not be optimal in spite of the value of t factor. Therefrom possible to expect limited stability of A_2BF_6 compounds and it corresponds reported data.[104] The case of A_2BCl_6 demonstrates better distinguishable border, but it still has some indeterminacy. At least one compound located along a border is special. Ag_2ReCl_6 is the only reported A_2BX_6 compound with A cation from group 11 of the periodical table. We assume that it indicates unknown reasons obstructive formation of $A_2^{XI}BX_6$ compounds in a general way. It also means that this "unique" compound might follow the usual A_2BX_6 formation, and we can note it like a critical case. Another three exceptions: Cs_2ThCl_6, Cs_2CeCl_6 and Cs_2UCl_6 follow to the border indeterminacy pattern.

Groups of A_2BBr_6 & A_2BI_6 continue the border sharpening trend. The case of A_2BBr_6 has two compounds with perovskite/non-perovskite polymorphism and is in good agreement with borders sharpening. The case of A_2BI_6 does not have it. Concurrently, bromides start to display disorder perovskites on the stability border. Iodine-based compounds have a bigger number of these compounds (6 vs 1) in the light of similar numbers of compounds in the dataset.

We presume that disordered compounds display the second part of the general trend: from the poorly distinguishable border (intersection of sets of perovskites and non-perovskites) to clear border with disordered (K_2SnCl_6 type) perovskites on the border of optimal range. It might be relevant with a change of potential of perovskite phase on Gibbs free energy surface in the row of halides from F to I.

Unfortunately, we cannot define high-value borders of t factor optimal range due to limited data.

The workability of t factor is supported by data about new hybrid double perovskites. Crystal structure and values of t factor of recent reported[81] organic-inorganic double perovskites (where A is a small organic molecule) correspond to

our optimal suggested ranges based on the fully inorganic dataset. MA_2TeI_6 ($t = 0{,}9748,$), MA_2TeBr_6 ($t = 1{,}1445,$), FA_2TeI_6 ($t = 1{,}0551,$) and FA_2TeBr_6 ($t = 1{,}2475,$) ($r_{MA} = 217pm, r_{FA} = 253pm$)[91] having double perovskite structures and t factor values inside suggested stability areas. The match with suggested optimal ranges demonstrates the applicability of t factor for hybrid double perovskites.

The reason for the stability border shift is an open question. It is possible to presume that the reason might be connected with the formation of $[BX_6]^{-2}$ octahedral. Hypothetically, it might be an influence of X anion effective ionic radius and electronegativity at vacancy-ordered perovskite formability. Anion dependent change of effective ionic radii introduced by W. Travis et al. might be one of the possible interpretations;[106] Thus, the exact nature of observed shift of the optimal range needs future research include anion dependent refinement of effective ionic radii for B^{+4} cations.

As we noted in the problem statement, the values of stability borders are useful for the prediction of potential A_2BX_6 double perovskites. Suggested t factor optimal range and using only stable/quasi-stable elements it is possible to predict: 256 A_2BI_6, 252 A_2BBr_6, 200 A_2BCl_6 and 88 A_2BF_6 (total 796 compounds) undescribed full inorganic compounds satisfy the optimal range of double perovskite structure. The same way is useful to design and new hybrid organic-inorganic double perovskite.

Searching for possible correlation between physicochemical properties (e.g., electrical, optical, stability) of double perovskites and values of its t factor is a challenge for future research. Looking for ways that could help to form quasi-stable double perovskites with the value of t out of the optimal ranges could be an opportunity to increase this class of materials. It also might be related to unknown formability factors.

2.3 Conclusions

In this study, 170 A_2BX_6 compounds have been analyzed. We determine that Goldschmidt's tolerance factor is applicable for the prediction of formability A_2BX_6 vacancy-ordered double perovskites in analog with ABX_3 perovskites as necessary but not sufficient condition. We found that the minimum value of t factor optimal range and border blurring decreasing in the row of halides from F to Cl to Br to I. These optimal ranges suggest the potential existence of 796 A_2BX_6 full inorganic double halide perovskite compounds.

Chapter 3. Beyond Tolerance Factor: using deep learning for prediction formability of ABX_3 perovskite structures

Abstract

Deep learning is a modern, powerful instrument for multiple purposes, including classification. In this study, we applied this technique to the task of perovskites formability. We used a commonly known perovskite dataset to try to make an instrument superior to the 'classic' geometric approach. We found that the resulting models allow the finding of inaccuracies in the data and could successfully forecast perovskite formability with an accuracy of over 98% for the best case.

This chapter is based on the following published article:

Fedorovskiy, Alexander E., Valentin IE Queloz, and Mohammad Khaja Nazeeruddin. "Beyond Tolerance Factor: Using Deep Learning for Prediction Formability of ABX3 Perovskite Structures." Advanced Theory and Simulations 4.5 (2021): 2100021. DOI: 10.1002/adts.202100021

In this work, I collected data, created the dataset, and built all the models. Valentin Queloz consulted and supported the process of the study, Mohammad Khaja Nazeeruddin supervised the process.

3.1 Introduction

The family of materials with perovskite structure has a key role to play in many different areas such as piezoceramics[108], superconductivity[109], photovoltaic[66], and others[31,110]. The history and progress of each of these fields are based on searching for new perovskite compounds with better-optimized properties.

The experimental search for new compounds is an expensive and time-consuming process, reminiscent of trial and error. A desire to ease that process led to the creation of many different theoretical and empirical-based techniques. The main goal is to cut off variants of compounds with low success chances and direct research to the most promising ones.

One of these techniques is predicting the structure stability of the given chemical composition. It is a generally unresolved challenge in material science, especially for solid-state non-molecular compounds[111,112]. However, modern "heavy" computational methods can predict correct structures of new compounds[113,114]. Of course, they are not applicable for all compounds and are often limited only inside specific subclasses, and hard to scale up for screening due to their complexity and slow speed. At the same time, simple geometric and empirical prediction approaches for some structure classes are in use for around a century[87]. They are not limited by their complexity to use for screening but usually have lower accuracy.

The perovskite family has two widely used geometrical factors: Goldschmidt's tolerance factor $t = (r_A + r_X)/(\sqrt{2}[r_X + r_B])$ [87,115] and the octahedral factor $\mu = r_B/r_x$ [88] (where r_A, r_B and r_X are ionic radii for ions in A, B and X sites). Obtained from the geometry of the perovskite unit cell, they found application in the prediction of perovskites formation. Li et al. revealed an optimal range of t and μ factor for oxide and halide perovskites[88,89]. Later, Kieslich et al. widened the application of these factors to hybrid organic-inorganic perovskites[91].

The predictions using only the geometrical factors do not cover all cases in Li's dataset[88,89]. The resulting mistake is acceptable for such a simple and easy-to-use approach. However, the model has a problem when scaled up. Adding extra features to improve its performance leads to n-dimensional space (where n>3), and searching for new optimal regions in the n-dimensional is a complex task.

Analysis of n-dimensional spaces to resolve classification problems (in our case, perovskite/non-perovskite) is possible by using machine learning (ML) techniques. ML is a collection of different algorithms and approaches (e.g., Support vector machine (SVM), Random Forest, Artificial Neural Networks (ANNs), etc.)widely used in various research topics for data analysis and predictions[116–118].

There are already several reports using a form of supervised learning classification techniques for the prediction of perovskite formation[119,120]. However, in most of these publications, the authors did not involve new features in addition to ionic radii. Moreover, they used specially prepared and dependent features. For example, Pilania et al.[120] are using 11 input features, but 7 of them are depending only of r_A, r_B, r_X. This reflects they used the SVM method as a part of the linear classification algorithms family, which often requires an in-depth feature engineering process[121].

Classification algorithms based on ANNs are free from the limitations of linear ones. The deep learning (DL) method is based on using multi-layer ANNs. Over the last decade, ANNs & DL have become a hot topic in ML with a huge amount of applications[122–124]. Their properties such as excellent scaling up, less demand for feature engineering, and relatively easy prototyping, and an excellent candidate for application in the perovskite classification task.

In this paper, we have the objective to demonstrate the application of the DL to predict the formation of perovskite structures.

3.2 Dataset

It is easy to argue that the prediction task could be reformulated to a classification problem where we classify compounds for two classes: perovskite and non-perovskite. In DL, we can solve this type of problem by supervised learning. Supervised learning for classification requires a dataset. In our case, the dataset is a list of chemical compounds, where every compound has a label (1 for perovskites and 0 for non-perovskites) based on known experimental data. The noted above publications of Li et al. have exactly this type of data divided by two perovskite subclasses: oxide and halide perovskite subclasses[88,89]. The datasets represent oxide (ABO_3, given in Table A2.1) and halide (ABh_3, $h = F, Cl, Br, I$ given in Table A2.2) perovskites. Keeping the splitting between these subclasses helps us reducing the complexity of the problem (however, we do report the merged case below).

To keep the reliability of the data and to avoid or take into account possible anomalies in the datasets, we perform an initial analysis.

Figure 12 presents compounds per type. Their ratios ($40.8\%/59.2\%$ for dataset 1, $42\%/58\%$ for dataset 2) are not far from "ideal" 50%/50%. In the case of DL, it means that the NN will be equally trained for both types.

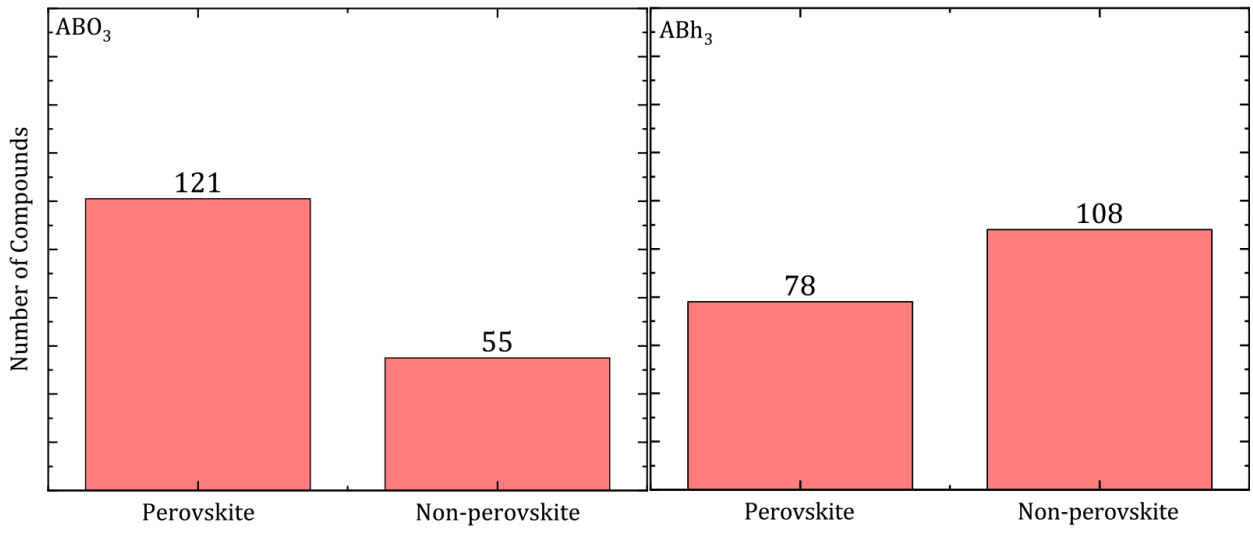

Figure 12. The number of compounds per label (perovskite/non-perovskite).

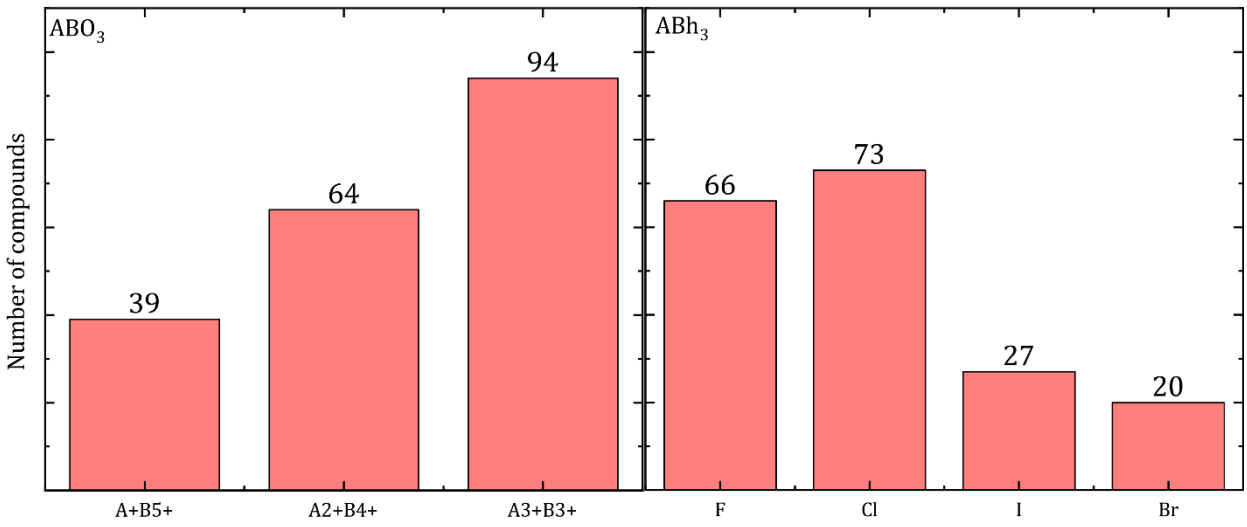

Figure 13. The number of compounds per subclass in the subsets.

Both datasets have internal subclasses. In the case of dataset 1, there are three subclasses with different charge balances ($A^{+}B^{+5}O_3$, $A^{+2}B^{+4}O_3$ and $A^{+3}B^{+3}O_3$). In the case of dataset 2, there are four subclasses with different halides (ABF_3, $ABCl_3$, $ABBr_3$ and ABI_3). Figure 13 presents compounds per internal subclass. As we can see, the subclasses in both datasets do not have an even distribution. This might be a result of many factors such as relatively small experimental coverage of whole compound space where perovskites may exist [54], synthesis difficulties increasing proportionally to the halide period number[104], etc. Figure 14 displays compounds per type for each internal subclass. In the case of DL, it means that datasets splitting to training and test subsets should be done carefully to avoid possible imbalance.

We understand that the dataset is relatively small, and it might influence to results NNs. However, we found examples in literature with around the same size of a dataset (~500 data points), and they display successful results for tasks with a complexity comparable to our target.[125,126] Therefore, we found it interesting to show that DL prediction of perovskite formation is possible by using a relatively small dataset.

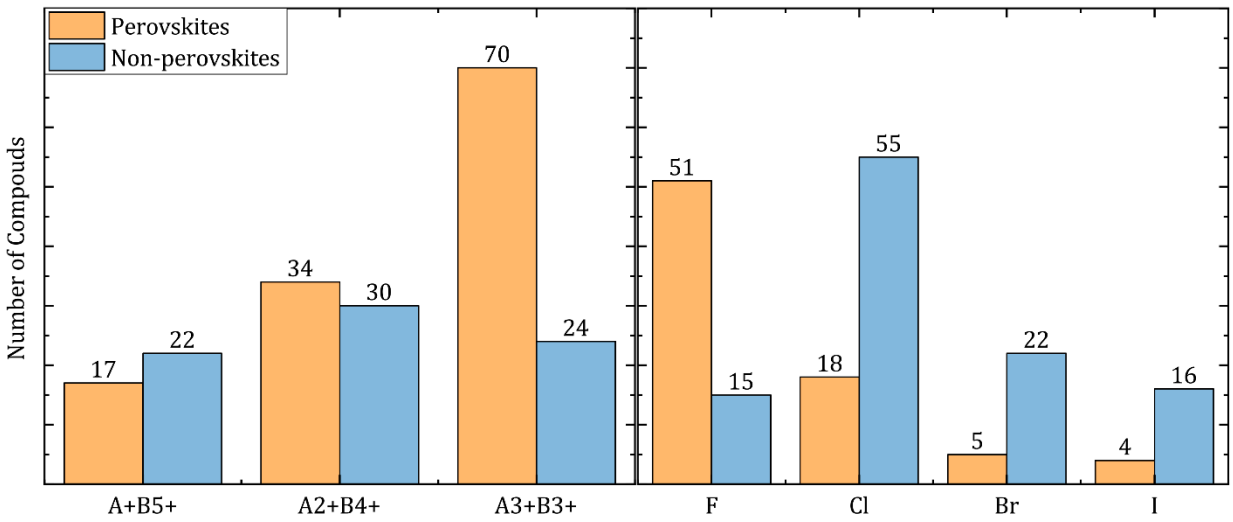

Figure 14. The number of compounds per label (perovskite/non-perovskite) in each subclass.

Using NNs presume to use uniform, ordered number-only normalized input matrix (vectors). Therefore, our first task is to choose a way to encode chemical compounds. We chose a technique based on charge balance, atomic, and coordination numbers (in an ideal cubic perovskite structure). Atom A (coordination XII, positive charge) is the first position in the input vector, atom B (coordination VI, positive charge) is second, and atom X (coordination VI, negative charge) is third. It allows to encode and decodes every possible ABX_3 compound. For example, $[55, 82, 35]$ vector ($[0.55, 0.82, 0.35]$ after normalization) corresponds to $CsPbBr_3$.

3.3 Modelling and Results

We used Keras library (v2.4.0) with Tensorflow backend (v2.3.0) to make all the below described models. Table 1 has parameters that are common for all constructed networks. We chose an NNs 'pyramid'-like architecture where N_0 are several neurons for the first layer. Every next i layer (exclude output) has $N_i = int(N_0 * \left(1 - \frac{0.9}{L-1} i\right))$, L is several changeable layers. If calculated $N_i < 2$ we replace it to $N_i = 2$. The layers have a dropout with a 0.5 rate. We decided to keep the dropout rate as a constant because the results noted below do not display signs of under-learning. The output layer always has a single neuron. Therefore, N_0 and

L are hyper-parameters. To optimize hyper-parameters, we used the Bayesian optimization algorithm implemented in Keras Tuner, used validation accuracy as an aim parameter. We chose borders of the hyperparameters as $N_0 \in [10, 1000], \Delta N_0 = 10$ and $L \in [1, 10], \Delta L = 1$. We choose the best models as ones with the highest total accuracy (training & test). In the case of equivalent accuracies, we discuss a model with the smallest number of parameters. The source code and input files are available on GitHub[127].The single output neuron has a sigmoid activation function. The output corresponds to labels noted above (0 is non-perovskite, 1 is perovskite). The dataset was randomly shuffled and spitted into training and test sets in 70%/30% ratio.

Loss function	Binary cross-entropy
Activation function (exclude the last layer)	ReLU
Activation function (last layer)	Sigmoid
Kernel initializer	Uniform
Optimizer	Adam ($\alpha = 0.001, \beta_1 = 0.9, \beta_2 = 0.999, \epsilon = 1 * 10^{-7}$)
Batch size	64

Table 1. Common parameters of the constructed NNs.

We found it interesting to try to make models without extra data features to use it as an indicator of predicting complexity and be a good start point. The best of these simple models with input features $x_f = |n_A \quad n_B \quad n_X|$ reached accuracies: for ABh_3 up to 87.5% on the test set (82.31% on the training set; $N_0 = 660$, $L = 3$), for ABO_3 up to 86.44% on the test set (83.94% on the training set; $N_0 = 560$, $L = 2$). Interesting to note that model for ABO_3 does not have information about the subclasses; however, it reached almost the same accuracy. In the case of the merged dataset $ABh_3 + ABO_3$ the model reached accuracy up to 86.96% on the test set (82.77% on the training set; $N_0 = 720$, $L = 3$).

We assume that lower accuracy in the merged case corresponds to the increased complexity of the task. We consider that a summary of the results corresponds to a situation with many 'easy to predict' or 'core' cases; however, it cannot show high accuracy for border cases. Figure 15 presents an error map of the models in $\mu: t$ space.

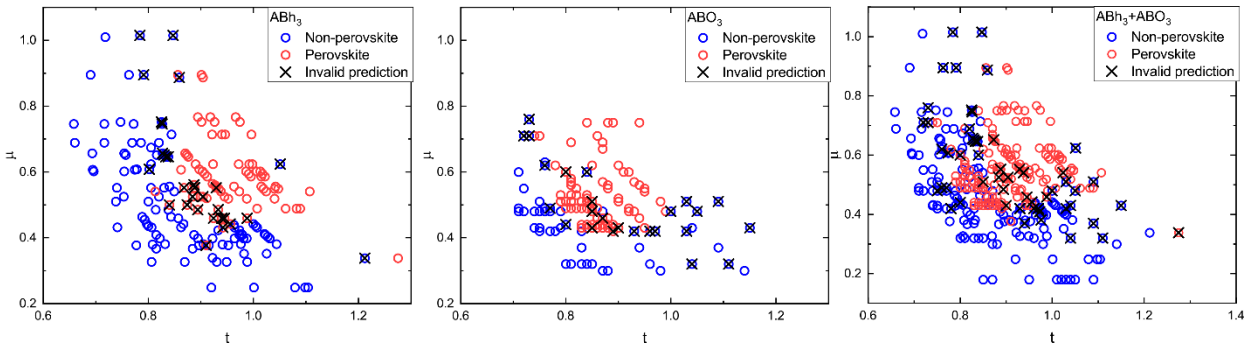

Figure 15. Error maps for models with $f = |n_A\ n_B\ n_X|$.

Accordingly, we expected that accuracy improvement is possible by adding extra data features. It might allow for a description of specific interactions and patterns of formability for these 'border' cases.

For the first, we chose ionic radii r_i for each element. Values of r_i were taken the same as in the origin of the dataset [88,89,98]. We have to note that using different radii values [106,128] may lead to different results. The best of these models with input features $x_f = \begin{vmatrix} n_A & n_B & n_X \\ r_{i\_A} & r_{i\_B} & r_{i\_X} \end{vmatrix}$ reached accuracies: for ABh_3 up to 91.07% on the test set (86.92% on the training set; $N_0 = 680$, $L = 6$), for ABO_3 up to 98.31% on the test set (97.81% on the training set; $N_0 = 730$, $L = 4$) and for the merged $ABh_3 + ABO_3$ case, the model reached accuracy up to 95.65% on the test set (95.51% on the training set; $N_0 = 680$, $L = 5$). The growth of the model's accuracies correlates with our hypothesis noted above. At this stage, the model for the ABO_3 case has higher accuracy than the geometrical approach (4 errors of our model vs 5 in case of $t - \mu$ approach)[88].

As a next feature, we add electronegativity values according to the Pauling Scale [129]. The best of these models with input features $x_f = \begin{vmatrix} n_A & n_B & n_X \\ r_{i\_A} & r_{i\_B} & r_{i\_X} \\ \chi_{p\_A} & \chi_{p\_B} & \chi_{p\_X} \end{vmatrix}$ reached accuracies: for ABh_3 up to 92.86% on the test set (96.15% on the training set; $N_0 = 930$, $L = 5$), for ABO_3 up to 96.61% on the test set (97.08% on the training set; $N_0 = 820$, $L = 2$). In the merged $ABh_3 + ABO_3$ case, the model reached accuracy up to 93.91% on the test set (96.63% on the training set; $N_0 =$

280, $L = 7$). Based on the result, we presume that electronegativity has a higher correlation to the formation of ABh_3 than ABO_3.

For the next step, instead of electronegativity, we added a covalent radius r_c for each element[130]. The best of these models with input features $x_f = \begin{vmatrix} n_A & n_B & n_X \\ r_{i\_A} & r_{i\_B} & r_{i\_X} \\ r_{c\_A} & r_{c\_B} & r_{c\_X} \end{vmatrix}$ reached accuracies: for ABh_3 up to 92.86% on the test set (93.85% on the training set; $N_0 = 1000$, $L = 6$), for ABO_3 up to 98.31% on the test set (97.81% on the training set; $N_0 = 890$, $L = 3$). Another model for ABO_3 achieved 100% accuracy on the test set (97.81% on the training set; $N_0 = 940$, $L = 6$). Due to the relatively small dataset size, we note with caution this result, and we expect that this model might be overfitted and have lower generalization ability in the future. In the merged $ABh_3 + ABO_3$ case, the model reached accuracy up to 95.65% on the test set (96.25% on the training set; N_0 =580, $L = 4$). Accordingly, using r_c help to improve model accuracies for all cases. We found that using this variant of input allows reaching high accuracy (and possible overfitting) for relatively small networks, e.g., a model for ABO_3 has accuracy up to 100% on the test set (94.89% on the training set) with $N_0 = 330$, L =3.

To evaluate the effect of using a bigger feature number, we tried two more input configurations. For both, we increased the number of learning epochs from 500 to 1000 and decrease the number of optimization iterations to 250 to keep calculation time. First, we tried to combine all previously used features. The best of these models with input features $x_f = \begin{vmatrix} n_A & n_B & n_X \\ r_{i\_A} & r_{i\_B} & r_{i\_X} \\ \chi_{p\_A} & \chi_{p\_B} & \chi_{p\_X} \\ r_{c\_A} & r_{c\_B} & r_{c\_X} \end{vmatrix}$ reached accuracy for ABh_3 up to 92.86% on the test set (95.38% on the training set; $N_0 = 260$, $L = 6$), for ABO_3 and up to 98.31% on the test set (99.27% on the training set; $N_0 = 820$, $L = 2$) and for the merged $ABh_3 + ABO_3$ case up to 99.25% on the test set (94.78% on the training set; $N_0 = 920$, $L = 3$).

Second, we added information about the charge of each element as an implementation of subgroups information. The best of these models with input features $x_f = \begin{vmatrix} n_A & n_B & n_X \\ q_A & q_B & q_X \\ r_{i\_A} & r_{i\_B} & r_{i\_X} \\ \chi_{p\_A} & \chi_{p\_B} & \chi_{p\_X} \\ r_{c\_A} & r_{c\_B} & r_{c\_X} \end{vmatrix}$ reached accuracy for ABh_3 up to 92.86% on the test set (94.62% on the training set; $N_0 = 640$, $L = 5$), for ABO_3 up to 98.31% on the test set (97.08% on the training set; $N_0 = 410$, $L = 3$). Another model for ABO_3 achieved 100% accuracy on the test set (100% on the training set; $N_0 = 410$, $L = 3$); however, we assume that it might be a result of false-correlation on a relatively small dataset. For the merged $ABh_3 + ABO_3$ case up to 95.65% on the test set (96.25% on the training set; $N_0 = 760$, $L = 7$).

Table 2 represents a summary of the models described above.

To get a better understanding of our model's limitations and try to improve the results, we have reviewed their mistakes. Tables A2.3-A2.5 contain a listing of errors for all discussed models. We analyzed mistakes of all models except the simplest only n based. Figure 16 presents an error map of selected models in μ: t space.

Features\Cases	Accuracy %	ABh_3	ABO_3	$ABh_3 + ABO_3$
n	Training	82.31	83.94	82.77
	Test	87.5	86.44	86.96
n, r_i	Training	86.92	97.81	95.51
	Test	91.07	98.31	95.65
n, r_i, χ_p	Training	96.15	97.08	96.63
	Test	92.86	96.61	93.91
n, r_i, r_c	Training	93.85	97.81 | 97.81	96.25
	Test	92.86	98.31 | 100	95.65
n, r_i, χ_p, r_c	Training	95.38	99.27	99.25
	Test	92.86	98.31	94.78
n, q, r_i, χ_p, r_c	Training	92.86	97.08 | 100	96.25
	Test	94.62	98.31 | 100	95.65

Table 2. Summary of the models with different inputs.

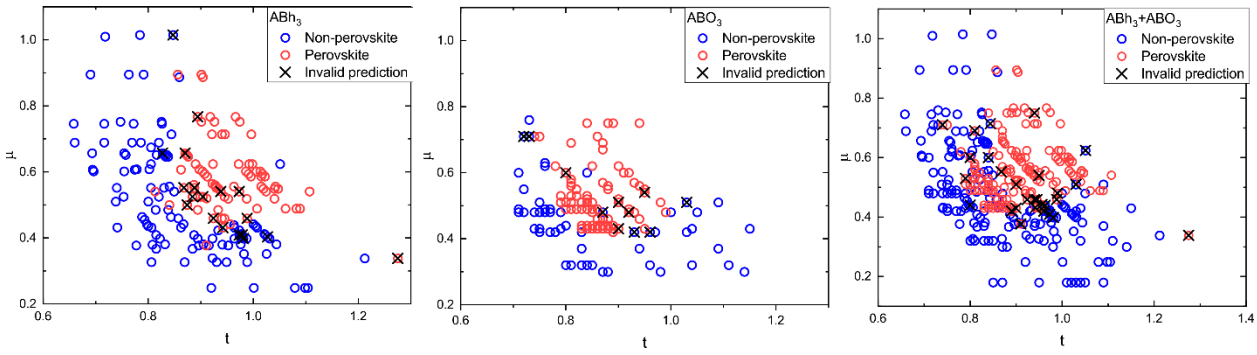

Figure 16. Error maps for a summary of models with the increased feature vector.

To find a possible reason for the mistakes, we performed literature research and found that not all these mistakes are valid. By analyzing ICSD, we found that ~15% of all reported ABX3 halide perovskites display polymorphism at normal conditions. Our assumption is that polymorph (perovskite + any other phases) is seen as perovskite because it can reach the objective phase. Regarding this fact, we rechecked the validity of labels for all 50 mistakes (SI6). As a result, we found

reports of perovskite structure for 11 of them that correspond to the model's predictions. For the other 5 cases, we found reports about thermodynamically instability or existence only in the predicted non-perovskite phase (see comments in Table A2.6). For the next 34 cases, we found reports that confirm the mistake of the prediction. Finally, for the last 2 cases, we have not found any structural reports, so they cannot be judged.

This mistaken analysis confirms our caution about overfitting the highly accurate models with many input features noted above. However, using a reasonable size of the input vector (e.g., cases n ri or $n\ ri\ rc$) and/or a relatively small number of training epochs allows us to get good generalization ability and right prediction despite few initially wrong labels.

3.4 Conclusion

In this study, we build several deep-learning models trained on a dataset of 483 compounds with general formula ABX_3. We demonstrated a change of forecast accuracy independence of input feature vector and optimized size-related parameters of NNs for the task. Our models were able to help found mistakes in the used dataset and reached an accuracy of over 98% for ABO_3 and over 94% for ABh_3.

The main ability of the studied models is a possibility of further improving as soon as new experimental data become available. We hope that these results will be useful not only as a perovskite formability prediction instrument but also as a background of further NNs design for prediction crystal structures.

Also, we can note that interpretation of the NNs and their expansion to other classes of perovskite super-family (e.g., double perovskites) remain an open question.

Chapter 4. A_2TeX_6 halide vacancy ordered perovskites: The problem of unequivocal optical band gap definition

Abstract

Family of A_2TeX_6 halide vacancy ordered perovskites is a potential candidate for optoelectronics as a lead-free version of halide perovskites. In this study, we performed synthesis and research of physiochemical properties of the group. We found unusual issues with the determination of band gaps during the study based on optical spectroscopy data. Further investigation showed the limitation of Tauc's plot applicability for this family of materials.

This chapter is based on the following research (preprint state):

Alexander E. Fedorovskiy, Olga A. Syzgantseva, Valentin I. E. Queloz, Iwan Zimmermann, Sara Bonomi, Lorenzo Malavasi, Nikita A. Drigo, Hobeom Kim, Giulia Grancini, and Mohammad K. Nazeeruddin. "A_2TeX_6 halide vacancy ordered perovskites: The problem of unequivocal optical band gap definition."

In this work, I was leading the research, made the problem statement, compounds synthesis, single crystal growth, powder XRD experiment, UV-Vis optical spectroscopy experiment, data analysis. Also, I contributed PL, TGA, and thin-film growing experiments. Olga Syzgantseva performed calculations, Valentin Queloz made a PL experiment, Iwan Zimmermann made single-crystal XRD experiments, Sara Bonomi and Lorenzo Malavasi made magnetron sputtering experiment, Nikita Drigo made TGA experiment, Hobeom Kim made UPS experiment, Giulia Grancini consulted and expertized PL and UV-Vis experiments, Mohammad Khaja Nazeeruddin supervised the process.

4.1. Introduction

Perovskite solar cells (PSC) demonstrate significant progress, with the efficiency grown from 4% in 2009 up to 25.6% nowadays.[131,132] These remarkable results are based on a set of specific properties. These include huge variability of compounds inside halide perovskite class, from full inorganic to hybrid metal-organic crystals that allow tuning properties such as band-gap width and extending the application to other optoelectronic devices such as light-emitting diodes.[133,134] Also, the perovskites display an unusually high level of defect tolerance and have the capacity of easier (relative to silicon-based solar cells) manufacturing processes, e.g., solution-based or thermal evaporation deposition.[33,132]

Unfortunately, the high-efficient PSCs are lead-based with general formula $APbX_3$. Lead is a known toxic metal with cancerogenic properties.[43,44] The situation is exacerbated by the water-solubility of the halide perovskite compounds and their precursors (mostly PbI_2 and $PbBr_2$) with higher toxicity.[44] The only solution to the toxicity problem is searching for new lead-free, environmentally friendly materials that would be able to keep most of PSCs advantages at the same time.

Different research groups suggest various candidate compounds. Some of these compounds follow the structure of original $APbX_3$ compounds (e.g., $ASnX_3$), the others deviate from the source to a new structure with different levels of similarity to perovskite structure, such as double perovskites and 2D perovskites (e.g., $Cs_2AgBiBr_6$, PEA_2PbI_4, $PEA = phenylethylammonium$).[135,136] Despite a wide range of tested candidates, unfortunately, they demonstrate relatively low efficiency, and in some situations stability related issues, that is the case, for example, of Sn-based perovskites.[137]

New for the topic, a family of perovskite-like vacancy ordered structures with the general formula A_2BX_6 shows encouraging results. For example, one of the

first in the class-tested for PV, the Cs_2TiBr_6 based device, despite its low efficiency, shows remarkable stability over 350 hours without encapsulation.[76]

Within new tested candidates, Tellurium-based vacancy-ordered perovskites have demonstrated values of band-gaps 1.47-2.02eV near the close to optimal range in the Schottky-Queisser limit.[22,24,81] In conjunction with the optimistic report about long carrier diffusion length, it makes the A_2TeX_6 sub-family to be a new highlighted candidate for lead-free PSCs.

The nature of the optical gap, i.e., the direct or indirect character of the lowest transition, defines many optoelectronic parameters of the vacancy-ordered perovskites, including the photoluminescence intensity and the radiative limit of the charge carrier lifetimes. The first one is relevant for optoelectronic applications, while the second quantity is essential for photovoltaics. This is why it is crucial to understand the nature of the lowest optical transitions in these compounds in real experimental conditions. During the research, properties of the A_2TeX_6 perovskites, we found inconsistency of optical spectroscopy data interpretation for the determined nature of a band-gap. During our further investigation, we also found inconsistent PL results and challenges in the theoretical description. As a result, we would like to focus our manuscript on the problem of unequivocal optical band gap definition for A_2TeX_6 halide vacancy ordered perovskites.

4.2. Results and discussion

4.2.1 Synthesis

We performed the synthesis of $A'_2TeX'_6$ ($A' = K, Rb, Cs, NH_4, MA, FA$; $X' = Cl, Br, I$) compounds with both organic and inorganic cations. We have tried synthesis of $A'_2TeX'_6$ from two different sets of precursors.

1. TeX'_4 based

$$TeX'_4 + 2AX' \xrightarrow{HX', t^\circ} A_2TeX'_6 \ (1)$$

2. TeO_2 based[138]

$$TeO_2 + 6HX' \xrightarrow{t^\circ} H_2TeX'_6 + 2H_2O \ (2)$$

$$H_2TeX'_6 + AX' \xrightarrow{t^\circ} A_2TeX'_6 + 2HX \ (3)$$

In the second case, we use significant excess of halogenating acid. In both cases, the acid afterward evaporated.

For MA_2TeI_6 and FA_2TeI_6, we have performed single-crystal growing by using a drop-casting technique. In a nitrogen atmosphere, a small amount ($50\mu l$) of a compound dissolved in dry DMF ($25mg: 100\mu l$) was dropped on a glass substrate (Microscope slide) and then dried at $100°C$ until complete visual evaporation of the solvent.

4.2.2 XRD characterization

We studied the resulting product in powder state by powder XRD (Figure 17, Figures A3.1-A3.3), and to ensure accuracy and complete structural determination, grown small single crystals by single-crystal XRD (Figure 18, Table A3.1).

Regarding XRD patterns, the first synthesis method showed better results for the case of iodides (less number and intensity of extra XRD peaks up to its total absence) but did not work satisfactorily for bromides and chlorides. The second synthesis was a mirror; it shows good results only for bromides and chlorides but not for iodides. Hypothetically, it might be the result of different equilibriums in the process of formation $[BX_6]^{-2}$ for different halides. The equilibrium might be sensitive to acids concentration; at least, this point of view is supported by the literature.[139] We assume it is possible to adjust both ways for all halides via optimization of the reaction temperature and prolongation synthesis process. We found that using non-extra dry solvents for single crystal growth leads to an immediate degradation process that is expressed in extra peaks on an XRD pattern and precipitation of a white powder. We did not identify the decomposition

products successfully, but we anticipate a link with the hydration/oxidation process.

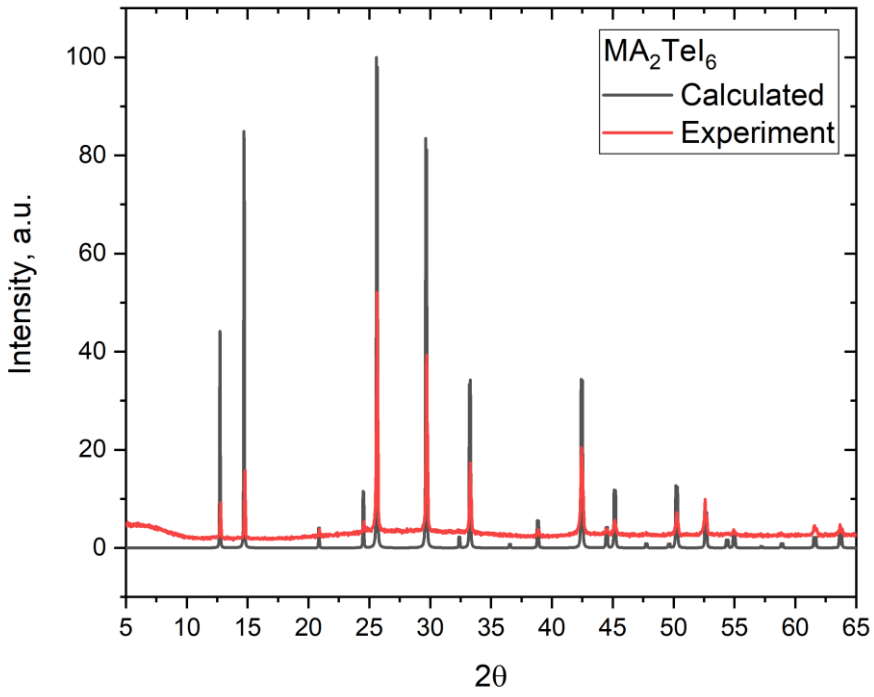

Figure 17. MA_2TeI_6 XRD pattern after synthesis and the pattern calculated from the single crystal data.

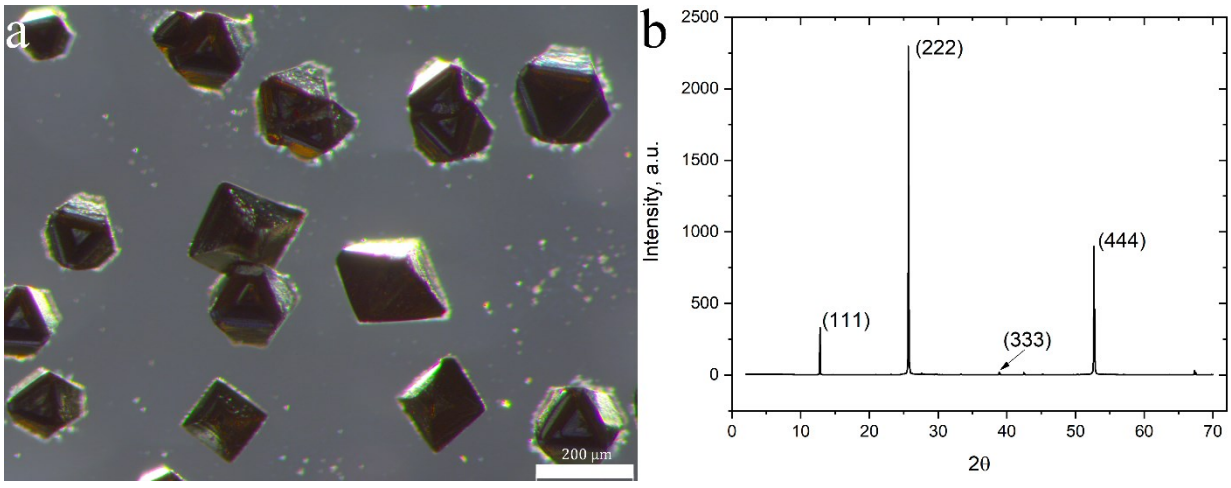

Figure 18. a) MA_2TeI_6 recrystallized from DMF-based solution via drop-casting on a glass substrate. b) XRD pattern shows that the crystals have orientation [111] along the vertical axis.

Table 3 displays the summary of the structural study. The results are good at correlating to previous publications.[81,140–143]

	I	Br	Cl
K	$P\ 2_1/n$ $t = 0.799$	$F\ m\bar{3}m$ $t = 0.806$	$I\ 2/m$ $t = 0.811$
Rb	$P\ 4/mnc$ $t = 0.830$	$F\ m\bar{3}m$ $t = 0.840$	$F\ m\bar{3}m$ $t = 0.847$
Cs	$F\ m\bar{3}m$ $t = 0.863$	$F\ m\bar{3}m$ $t = 0.876$	$F\ m\bar{3}m$ $t = 0.885$
NH_4	$P\ 2_1/n$ $t = 0.810$	$F\ m\bar{3}m$ $t = 0.818$	$F\ m\bar{3}m$ $t = 0.824$
MA	$F\ m\bar{3}m$ $t = 0.975$	$F\ m\bar{3}m$ $t = 0.997$	? $t = 1.012$
FA	$F\ m\bar{3}m$ $t = 1.055$	$F\ m\bar{3}m$ $t = 1.084$	? $t = 1.104$

Table 3. Structure summary of A_2TeX_6 compounds.

4.2.3 Optical (UV-Vis) spectroscopy

We used optical spectroscopy to determine band-gap type and width. During the experiment, we have measured reflectance (R) and transmission (T) coefficients of the materials. To get an absorption, we used the following equation

$$a_{simp} = \frac{1}{d} ln\ (\frac{1-R^2}{T})\ (4)$$

where d is the sample thickness. Due to the exact unknown value of the powder sample thickness, we ignored this coefficient and normalized the data. We determined the bandgaps as direct with width in the range (1.42eV-1.55eV for Iodides and 2.09eV-2.19eV for Bromides). Figure 19 displays the spectra.

During comparing our results with previously published data, we found inconsistency of band-gap type. Ju et al. also used optical spectroscopy to

determine the band-gap of the same materials; however, they determined the band gaps as indirect.[81] In both cases, the determination was based on Tauc plots, but different ways of absorption calculations were used. Due to the wide usage of the technique and noted above the importance of the band-gap determination, we found it interesting to continue an investigation about the reasons for the inconsistency.

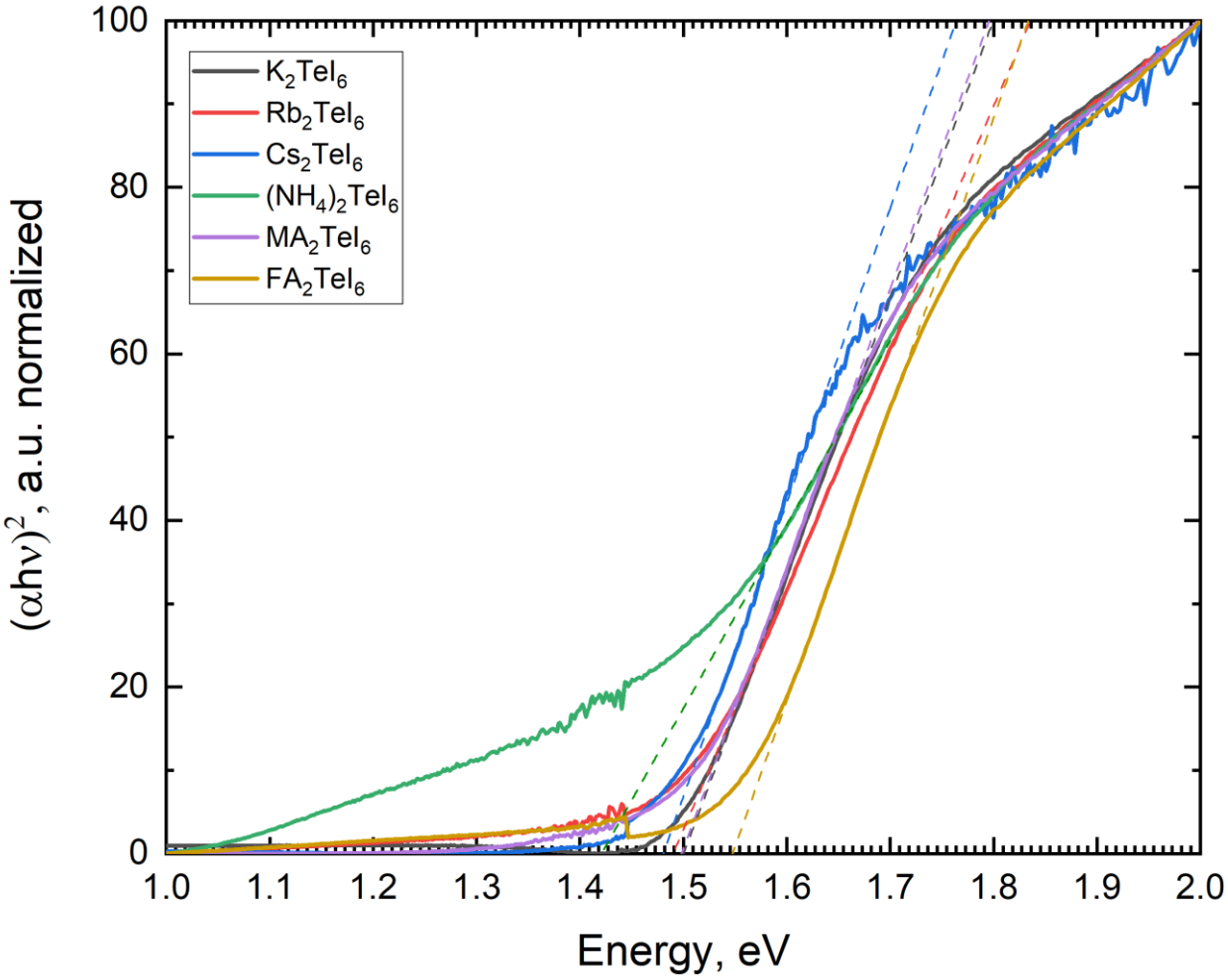

Figure 19. Tauc plots for A_2TeI_6 based on α_{simp} equation.

After comparing the experiment conditions, we found that the main difference is about the used absorption coefficient model. We attempted to use the same way based on the Schuster-Kubelka-Munk (SKM) equation (5)

$$F(R_\infty) = \frac{(1-R_\infty)^2}{2R_\infty} \approx \alpha_{SKM} \quad (5)$$

where R_∞ is the diffuse reflectance ($R_\infty \cong R$) and we successfully reproduced the "indirect" band-gaps (Figure 20) analog to Ju et al. This critical divergence of the results indicates the inapplicability of the used techniques.

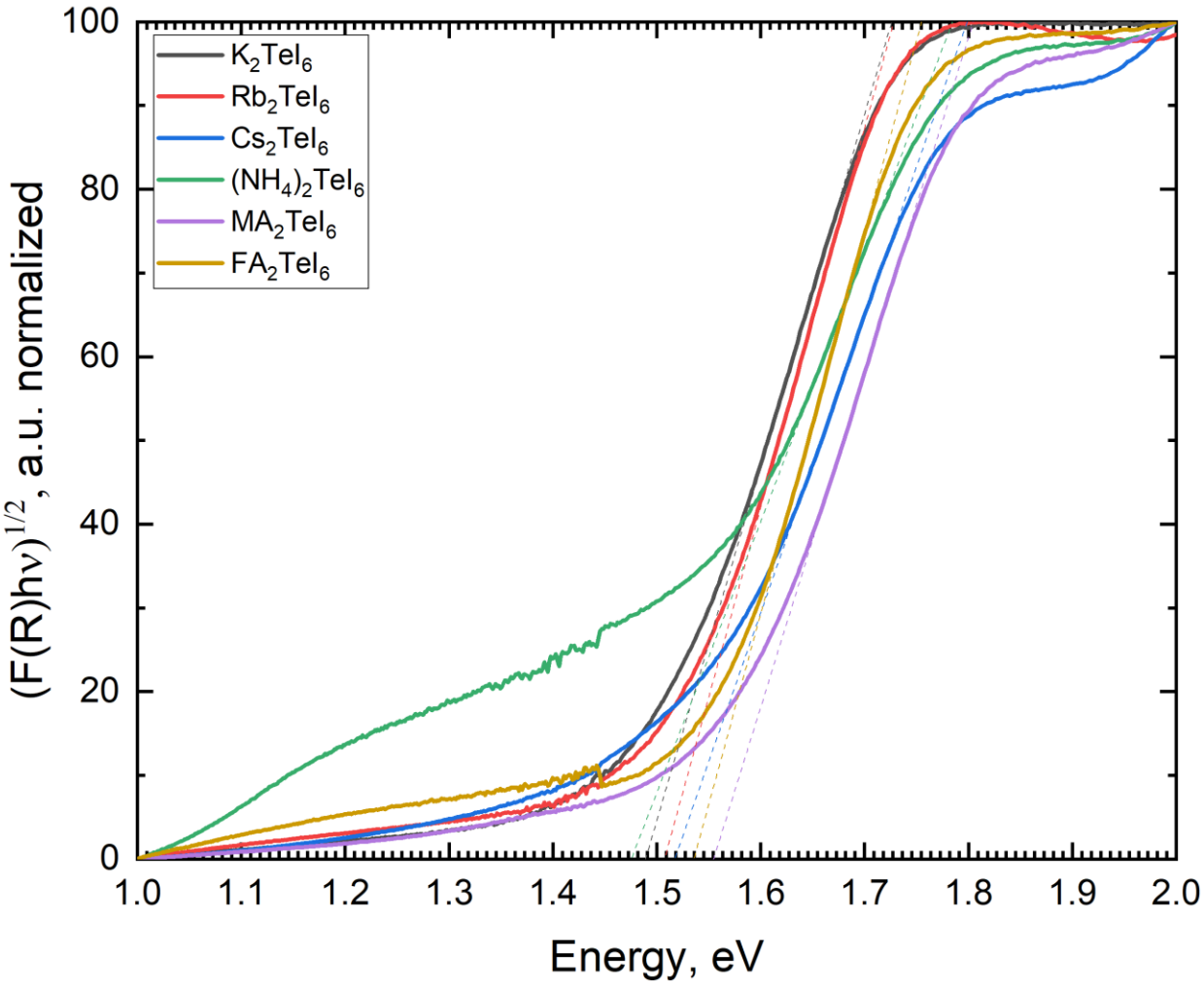

Figure 20. Tauc plots for A_2TeI_6 based on the SKM equation.

4.2.4 Analytical model for α coefficient

Noted above SKM equation is only a "good enough" approximation of an absorbance spectrum and based only on the R coefficient.[144,145] An alternative simplified model $\alpha_{BLB} = \frac{1}{d} ln\,(\frac{1}{T})$ is also limited and based only on T coefficient.[145] In this way, the process of choosing the suitable model and interpretation of the results compare are not clear.

A recent publication of A.R. Zanatta shed light on the problem.[145] On the example of well-known semiconductors, the author has shown discrepancies in results for the same data depending on the calculation technique. Figure 21 displays an example of different absorption spectra and "band-gaps" taken by a set of absorption models for MA_2TeI_6. The result type of the band-gap and its exact value directly depends on the chosen model for alpha calculation. Based on Zanatta's research, the most correct way to get a band-gap value is to use the Boltzmann function for fitting optical absorption spectra. The proposed technique has more precision and allows us to compare the direct and indirect variants.

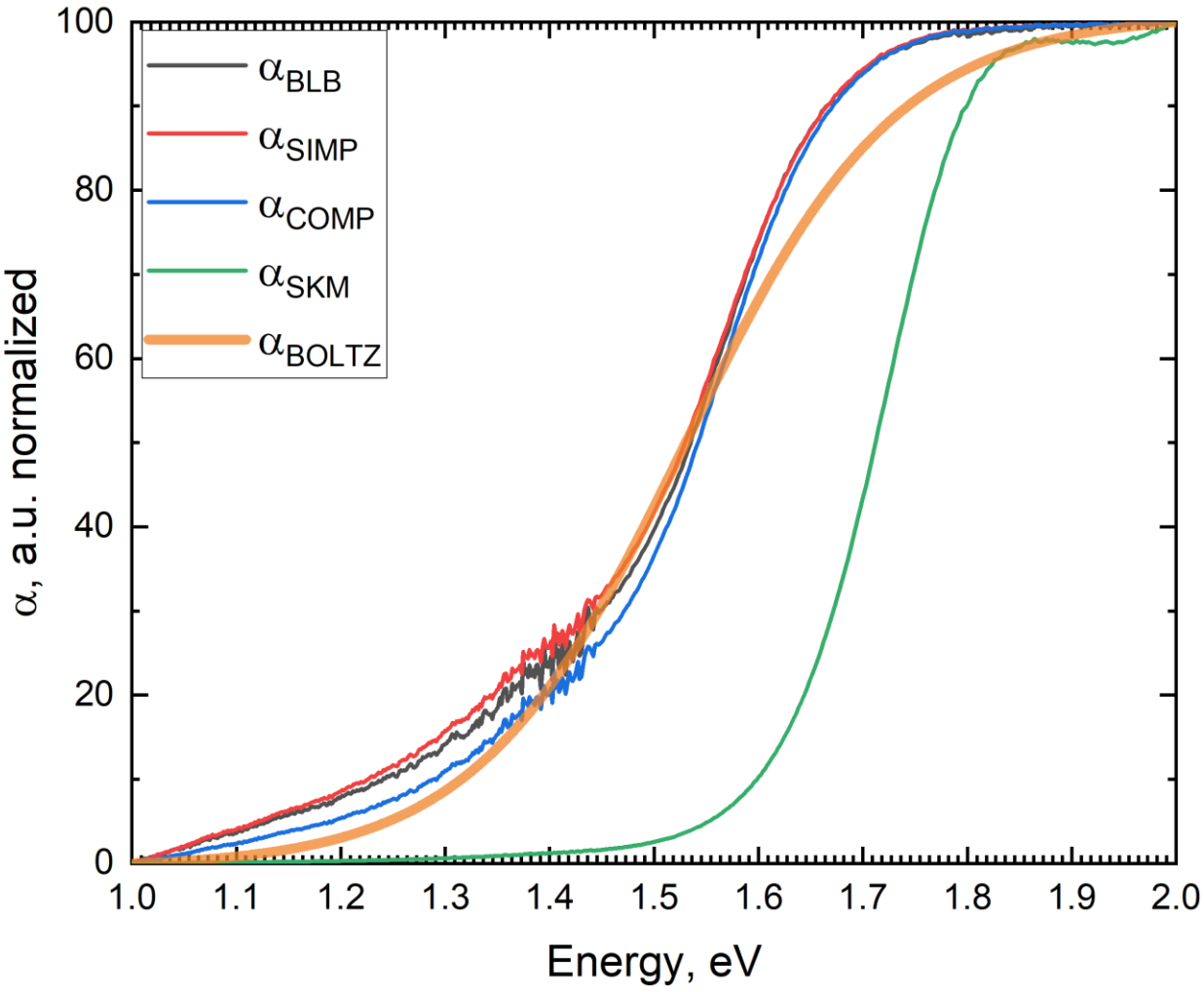

Figure 21. $\alpha(E)$ for MA_2TeI_6 calculated in different ways. a_{Boltz} is based on α_{comp}, coefficients $E_0 = 1.54eV$, $\delta E = 0.1$

Boltzmann fitting is made for equation (4):

$$\alpha_{Boltz}(E) = \alpha_{max} + \frac{\alpha_{min} - \alpha_{max}}{1+\exp\left(\frac{E-E_0^{Boltz}}{\delta E}\right)} \quad (6)$$

$\alpha_{max;min}$ are maximum and minimum values of the fitted absorption spectrum, $E_0^{Boltz} \approx E(\alpha_{mid})$, $\alpha_{mid} = \frac{\alpha_{max} - \alpha_{min}}{2} + \alpha_{min}$, δE is a coefficient associated with the sigmoid curve.[145] A band-gap value can be calculated from the fitted spectrums as:

$$E_g^{Boltz} = E_0^{Boltz} - n_{type}^{Boltz} \times \delta E \quad (7)^{145}$$

In equation (5) n_{type}^{Boltz} is adjusted constantly: $n_{dir}^{Boltz} = 0.3$, $n_{ind}^{Boltz} = 4.3$.[145]

For $\alpha(E)$ we used a model considered multiple internal reflections:

$$\alpha_{comp}(E) = \frac{1}{d}\ln\left[\frac{(1-R)^2}{2T} + \sqrt{\frac{(1-R)^4}{4T^2} + R^2}\right] \quad (8)^{145,146}$$

Figure 22 displays the application of the technique to A_2TeI_6 perovskites. Table 4 contains a summary of the absorption fitting for the A_2TeI_6 subfamily; Tables A3.2-A3.3 show a summary for the rest of the compounds. The optical band-gap values from Boltzmann fitting with the taken parameter $n^{Boltz} =$ 0.3 correspondings to direct type are better fitted to other models in terms of gaps width. In sum, with "direct" result using both experimentally measured coefficients (R & T) and advanced α_{comp} model, we are leaning towards definition the band-gap type as direct. However, we have to note that final defining the real types has not yet been achieved. As noted below, a possible small difference between direct and indirect transitions is the increasing complexity of the situation.

eV	K_2TeI_6	Rb_2TeI_6	Cs_2TeI_6	$(NH_4)_2TeI_6$	MA_2TeI_6	FA_2TeI_6
$(\alpha_{simp}E)^2$	1.5	1.49	1.48	1.42	1.55	1.55
$(\alpha_{comp}E)^2$	1.5	1.49	1.49	1.43	1.49	1.55
$(\alpha_{SKM}E)^{1/2}$	1.49	1.51	1.52	1.48	1.55	1.54
E_{Boltz}^{dir}	1.51	1.54	1.49	1.45	1.51	1.58
E_{Boltz}^{indir}	1.11	1.14	1.09	1.05	1.11	1.18

Table 4. Summary of the band-gap calculations for A_2TeI_6 compounds.

The discussion of the nature of the band gap in real materials based on the halide vacancy-ordered perovskites A_2TeX_6 demands in a first place the definition of notions to be determined. The fundamental gap is defined as the difference between the energies of the lowest edge of the conduction band and the highest edge of the valence, or alternatively, as the difference between ionization potential and electron affinity of the corresponding solid:

$$E_{gap} = E_C - E_V = I - A \quad (9)$$

The fundamental gap can have direct or indirect nature, depending on the difference in the symmetry of the wavevector k in the reciprocal space, corresponding to the top of the valence band and the bottom of the conduction band. The fundamental band gap is distinct from the optical gap, which is defined as the energy of the lowest optical excitation in the system, or an energy of the lowest exciton, formed by an interacting electron and a hole, while the fundamental gap is expressed in terms of energies of ionized and neutral systems excluding electron-hole interaction. The optical gap is often determined from the optical UV/vis absorption spectroscopy, as this is the case in the present work. In solids, the fundamental gap is thus reduced by the amount called exciton binding energy. Often, the values of the fundamental band gap and the optical gap are close; that is the case when the exciton binding energy is small. However, in

general, they do not have to coincide both in terms of the value and the nature of the gap.

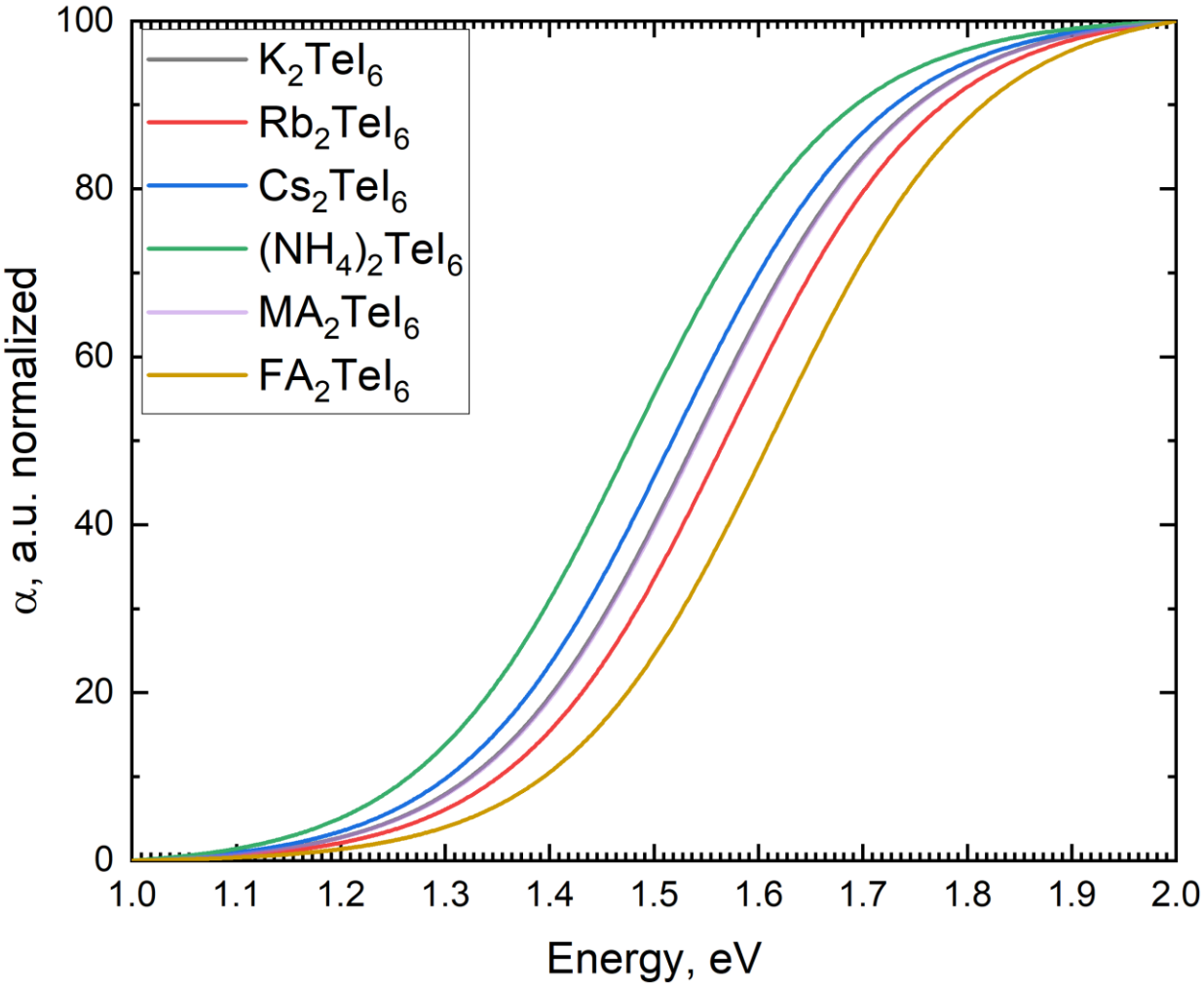

Figure 22. Boltzmann fitting of $\alpha(E)$ for A_2TeI_6. Coefficients $E_0(\mathrm{K}) = 1.54eV$, $E_0(\mathrm{Rb}) = 1.57eV$, $E_0(\mathrm{Cs}) = 1.52eV$, $E_0(NH_4) = 1.48eV$, $E_0(MA) = 1.54eV$, $E_0(FA) = 1.61eV$ $\delta E = 0.1$

4.2.5 Photoluminescence

Indirectly, we can often relate optical band gap type with PL signal intensity: direct band-gaps usually display a much higher PL signal than indirect ones. Our room temperature PL experiment has not detected any PL signals for A_2TeI_6 and A_2TeBr_6 compounds, but we detected strong PL signals for A_2TeCl_6 (Figure A3.4). Despite contradiction with the results of Ju et al., our data corresponds to other published data for the same type of compounds include hybrid organic-

inorganic cases.[140,141] Sedakova et al. showed a correlation of the PL signal intensity with a size of $[TeX_6]^{2-}$ coordination polyhedron and an increase in the A band energy.[140]

Our hypothesis about the detected by Ju et al. PL signal in the hydrothermally grown crystals is related to use hydrochloride salts as A cation sources. Cl^- impurities in the crystals might be a source of PL signal, and it corresponds to data about strong PL signal of A_2TeCl_6 compounds.

Strong PL signal of Cl-based compounds supports the idea of direct band-gap and, at the same time, it is hard to presume change of band-gap type inside A_2TeX_6 subfamily with change only X halide without change type of the structure

4.2.6 Theoretical analysis

Ju et al. also supported their result by DFT calculations of the indirect band-gap. To make a cross-check of these results, we performed the analog calculation of the band structures but for Cs_2TeX_6 and FA_2TeX_6.

For the symmetrical cubic structures of Cs_2TeBr_6 determined from the XRD analysis, the band-gap is formally indirect (Γ – L), even though the difference between direct and indirect gaps is small (around 0.3 eV), as demonstrated in Figure 23a. The inclusion of the spin-orbit coupling effect even slightly decreases this difference between direct and indirect band gaps to around 0.2 eV (Figure 23b).

Including finite temperature effects at 300 K enables a realization of Cs_2TeBr_6 structures with more minor differences between direct and indirect band gaps (Figure 23c). Lattice dynamics at finite temperature further decreases the difference between Γ – L and Γ – Γ gaps, making the top of the valence band even more flat (Figure 23d). This observation suggests that for these compounds, the electronic structure of instantaneous configurations accessible at a finite temperature can be different from that of perfectly symmetric cubic ones, which are defined by XRD analysis.

For FA_2TeBr_6 with randomized FA orientations, the top of the valence band becomes flat in a way that the difference between direct and indirect band gaps is smaller than 0.1 eV (Figure 24).

As a hypothesis, at finite temperature, the realizations of direct and indirect band gaps are indistinguishable in the experimental spectrum, as the difference between direct and indirect gaps is very small, not exceeding 0.1 eV (Figure 23 and 24).

As expected, the valence band maximum is formed mainly by the halide states, while both halide and Te states create the bottom of the conduction band. 3p, 4p, and 5p states of Cl, Br, and I, respectively, contribute both to the valence band maximum and conduction band minimum. Te 5p states are forming the bottom of the conduction band together with halide np states, while in the valence band, there is a small contribution of Te 5s for halide, bromide, and iodide compounds. The contribution of halide into the bottom of the conduction band is increasing in a row Cl – Br – I, as compared to Te contribution. Above these Te – X states, there are states centered on the monovalent cation Cs.

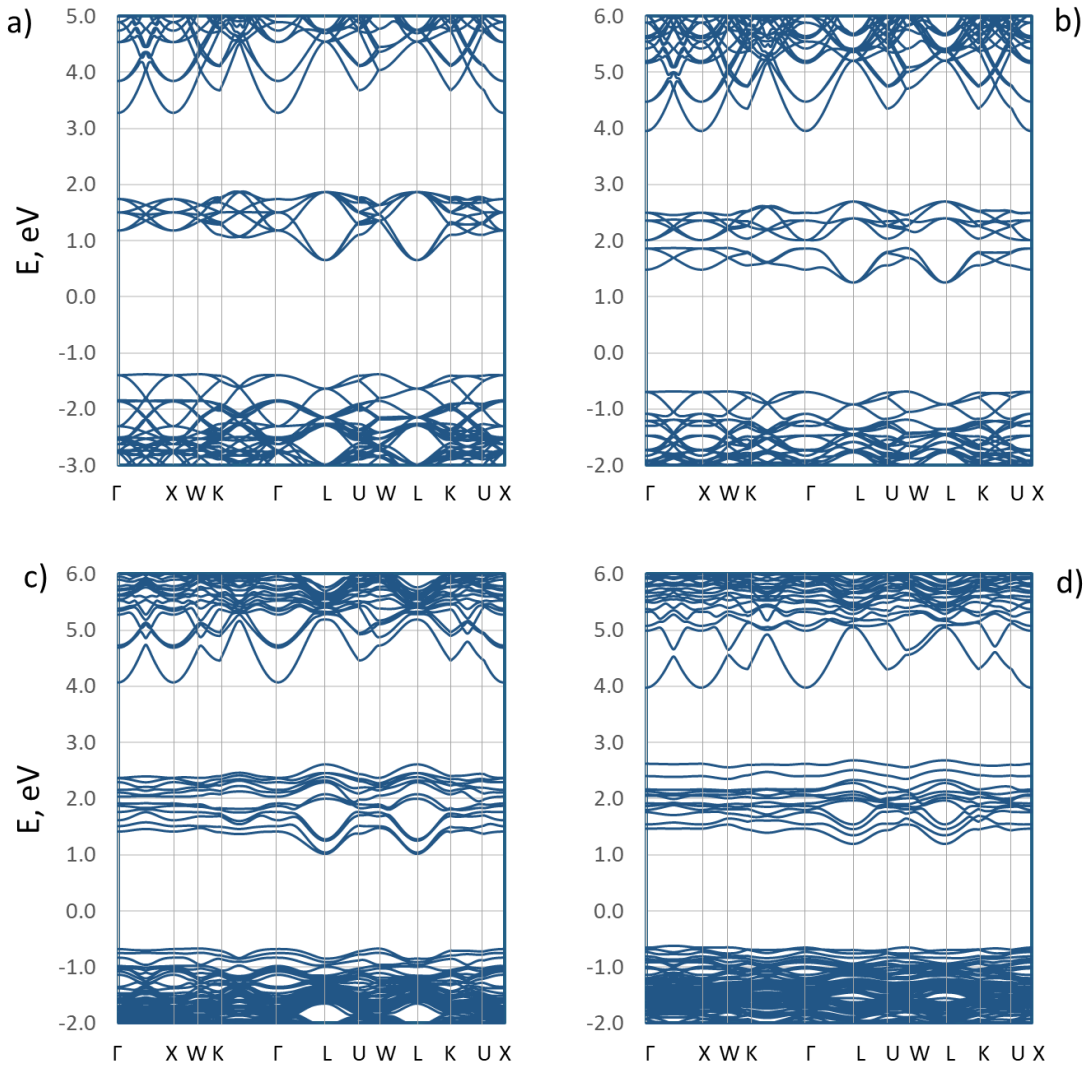

Figure 23. Cs_2TeBr_6 band structure variants. (a) Band structure of perfectly cubic Cs_2TeBr_6 structure without spin-orbit coupling; (b) Band structure of perfectly cubic Cs_2TeBr_6 structure with spin-orbit coupling; (c) Band structure of Cs_2TeBr_6 for a dynamics snapshot at 300K and experimental lattice parameters; (d) Band structure of Cs_2TeBr_6 for a dynamics snapshot at 300K and 1 atm. In all cases, the Fermi level is set to 0 eV. All crystal and electronic structures are obtained with PBE density functional.

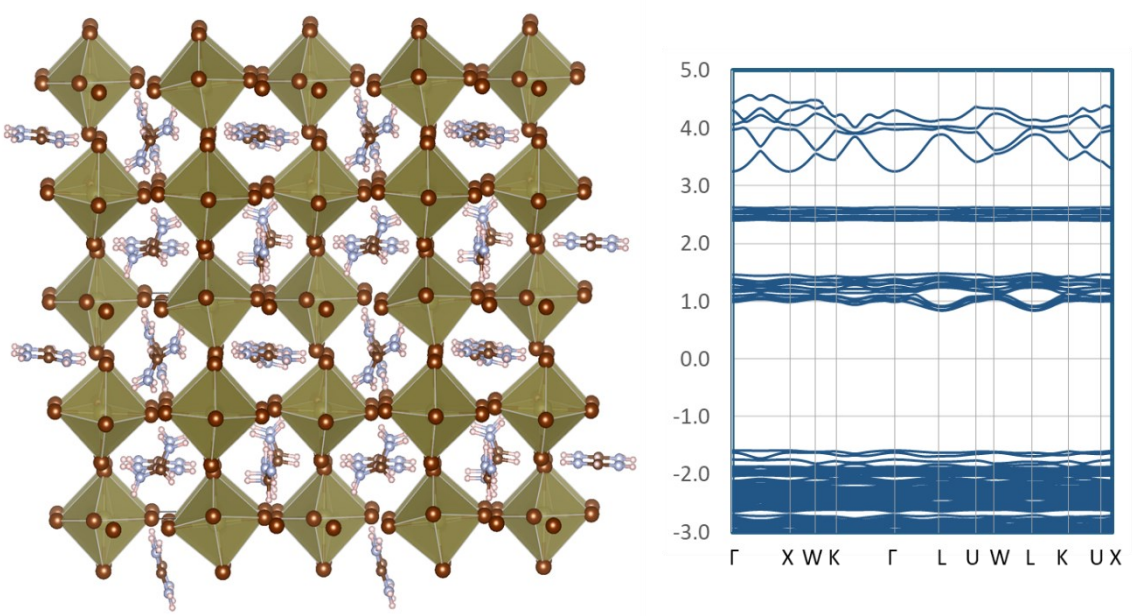

Figure 24. Crystal (left) and band (right) structure of pseudo-cubic FA_2TeBr_6 with randomized orientations of FA. The structure is obtained for 0K.

Such a slight difference between the direct and indirect band-gap accentuates the problem of its accurate definition.

To try to specify the situation, we attempt to simulate optical spectra of these compounds. We computed the ranges within the linear-response time-dependent density functional theory (LR-TDDFT). The shape of the spectra is susceptible to the inclusion of local field effects (LFE). By local effects, here, the inhomogeneity of the dielectric matrix is meant, which is accounted for by the inversion of this matrix in the calculation. In general, LFE is important for layered or 2D systems, while for classical halide perovskites, spectra with and without LFE are usually similar. However, this is not the case in the considered A_2TeX_6.

Without LFE, near the onset, there is a broad peak, which can also split into two extremes. A strong and sharp absorption peak at ~2.0 eV above the spectral onset is observed only in a case when local field effects are included in the calculation (Figure 25). The position of this peak gradually shifts down within the anionic row Cl – Br – I (Figure 26).

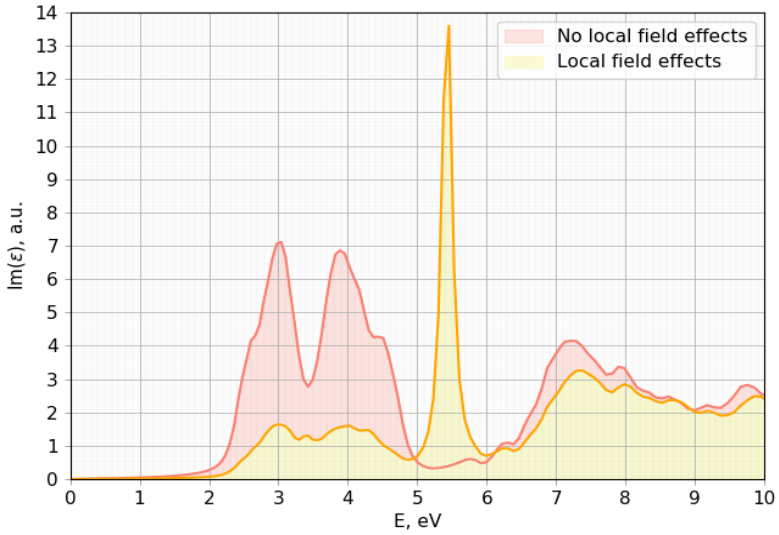

Figure 25. Optical spectrum (imaginary part Im(ε) of the dielectric function) of Cs_2TeBr_6 computed with (yellow) or without (red) local field effects.

We need to note that part of the simulated spectra above ~5.5eV might be non-relevant due to the predominance of non-linear processes uncounted in the applied model.

The top of the valence band in A_2TeX_6 double perovskites is formed by the states localized mainly on the halide atoms X, while the bottom of the conduction band is constructed from the orbitals of both Te and halide atoms. P-states of halides contribute both to the valence band maximum and conduction band minimum. Te 5p states are forming the bottom of the conduction band together with halide np states, while in the valence band, there is a small contribution of Te 5s (Figures 27, 28).

On top of these states in the conduction band, there is an exciting feature formed by the states localized in the vicinity of monovalent cation A (around 1 eV above CB edge). These states have a relatively high dispersion that implies high electron mobility. Besides, they are separated by an energy gap from the conduction band edge that means that the carrier relaxation from these states to the CB edge is slowed down and that the carrier lifetime is higher than in a typical perovskite with a continuous conduction band.

Also, the electronic structure of A_2TeX_6 might allow extracting hot carriers. Figure 29 presents the electronic structure features of A_2TeX_6 with possible implications for solar cells based on hot carrier extraction from the second manifold of the conduction band (3-5 eV region on Figure 29). These states' dispersion (parabolicity) implies low effective mass and, therefore, high carrier mobility. Besides, the energy gap a priori slows down the electron transition between two CB manifolds and thus extends the charge carrier lifetimes at the bottom of the 2nd CB manifold. This implies that the hot electrons could be directly extracted from these states to the electrode before reaching the conduction band bottom. For this purpose, the conduction band of the selected electron transporting material should be appropriately aligned with these states.

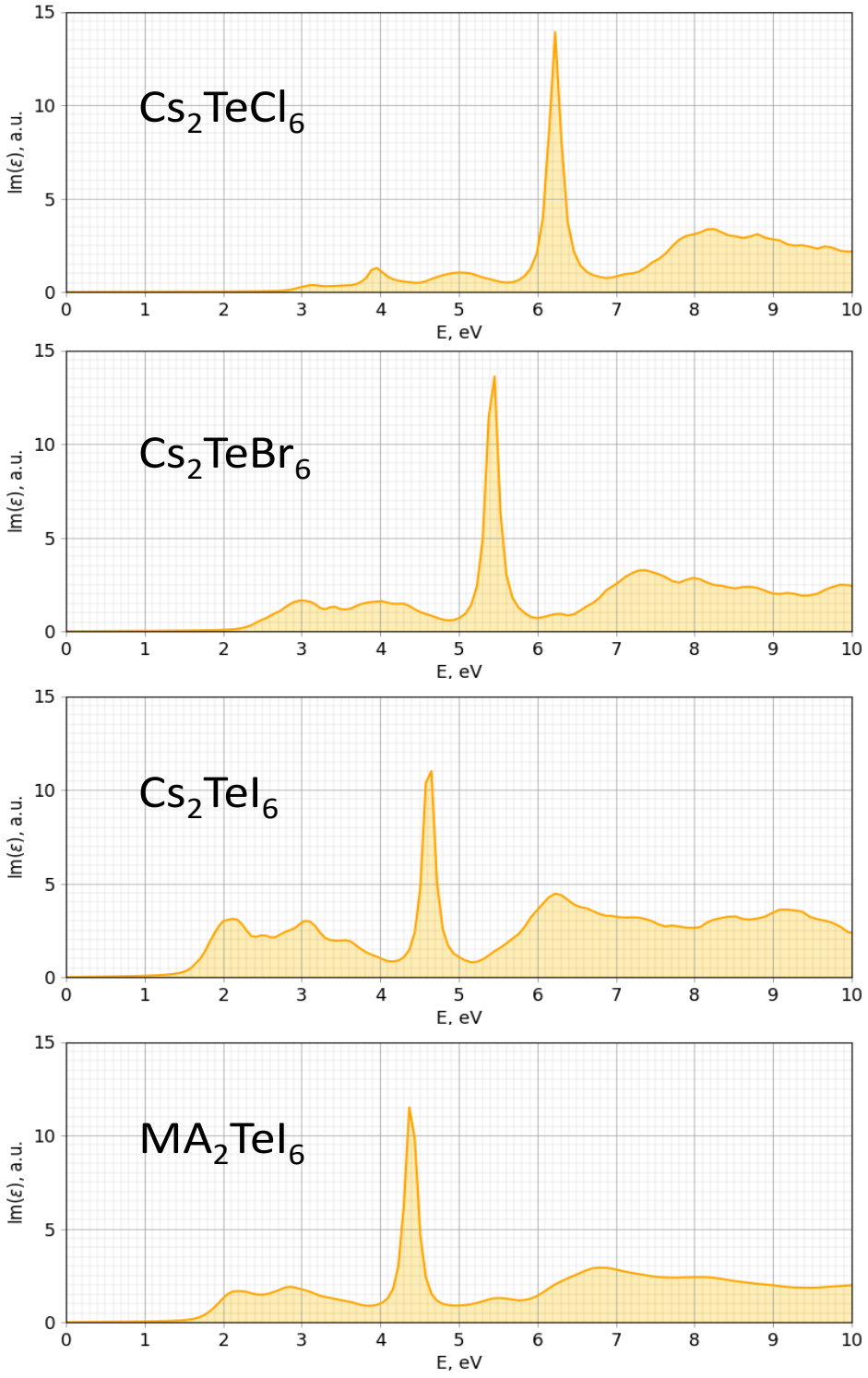

Figure 26. The optical absorption spectrum of the A_2TeX_6compounds, where A=Cs, MA; X=Cl, Br, I (Im(ε) – imaginary part of the dielectric function, proportional to the absorption coefficient α). The broadening parameter equals 0.08 eV.

Also, we evaluated the energy of vacancy formation. It may be of interest due to a report about low (relative to ABX_3 perovskites) defect tolerance. We calculated

the energies of vacancy formation in Cs_2TeX_6 and FA_2TeX_6 compounds, where $X = Cl, Br, I$ in the clamped nuclei approximation setting the reference of the chemical potential to the energy of isolated species, forming the vacancies. The defects are assumed to be neutral. The corresponding values are presented in Table 5 for A_2TeX_6.

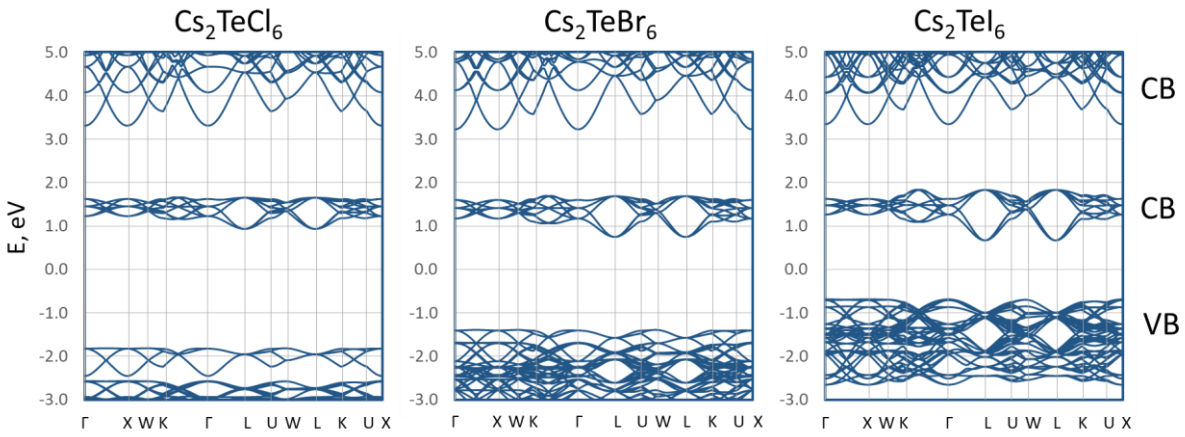

Figure 27. Band structure for Cs_2TeX_6 compounds calculated with PBE density functional without spin-orbit coupling. All atomic positions and lattice parameters are relaxed with PBE. Fermi energy is set to 0 eV.

	The formation energy of a defect, eV		
Compound	Vac_X $(X = Cl, Br, I)$	Vac_A $(A = Cs, FA)$	Vac_{Te}
Cs_2TeCl_6	3.6	5.6	10.4
Cs_2TeBr_6	2.9	5.4	8.5
Cs_2TeI_6	2.4	4.8	6.6
FA_2TeCl_6	3.5	5.7	10.8
FA_2TeBr_6	3.0	5.4	9.0
FA_2TeI_6	2.3	4.8	7.0

Table 5. Vacancy formation energies for A_2TeX_6 double perovskite compounds at clamped nuclei approximation, calculated with PBE density functional.

At the reference, chemical potentials are equal respectively to the energy of an isolated species for each type of vacancy. For the clamped nuclei approximation, the easiest vacancy to be formed is halide vacancy. In Cl – Br – I halide series, the easiest vacancy to form is I one. It is followed by the monovalent cation vacancy, which is on average 2 eV higher in energy. The Te vacancy is the hardest to form. They are slightly more challenging to create in FA_2TeX_6as compared to Cs_2TeX_6, at least under-considered approximations. Cs and FA vacancies have similar energies assuming clamped nuclei. For both $Cs_2TeX_6$and FA_2TeX_6 compounds, the defect formation energies are close for each kind of species. Interestingly, all types of vacancies have lower formation energies in iodine perovskites. Indeed, all formation energies are decreasing in a row Cl – Br – I.

Meanwhile, it should be borne in mind that for different chemical potentials, the corresponding formation energies can vary, as formation energies are dependent on a particular chemical environment, defined by the chemical potentials of species forming the defect. We found interesting a possible correlation between change of vacancy energy formation and noted above PL signal change if we assume that vacancies might be a part of the PL suppression mechanism.

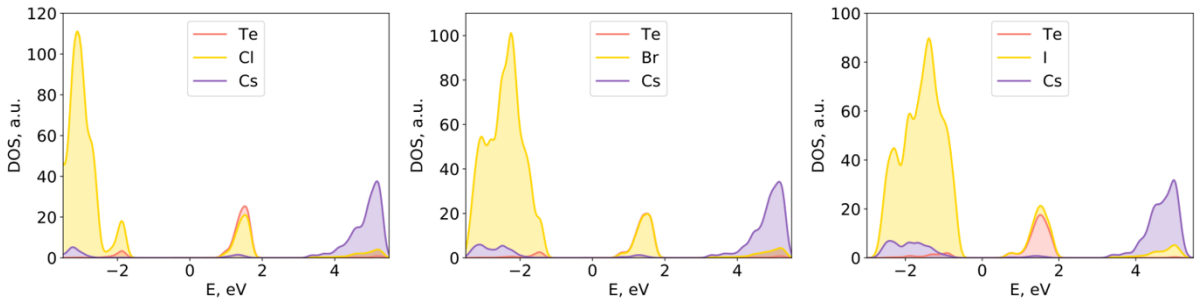

Figure 28. Densities of states in Cs_2TeX_6compounds calculated with PBE density functional without spin-orbit coupling. All atomic positions and lattice parameters are relaxed with PBE. Fermi energy is set to 0 eV.

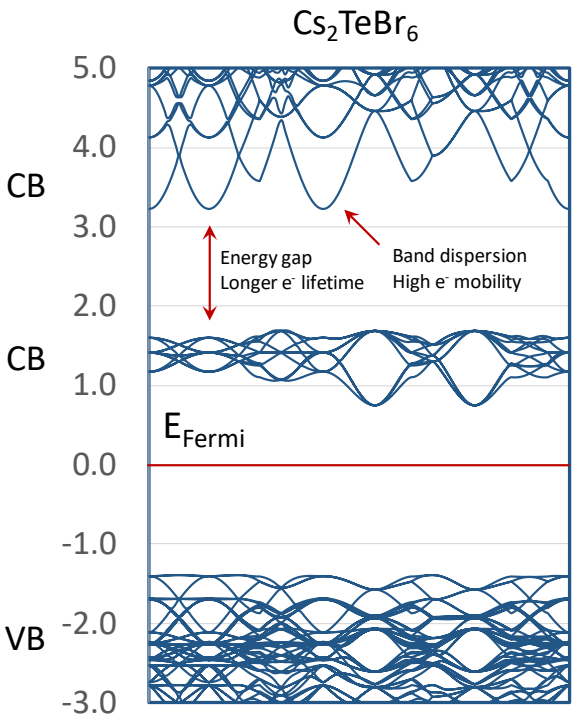

Figure 29. Specific electronic structure features of the double perovskites A_2TeX_6.

The complexity of the correct absorbance and band-gap definition is not limited only by noted factors. Vázquez-Fernández et al. in their report about Cs_2TeI_6 thin films have noted the change of the absorption spectra and the band-gap shift depend on the used anti-solvent.[147] Possible change of properties depending on the manufacturing process allows broad tuning for material optimization, but it increases the complexity of its understanding.

4.2.7 Other experimental data

Because of the change research target due to discovered data inconsistency, some experiments were put outside the mainline. However, we would like to include them as potentially interesting for further applied research.

We successfully deposited thin films of Rb_2TeI_6, Cs_2TeI_6, and MA_2TeI_6 via an RF magnetron-sputtering process. We used two compress powder targets: TeI_4 and $RbI/CsI/MAI$. The structure of thin films was confirmed by XRD. We noted the surprisingly high deposition rate and the high corrosive activity of the plasma during the sputtering process.

Following UPS experiment for Rb_2TeI_6 and MA_2TeI_6 displayed unusual deep VBM (Figure A3.6), e.g. 6.9 eV for MA_2TeI_6 . The deep levels might be a problem for further device engineering and choosing adequate hole and electron transport materials.

4.3. Conclusion

In the study, we displayed the problem of unequivocal optical band gap definition for the A_2TeX_6 compounds. Despite the wide use of Tauc plots, the techniques are still based on simplified models, and sometimes, like in our case, they might fault; the result directly relates to choosing the absorption coefficient model. Comparing with Boltzmann's fitting applied to clarify the situation, it better corresponds to direct band gaps. PL data also support this point of view. However, this result is not guaranteed because of the small difference between direct and indirect cases; minor structural and compound variations might change the balance. It might make the A_2TeX_6 family unique optoelectronic materials with easy tunable band-gap type.

We would like to highlight the specific complexity of A_2TeX_6 semiconductors. Future research of the subfamily requires a wide range of experiments to form the union picture of these semiconductors' properties.

Future research of the question needs to be done with the use of alternative experiments to determine the band-gap, such as the 4-probe technique. Using ARPES also might be a continuation of the band structure research. Also, it might expand the results of the study to other vacancy-ordered A_2BX_6 perovskites.

Chapter 5. Conclusion and future perspectives

In this chapter, I would like to highlight and summarize the outcome of discussed studies and my view about further perspectives for each of them. During my work on the thesis, I have changed my view about the anticipated results of the research multiple times. Unexpected difficulties of various nature - from technical and safety problems to profound fundamental limits. Some issues were solved, others still stay open - all they shaped the outcome of my research.

In chapter 2, I described the generalized way to predict the formation of vacancy-ordered double perovskites. During my pre-research literature review, I did not find any other model to forecast it. The proposed technique logically followed and broadened the geometrical factor approach widely used for classic perovskites. Simplicity and ease of use are the main great advantages of the method.

However, the result opens new questions. I formulate them as: Why the optimal value of the t factor is shifted depending on halide? How to predict the factor value and its shift? Why is the blurring of the border is different for different halides? How will it work for crystal with mixed halides, e.g. $A_2BX_yX_z$ $(y + z = 6)$? I assume that answers to the questions might come from further research to understand the sum of factors that define the crystal formation process. This way could be easily connected with general questions of crystal formation and crystallography. Of course, this kind of prediction model will not be simple, but it might have higher accuracy and potentially be connected with other physicochemical properties of a crystal.

In chapter 3, I actually presented a new way that describes the complex model of perovskite crystal formation. The creation of the mentioned above complex crystal formation models might be extremely labor-intensive in the case of using 'classic' approaches such as, for example, first-principles-based ones. An alternative gaining popularity methodology based on using artificial neural networks (ANNs)

(also called deep learning (DL)) is easier to design. DL is related to the family of machine learning techniques, but in contrast to many others, it has a lower requirement to feature engineering, and it can better fit non-linear systems.

The result models demonstrated unexpected good results: The forecasted results showed high accuracy to the used dataset. Moreover, an investigation of the counter cases showed that the forecasted results for some compounds were right, and the original dataset was not full. In other words, the model successfully forecasted the results that were not experimentally confirmed (at the moment of the dataset creation) and were not fully correctly labeled in the original dataset. It demonstrates the significant forecasting ability of the ANNs in the crystal formation field.

Of course, there are still many open questions, for example, about the exact prediction algorithm of the created models. Unfortunately, an ANN is a "black box", and it requires special complex further investigation to try to understand the logic behind it. I find it promising to further research to try to use the DL technique to forecast other properties of perovskites compounds. Creating ANN-based models to predict the formation of other perovskite-like compounds is also a perspective. First attempts to apply the technique for the dataset of vacancy-ordered double-perovskites from chapter 2 were successful and showed an accuracy rate of over 90%. From an experimental point of view, I expect it might be useful to recheck cases predicted as perovskites but contradict the original dataset, especially ones predicted by few models.

In chapter 4, I chose an experimental way to study novel lead-free tellurium-based compounds. My initial target was to study the necessary properties of the materials and use them to design a prototype of a lead-free Te-based solar cell. Of course, I understand that tellurium might not be an excellent material to change for lead because of non-zero toxicity and rareness. Nevertheless, Te-based vacancy ordered perovskites are much easier to synthesis than, e.g., A_2TiX_6 or A_2WX_6. At the same time, it might be suitable for the first steps to research vacancy ordered

perovskites for optoelectronics. However, I found a massive line of challenges on the way, from the necessity of using hydrohalic acids for synthesis to low solubility and high sensitivity to the humidity of solutions. These facts make it hard to produce thin films via spin-coating in analog with Pb-based halide perovskites. In the end, searching for an alternative lead me to use RF magnetron sputtering. Unfortunately, the used variant was extremely resource-intensive (~2-3 grams of the stochiometric precursors' powder mixture for the formation of 4cm^2 of the thin film). The high corrosive activity of the plasma during the sputtering process makes it difficult to switch to a machine with higher intensity. Choosing optimal hole and electron transport materials also became a challenge regarding the deepness of the conduction and valence bands from the UPS experiment. The complexity of research physicochemical does not simplify the situation. As described in the chapter, the problem of definition band gaps type might indicate to unusual electronic structure for these semiconductors.

I see the future of the research Te-based perovskites in two different branches. The first one is focused on designing a solar cell prototype. It will require search an optimal way of thin-film production for manufacturing a vast number of samples. It is necessary for the experimental search of effective interface semiconductor-charge transport material. The quality of the thin films also might be a challenge. The second one is focused on deep research of the materials' electronic structure. It will require to use of experimental techniques such as XPS, ARPES, and the 4-probe method. Samples noted above are also necessary to perform these experiments; moreover, the ARPES experiment requires growing big (1-2cm) single crystal. Advanced calculations also might help shed light on the question.

To summarize, I found and passed the way full of complex and exciting challenges. I significantly strayed from my initial idea to go through the whole process from material synthesis to a PV device prototype; however, I assume it was an integral part of the scientific search. I hope that the outcome will be helpful

for the next researchers in the field, and my work will be a small but solid brick in the infinite tower of science.

Appendices

Appendix A

No	*Compound*	*Space Group*	*Structure type*	*t*	*μ*	*Ref*
			A_2BI_6			
1	K_2TeI_6	P 1 21/n 1	K_2SnCl_6(LT)	0,7985	0,4409	[148]
2	Tl_2TeI_6	P 1 21/n 1	K_2SnCl_6 (LT)	0,8253	0,4409	[149]
3	Rb_2TeI_6	P 4/m n c	K_2SnCl_6	0,8298	0,4409	[150]
4	Na_2UI_6	R -3 H	Na_2UI_6	0,7369	0,4046	[151]
5	$(NH_4)_2TeI_6$	P 1 21/n 1	K_2SnCl_6 (LT)	0,8097	0,4409	[152]
6	Li_2UI_6	P -3 1 c	$CaLiAlF_6$	0,6774	0,4046	[153]
7	K_2TcI_6	P 1 21/n 1	K_2SnCl_6 (LT)	0,8898	0,2932	[154]
8	K_2PtI_6	P 4/m n c	K_2SnCl_6	0,8961	0,2841	[155]
9	K_2ReI_6	P 1 n 1	**no prototype**	0,8945	0,2864	[156]
10	Rb_2SnI_6	F m -3 m	K_2PtCl_6	0,9102	0,3136	[157]
11	Cs_2TeI_6	F m -3 m	K_2PtCl_6	0,8633	0,4409	[158]
12	Cs_2HfI_6	F m -3 m	K_2PtCl_6	0,9404	0,3227	[159]
13	Cs_2SnI_6	F m -3 m	K_2PtCl_6	0,9469	0,3136	[160,161]
14	Rb_2PtI_6	F m -3 m	K_2PtCl_6	0,9311	0,2841	[155]
15	Cs_2PtI_6	F m -3 m	K_2PtCl_6	0,9687	0,2841	[155,159]
16	Rb_2PdI_6	F m -3 m	K_2PtCl_6	0,9344	0,2796	[162]
17	Cs_2PdI_6	F m -3 m	K_2PtCl_6	0,9721	0,2796	[163]
18	Cs_2PoI_6	F m -3 m	K_2PtCl_6	0,8715	0,4273	[164]
19	$(NH_4)_2ReI_6$	P 4/m n c	$(Cs,NH_4)_2TeCl_4Br_2$	0,907	0,2864	[156]
20	$(NH_4)_2PtI_6$	F m -3 m	K_2PtCl_6	0,9086	0,2841	[155]
			A_2BBr_6			
21	$(NH_4)_2TeBr_6$	F m -3 m	K_2PtCl_6	0,8181	0,4949	[165]
22	Na_2UBr_6	P -3 m 1	Li_2MnF_6	0,7394	0,4541	[166]
23	Li_2UBr_6	P -3 1 c	$CaLiAlF_6$	0,6748	0,4541	[167]
24	Cs_2TeBr_6	F m -3 m	K_2PtCl_6	0,876	0,4949	[165,168]
25	Rb_2TeBr_6	F m -3 m	K_2PtCl_6	0,8398	0,4949	[169]
26	Tl_2TeBr_6	F m -3 m	K_2PtCl_6	0,835	0,4949	[149]
27.1	Rb_2UBr_6	F m -3 m	K_2PtCl_6	0,8634	0,4541	[170]
27.2	Rb_2UBr_6	P 4/m n c	K_2SnCl_6 *(LT)*	0,8634	0,4541	[171]
28	K_2TeBr_6	P 1 21/n 1	K_2SnCl_6 *(LT)*	0,8061	0,4949	[172]
29.1	K_2SnBr_6	F m -3 m	K_2PtCl_6	0,8912	0,352	[173]
29.2	K_2SnBr_6	P 1 21/n 1	K_2SnCl_6 *(LT)*	0,8912	0,352	[174]

30	Rb_2SnBr_6	F m -3 m	K_2PtCl_6	0,9286	0,352	[173]
31	Cs_2SnBr_6	F m -3 m	K_2PtCl_6	0,9686	0,352	[173]
32	Rb_2WBr_6	F m -3 m	K_2PtCl_6	0,9392	0,3367	[175]
33	Cs_2WBr_6	F m -3 m	K_2PtCl_6	0,9797	0,3367	[176]
34	K_2ReBr_6	F m -3 m	K_2PtCl_6	0,9119	0,3214	[177,178]
35	K_2OsBr_6	F m -3 m	K_2PtCl_6	0,9119	0,3214	[179]
36	K_2PtBr_6	F m -3 m	K_2PtCl_6	0,9136	0,3189	[178]
37	Cs_2PtBr_6	F m -3 m	K_2PtCl_6	0,993	0,3189	[180]
38	Rb_2PdBr_6	F m -3 m	K_2PtCl_6	0,9556	0,3138	[181]
39	Cs_2PdBr_6	F m -3 m	K_2PtCl_6	0,9968	0,3138	[182]
40	K_2SeBr_6	F m -3 m	K_2PtCl_6	0,9601	0,2551	[183]
41	Cs_2UBr_6	F m -3 m	K_2PtCl_6	0,9006	0,4541	[170]
42	$(NH_4)_2PoBr_6$	F m -3 m	K_2PtCl_6	0,8266	0,4796	[168]
43	$(NH_4)_2SnBr_6$	F m -3 m	K_2PtCl_6	0,9046	0,352	[173]
44	$(NH_4)_2NbBr_6$	F m -3 m	K_2PtCl_6	0,908	0,3469	[184]
45	$(NH_4)_2TiBr_6$	F m -3 m	K_2PtCl_6	0,9345	0,3087	[185]
46	$(NH_4)_2SeBr_6$	F m -3 m	K_2PtCl_6	0,9744	0,2551	[186,187]
A_2BCl_6						
47	K_2TeCl_6	I 1 2/m 1	*no prototype*	0,8114	0,5359	[188]
48	Cs_2CeCl_6	P -3 m 1	K_2GeF_6	0,9182	0,4807	[189]
49	Cs_2ThCl_6	P -3 m 1	K_2GeF_6	0,8948	0,5193	[190]
50	Li_2UCl_6	P 63/m m c	*no prototype*	0,6731	0,4917	[191]
51	Na_2UCl_6	P -3 m 1	Li_2MnF_6	0,7412	0,4917	[191]
52	Cs_2UCl_6	P -3 m 1	K_2GeF_6	0,9114	0,4917	[190,192]
53	Cs_2TeCl_6	F m -3 m	K_2PtCl_6	0,8852	0,5359	[193]
54	Rb_2PbCl_6	F m -3 m	K_2PtCl_6	0,9109	0,4282	[188,193]
55	Cs_2PbCl_6	F m -3 m	K_2PtCl_6	0,9519	0,4282	[188,193]
56	Rb_2TeCl_6	F m -3 m	K_2PtCl_6	0,847	0,5359	[188,193,194]
57	Rb_2ZrCl_6	F m -3 m	K_2PtCl_6	0,9307	0,3978	[188]
58	Tl_2TeCl_6	F m -3 m	K_2PtCl_6	0,8419	0,5359	[188]
59	Tl_2SnCl_6	F m -3 m	K_2PtCl_6	0,9362	0,3812	[188]
60	Rb_2SnCl_6	F m -3 m	K_2PtCl_6	0,9419	0,3812	[100,188,193]
61	Cs_2SnCl_6	F m -3 m	K_2PtCl_6	0,9843	0,3812	[100,188,193]
62	K_2TaCl_6	F m -3 m	K_2PtCl_6	0,9059	0,3757	[195]
63	Cs_2TaCl_6	F m -3 m	K_2PtCl_6	0,9882	0,3757	[196]
64	K_2WCl_6	F m -3 m	K_2PtCl_6	0,9132	0,3646	[197]
65	Tl_2WCl_6	F m -3 m	K_2PtCl_6	0,9476	0,3646	[198]
66	Rb_2WCl_6	F m -3 m	K_2PtCl_6	0,9533	0,3646	[199]

67	Cs_2WCl_6	F m -3 m	K_2PtCl_6	0,9962	0,3646	[200]
68	K_2MoCl_6	F m -3 m	K_2PtCl_6	0,9169	0,3591	[201]
69	Tl_2MoCl_6	F m -3 m	K_2PtCl_6	0,9514	0,3591	[202]
70	Cs_2MoCl_6	F m -3 m	K_2PtCl_6	1,0085	0,3591	[203]
71	K_2TcCl_6	F m -3 m	K_2PtCl_6	0,9188	0,3564	[204]
72	Ag_2ReCl_6	R -3 H	Na_2UI_6	0,8578	0,3481	[205]
73	K_2ReCl_6	F m -3 m	K_2PtCl_6	0,9245	0,3481	[206]
74	Cs_2ReCl_6	F m -3 m	K_2PtCl_6	1,0085	0,3481	[207]
75	K_2OsCl_6	F m -3 m	K_2PtCl_6	0,9245	0,3481	[179]
76	Cs_2IrCl_6	F m -3 m	K_2PtCl_6	1,0106	0,3453	[208]
77	K_2PtCl_6	F m -3 m	K_2PtCl_6	0,9264	0,3453	[181,209,210]
78	Tl_2PtCl_6	F m -3 m	K_2PtCl_6	0,9612	0,3453	[188]
79	Rb_2PtCl_6	F m -3 m	K_2PtCl_6	0,967	0,3453	[188,193]
80	Cs_2PtCl_6	F m -3 m	K_2PtCl_6	1,0106	0,3453	[188,193]
81	K_2PdCl_6	F m -3 m	K_2PtCl_6	0,9302	0,3398	[173,211,212]
82	Cs_2ZrCl_6	F m -3 m	K_2PtCl_6	0,9726	0,3978	[188]
83	K_2TiCl_6	F m -3 m	K_2PtCl_6	0,934	0,3343	[213]
84	Rb_2TiCl_6	F m -3 m	K_2PtCl_6	0,975	0,3343	[188]
85	Cs_2TiCl_6	F m -3 m	K_2PtCl_6	1,0189	0,3343	[188]
86	K_2MnCl_6	F m -3 m	K_2PtCl_6	0,964	0,2928	[214]
87	Rb_2MnCl_6	F m -3 m	K_2PtCl_6	1,0063	0,2928	[215]
88	Cs_2GeCl_6	F m -3 m	K_2PtCl_6	1,0516	0,2928	[216]
A_2BF_6						
89	Na_2ThF_6	P 3 2 1	Na_2ThF_6	0,732	0,7068	[217,218]
90	K_2ThF_6	P -6 2 m	K_2UF_6	0,8442	0,7068	[217,219]
91	Rb_2ThF_6	P -6 2 m	K_2UF_6	0,8878	0,7068	[220]
92.1	Na_2UF_6	P 3 2 1	Na_2ThF_6	0,7485	0,6692	[217]
92.2	Na_2UF_6	I m m m	**no prototype**	0,7485	0,6692	[217]
92.3	Na_2UF_6	P 3	**no prototype**	0,7485	0,6692	[221]
93.1	K_2UF_6	P -6 2 m	K_2UF_6	0,8632	0,6692	[217,222]
93.2	K_2UF_6	P 3 2 1	Na_2ThF_6	0,8632	0,6692	[217]
94	Rb_2UF_6	C m c m	K_2ZrF_6	0,9078	0,6692	[223]
95	Li_2TbF_6	P 1 2/c 1	Li_2TbF_6	0,7071	0,5714	[224]
96	K_2TbF_6	P 1 2/c 1	Li_2TbF_6	0,9169	0,5714	[225]
97	Rb_2TbF_6	C 1 2/c 1	K_2ZrF_6 *(C2/c)*	0,9642	0,5714	[225]
98.1	Li_2ZrF_6	P 1 21/c 1	Li_2TbF_6	0,7209	0,5413	[226]
98.2	Li_2ZrF_6	P -3 1 m	Li_2ZrF_6	0,7209	0,5413	[227,228]
99.1	K_2ZrF_6	C 1 2/c 1	K_2ZrF_6 *(C2/c)*	0,9348	0,5413	[229,230]

99.2	K_2ZrF_6	C m c m	K_2ZrF_6	0,9348	0,5413	[231]
99.3	K_2ZrF_6	C 2 2 21	*no prototype*	0,9348	0,5413	[232]
100	Rb_2ZrF_6	P -3 m 1	K_2GeF_6	0,9831	0,5414	[233]
101	Cs_2ZrF_6	P -3 m 1	K_2GeF_6	1,0348	0,5414	[233]
102	Li_2HfF_6	P -3 1 m	Li_2ZrF_6	0,7244	0,5338	[234]
103	K_2RhF_6	P -3 m 1	K_2GeF_6	0,9929	0,4511	[235]
104	Rb_2HfF_6	P -3 m 1	K_2GeF_6	0,9879	0,5338	[233]
105	Cs_2HfF_6	P -3 m 1	K_2GeF_6	1,0399	0,5338	[233]
106.1	Na_2SnF_6	P 42/m n m	$ZnSb_2O_6$	0,8226	0,5188	[236]
106.2	Na_2SnF_6	P 1 21/a 1	Na_2SnF_6	0,8226	0,5188	[237]
107	Tl_2SnF_6	P -3 m 1	K_2GeF_6	0,9907	0,5188	[238]
108	Cs_2SnF_6	P -3 m 1	K_2GeF_6	1,0502	0,5188	[239,240]
109	Li_2NbF_6	P -3 m 1	Li_2ZrF_6	0,7353	0,5113	[241]
110	Rb_2NbF_6	P -3 m 1	K_2GeF_6	1,0026	0,5113	[242]
111	Cs_2NbF_6	P -3 m 1	K_2GeF_6	1,0554	0,5113	[242]
112.1	Li_2MoF_6	P 42/m n m	$ZnSb_2O_6$	0,7464	0,4887	[243]
112.2	Li_2MoF_6	P 42 21 2	*no prototype*	0,7464	0,4887	[244]
113	Na_2TcF_6	P -3 m 1	K_2GeF_6	0,8414	0,485	[245]
114	Rb_2TcF_6	P -3 m 1	K_2GeF_6	1,0204	0,485	[245]
115	Cs_2TcF_6	P -3 m 1	K_2GeF_6	1,0741	0,485	[245]
116	K_2ReF_6	P -3 m 1	K_2GeF_6	0,9777	0,4737	[246]
117	Rb_2ReF_6	P -3 m 1	K_2GeF_6	1,0282	0,4737	[247]
118	Cs_2ReF_6	P -3 m 1	K_2GeF_6	1,0823	0,4737	[247]
119	K_2IrF_6	P -3 m 1	K_2GeF_6	0,9802	0,4699	[248]
120	Rb_2IrF_6	P -3 m 1	Rb_2IrF_6	1,0308	0,4699	[249]
121	Cs_2IrF_6	P -3 m 1	Rb_2IrF_6	1,0851	0,4699	[250]
122	Li_2PtF_6	P 1 21/a 1	Na_2SnF_6	0,7559	0,4699	[251]
123	K_2PtF_6	P -3 m 1	K_2GeF_6	0,9802	0,4699	[252,253]
124	Rb_2PtF_6	P -3 m 1	K_2GeF_6	1,0308	0,4699	[254]
125	$(NH_4)_2TcF_6$	P -3 m 1	K_2GeF_6	0,9882	0,9882	[245]
126.1	Li_2PdF_6	P 1 21/a 1	Na_2SnF_6	0,7598	0,4624	[251]
126.2	Li_2PdF_6	P 42/m n m	$ZnSb_2O_6$	0,7598	0,4624	[255]
127	K_2PdF_6	P -3 m 1	K_2GeF_6	0,9852	0,4624	[256]
128	Li_2CrF_6	P 1 21/a 1	Na_2SnF_6	0,7861	0,4135	[257]
129	$(NH_2)_4MnF_6$	P 63 m c	$(NH_4)_2SiF_6$	1,0493	0,3958	[258]
130	Li_2TiF_6	C 1 2/c 1	$Zn_4Ta_2O_9$	0,7637	0,4549	[259]
131.1	Na_2TiF_6	P 1	Na_2TiF_6	0,8588	0,4549	[260]
131.2	Na_2TiF_6	P -3 m 1	Li_2MnF_6	0,8588	0,4549	[261]

132	K_2TiF_6	P -3 m 1	K_2GeF_6	0,9903	0,4549	[262,263]
133	Tl_2TiF_6	P -3 m 1	K_2GeF_6	1,0342	0,4549	[238]
134.1	Li_2RhF_6	P 42/m n m	$ZnSb_2O_6$	0,7657	0,4511	[248,255]
134.2	Li_2RhF_6	P 1 21/c 1	Na_2SnF_6	0,7657	0,4511	[264]
135	Li_2SiF_6	P 3 2 1	Na_2SiF_6	0,8543	0,3008	[265]
136	Rb_2RhF_6	P -3 m 1	K_2GeF_6	1,0442	0,4511	[235]
137.1	Li_2VF_6	P 42/m n m	$ZnSb_2O_6$	0,7737	0,4361	[266,267]
137.2	Li_2VF_6	P 1 21/c 1	Na_2SnF_6	0,7737	0,4361	[266]
138	Cs_2VF_6	C c m m	*no prototype*	1,1106	0,4361	[268]
139.1	$(NH_4)_2ZrF_6$	P c a 21	$(NH4,K)_2ZrF_6$	0,952	0,5414	[269,270]
139.2	$(NH_4)_2ZrF_6$	P b a m	*no prototype*	0,952	0,5414	[232]
140	$(NH_4)_2TiF_6$	P -3 m 1	K_2GeF_6	1,0086	0,4549	[271]
141.1	Na_2SiF_6	P 3 2 1	Na_2SiF_6	0,9605	0,3008	[272–274]
141.2	Na_2SiF_6	P 1	Na_2TiF_6	0,9605	0,3008	[260]
141.3	Na_2SiF_6	P -3 m 1	Li_2MnF_6	0,9605	0,3008	[275]
142	Li_2MnF_6	P -3 m 1	Li_2MnF_6	0,7945	0,3985	[276]
143.1	K_2GeF_6	P -3 m 1	K_2GeF_6	1,0303	0,3985	[277]
143.2	K_2GeF_6	P 63 m c	K_2MnF_6	1,0303	0,3985	[278]
144.1	Li_2GeF_6	P 3 2 1	Na_2SiF_6	0,7945	0,3985	[279,280]
144.2	Li_2GeF_6	P 42/m n m	$ZnSb_2O_6$	0,7945	0,3985	[279]
145	$(NH_4)_2SnF_6$	P -3 m 1	K_2GeF_6	0,9661	0,5188	[281,282]
146.1	Na_2GeF_6	P 3 2 1	Na_2SiF_6	0,8934	0,3985	[280]
146.2	Na_2GeF_6	P -3 m 1	Li_2MnF_6	0,8934	0,3985	[275]
147.1	$(NH_4)_2GeF_6$	F m -3 m	K_2PtCl_6	1,0493	0,3985	[283]
147.2	$(NH_4)_2GeF_6$	P -3 m 1	K_2GeF_6	1,0493	0,3985	[277]
147.3	$(NH_4)_2GeF_6$	P 63 m c	$(NH_4)_2SiF_6$	1,0493	0,3985	[284]
148.1	Rb_2MnF_6	F m -3 m	K_2PtCl_6	1,0835	0,3985	[285–287]
148.2	Rb_2MnF_6	P 63 m c	K_2MnF_6	1,0835	0,3985	[285]
148.3	Rb_2MnF_6	R -3 m H	*no prototype*	1,0835	0,3985	[273]
149	K_2SiF_6	F m -3 m	K_2PtCl_6	1,1077	0,3008	[288–290]
150.1	K_2MnF_6	F m -3 m	K_2PtCl_6	1,0302	0,3985	[286]
150.2	K_2MnF_6	P 63 m c	K_2MnF_6	1,0302	0,3985	[273,285,291]
151.1	Rb_2GeF_6	F m -3 m	K_2PtCl_6	1,0835	0,3985	[292]
151.2	Rb_2GeF_6	P 63 m c	K_2MnF_6	1,0835	0,3985	[278]
151.3	Rb_2GeF_6	P -3 m 1	K_2GeF_6	1,0835	0,3985	[293]
152	K_2HfF_6	C 1 2/c 1	K_2ZrF_6(C2/c)	0,9393	0,5338	[294]
153.1	Cs_2PtF_6	F m -3 m	K_2PtCl_6	1,0851	0,4699	[295]
153.2	Cs_2PtF_6	P -3 m 1	K_2GeF_6	1,0851	0,4699	[254]

154	K_2NiF_6	F m -3 m	K_2PtCl_6	1,0587	0,3609	[296,297]
155	Cs_2CrF_6	F m -3 m	K_2PtCl_6	1,1284	0,4135	[298]
156	Cs_2GeF_6	F m -3 m	K_2PtCl_6	1,1405	0,3985	[299]
157	Rb_2NiF_6	F m -3 m	K_2PtCl_6	1,1134	0,3609	[298]
158	Cs_2NiF_6	F m -3 m	K_2PtCl_6	1,172	0,3609	[298]
159	Tl_2SiF_6	F m -3 m	K_2PtCl_6	1,1567	0,3008	[288,300]
160	Rb_2SiF_6	F m -3 m	K_2PtCl_6	1,1649	0,3008	[288]
161	Cs_2SiF_6	F m -3 m	K_2PtCl_6	1,2262	0,3008	[288,301]
162	Cs_2CoF_6	F m -3 m	K_2PtCl_6	1,1405	0,3985	[302]
163	Rb_2CoF_6	F m -3 m	K_2PtCl_6	1,0835	0,3985	[302]
164	Cs_2MnF_6	F m -3 m	K_2PtCl_6	1,1405	0,3985	[285,286]
165	$(NH_4)_2PtF_6$	F m -3 m	K_2PtCl_6	0,9983	0,4699	[303]
166	Rb_2CrF_6	F m -3 m	K_2PtCl_6	1,0719	0,4135	[298]
167	Cs_2PdF_6	F m -3 m	K_2PtCl_6	1,0907	0,4624	[304]
168	Rb_2PdF_6	F m -3 m	K_2PtCl_6	1,0361	0,4624	[304]
169.1	$(NH_4)_2SiF_6$	F m -3 m	K_2PtCl_6	1,1281	0,3008	[305,306]
169.2	$(NH_4)_2SiF_6$	P 63 m c	$(NH_4)_2SiF_6$	1,1281	0,3008	[307]
169.3	$(NH_4)_2SiF_6$	P -3 m 1	K_2GeF_6	1,1281	0,3008	[308,309]

Table A1.1. Studied A_2BX_6 compounds.

Appendix B

A	B	X	Group	PEROVSKITE	t	m
Li	Nb	O	A_2O-B_2O_5	0	0,75	0,51
Li	Ta	O	A_2O-B_2O_5	0	0,75	0,51
Li	V	O	A_2O-B_2O_5	0	0,79	0,43
Rb	Nb	O	A_2O-B_2O_5	0	1,03	0,51
Li	As	O	A_2O-B_2O_5	0	0,83	0,37
Rb	Ta	O	A_2O-B_2O_5	0	1,03	0,51
Cs	Nb	O	A_2O-B_2O_5	0	1,09	0,51
K	As	O	A_2O-B_2O_5	0	1,09	0,37
K	V	O	A_2O-B_2O_5	0	1,04	0,43
Na	As	O	A_2O-B_2O_5	0	0,94	0,37
Na	P	O	A_2O-B_2O_5	0	0,98	0,3
Cs	V	O	A_2O-B_2O_5	0	1,15	0,43
Cu	P	O	A_2O-B_2O_5	0	0,88	0,3
K	P	O	A_2O-B_2O_5	0	1,14	0,3
Li	P	O	A_2O-B_2O_5	0	0,87	0,3
Tl	Sb	O	A_2O-B_2O_5	0	1,05	0,48
Na	Sb	O	A_2O-B_2O_5	0	0,87	0,48
Li	Sb	O	A_2O-B_2O_5	0	0,77	0,48
K	Sb	O	A_2O-B_2O_5	0	1	0,48
Na	Bi	O	A_2O-B_2O_5	0	0,8	0,6
Li	Bi	O	A_2O-B_2O_5	0	0,71	0,6
Ag	Bi	O	A_2O-B_2O_5	0	0,84	0,6
K	Nb	O	A_2O-B_2O_5	1	0,98	0,51
K	Ta	O	A_2O-B_2O_5	1	0,98	0,51
Na	Nb	O	A_2O-B_2O_5	1	0,85	0,51
Na	Ta	O	A_2O-B_2O_5	1	0,85	0,51
K	U	O	A_2O-B_2O_5	1	0,92	0,6
Na	U	O	A_2O-B_2O_5	1	0,8	0,6
Na	W	O	A_2O-B_2O_5	1	0,86	0,49
Na	V	O	A_2O-B_2O_5	1	0,9	0,43
Ag	V	O	A_2O-B_2O_5	1	0,95	0,43
Ag	Ta	O	A_2O-B_2O_5	1	0,9	0,51
Ag	Nb	O	A_2O-B_2O_5	1	0,9	0,51
Cs	I	O	A_2O-B_2O_5	1	0,94	0,75
Tl	I	O	A_2O-B_2O_5	1	0,88	0,75

Rb	I	O	A_2O-B_2O_5	1	0,89	0,75
K	I	O	A_2O-B_2O_5	1	0,84	0,75
Ag	Sb	O	A_2O-B_2O_5	1	0,92	0,48
K	Bi	O	A_2O-B_2O_5	1	0,92	0,6
Ba	Ge	O	AO-BO_2	0	1,03	0,42
Ca	Si	O	AO-BO_2	0	0,96	0,32
Co	Ti	O	AO-BO_2	0	0,72	0,48
Mg	Ge	O	AO-BO_2	0	0,78	0,42
Mg	Ti	O	AO-BO_2	0	0,75	0,48
Mn	Ti	O	AO-BO_2	0	0,79	0,48
Zn	Ti	O	AO-BO_2	0	0,76	0,48
Fe	Ti	O	AO-BO_2	0	0,71	0,48
Ni	Ti	O	AO-BO_2	0	0,74	0,48
Fe	Si	O	AO-BO_2	0	0,8	0,32
Zn	Si	O	AO-BO_2	0	0,85	0,32
Mn	Ge	O	AO-BO_2	0	0,83	0,42
Mg	Sn	O	AO-BO_2	0	0,72	0,55
Sr	Si	O	AO-BO_2	0	1,04	0,32
Eu	Si	O	AO-BO_2	0	1,04	0,32
Sm	Si	O	AO-BO_2	0	1,04	0,32
Ba	Si	O	AO-BO_2	0	1,11	0,32
Co	Si	O	AO-BO_2	0	0,81	0,32
Sn	Pb	O	AO-BO_2	0	0,76	0,62
Ni	Si	O	AO-BO_2	0	0,83	0,32
Pb	Si	O	AO-BO_2	0	1,04	0,32
Mg	Si	O	AO-BO_2	0	0,84	0,32
Sr	Ge	O	AO-BO_2	0	0,96	0,42
Pb	Ge	O	AO-BO_2	0	0,97	0,42
Cd	Ge	O	AO-BO_2	0	0,93	0,42
Ca	Ge	O	AO-BO_2	0	0,89	0,42
Ba	Mn	O	AO-BO_2	0	1,03	0,42
Co	Mn	O	AO-BO_2	0	0,75	0,42
Ni	Mn	O	AO-BO_2	0	0,77	0,42
Sr	Mn	O	AO-BO_2	0	0,96	0,42
Ca	V	O	AO-BO_2	1	0,87	0,46
Sr	Hf	O	AO-BO_2	1	0,88	0,56
Ca	Mo	O	AO-BO_2	1	0,84	0,52
Ca	Ru	O	AO-BO_2	1	0,85	0,49

Ca	Sn	O	$AO\text{-}BO_2$	1	0,82	0,55
Sr	Ce	O	$AO\text{-}BO_2$	1	0,81	0,69
Sr	Ru	O	$AO\text{-}BO_2$	1	0,92	0,49
Sr	Sn	O	$AO\text{-}BO_2$	1	0,88	0,55
Ba	Ce	O	$AO\text{-}BO_2$	1	0,87	0,69
Sr	Zr	O	$AO\text{-}BO_2$	1	0,87	0,57
Sr	Pb	O	$AO\text{-}BO_2$	1	0,85	0,62
Sr	Ti	O	$AO\text{-}BO_2$	1	0,92	0,48
Ba	Nb	O	$AO\text{-}BO_2$	1	0,95	0,54
Ba	Sn	O	$AO\text{-}BO_2$	1	0,95	0,55
Ba	Zr	O	$AO\text{-}BO_2$	1	0,93	0,57
Sr	Mo	O	$AO\text{-}BO_2$	1	0,9	0,52
Sr	V	O	$AO\text{-}BO_2$	1	0,94	0,46
Ca	U	O	$AO\text{-}BO_2$	1	0,74	0,71
Ba	Th	O	$AO\text{-}BO_2$	1	0,84	0,75
Ba	U	O	$AO\text{-}BO_2$	1	0,86	0,71
Ca	Hf	O	$AO\text{-}BO_2$	1	0,81	0,56
Pb	Ce	O	$AO\text{-}BO_2$	1	0,81	0,69
Ba	Hf	O	$AO\text{-}BO_2$	1	0,94	0,56
Ca	Ti	O	$AO\text{-}BO_2$	1	0,85	0,48
Ca	Zr	O	$AO\text{-}BO_2$	1	0,81	0,57
Ba	Ti	O	$AO\text{-}BO_2$	1	0,99	0,48
Pb	Ti	O	$AO\text{-}BO_2$	1	0,93	0,48
Pb	Zr	O	$AO\text{-}BO_2$	1	0,87	0,57
Ba	Mo	O	$AO\text{-}BO_2$	1	0,95	0,54
Ba	Tb	O	$AO\text{-}BO_2$	1	0,91	0,6
Ba	Pr	O	$AO\text{-}BO_2$	1	0,87	0,67
Ba	Pb	O	$AO\text{-}BO_2$	1	0,9	0,62
Ca	Pb	O	$AO\text{-}BO_2$	1	0,78	0,62
Ca	Mn	O	$AO\text{-}BO_2$	1	0,89	0,42
La	B	O	$A_2O_3\text{-}B_2O_3$	0	1,09	0,18
Sc	B	O	$A_2O_3\text{-}B_2O_3$	0	0,95	0,18
Sm	B	O	$A_2O_3\text{-}B_2O_3$	0	1,05	0,18
Al	B	O	$A_2O_3\text{-}B_2O_3$	0	0,85	0,18
Ga	Al	O	$A_2O_3\text{-}B_2O_3$	0	0,74	0,43
Eu	Ln	O	$A_2O_3\text{-}B_2O_3$	Typo in original paper, ignored	0,76	0,63
Dy	B	O	$A_2O_3\text{-}B_2O_3$	0	1,03	0,18

Er	B	O	A_2O_3-B_2O_3	0	1,02	0,18
Eu	B	O	A_2O_3-B_2O_3	0	1,05	0,18
Gd	B	O	A_2O_3-B_2O_3	0	1,04	0,18
Ho	B	O	A_2O_3-B_2O_3	0	1,02	0,18
Y	B	O	A_2O_3-B_2O_3	0	1,03	0,18
Yb	B	O	A_2O_3-B_2O_3	0	1,01	0,18
Bi	Sm	O	A_2O_3-B_2O_3	0	0,73	0,76
V	Cr	O	A_2O_3-B_2O_3	0	0,71	0,49
V	Al	O	A_2O_3-B_2O_3	0	0,75	0,43
As	B	O	A_2O_3-B_2O_3	0	0,87	0,18
Gd	Y	O	A_2O_3-B_2O_3	0	0,72	0,71
Sm	Y	O	A_2O_3-B_2O_3	0	0,73	0,71
Tm	B	O	A_2O_3-B_2O_3	0	1,02	0,18
In	Cr	O	A_2O_3-B_2O_3	0	0,77	0,49
In	Fe	O	A_2O_3-B_2O_3	0	0,8	0,44
Sc	Al	O	A_2O_3-B_2O_3	0	0,79	0,43
Sc	Cr	O	A_2O_3-B_2O_3	0	0,76	0,49
La	Cr	O	A_2O_3-B_2O_3	1	0,86	0,49
La	Fe	O	A_2O_3-B_2O_3	1	0,89	0,44
La	V	O	A_2O_3-B_2O_3	1	0,85	0,51
Sm	Cr	O	A_2O_3-B_2O_3	1	0,83	0,49
Ce	V	O	A_2O_3-B_2O_3	1	0,84	0,51
Er	Fe	O	A_2O_3-B_2O_3	1	0,84	0,44
Er	V	O	A_2O_3-B_2O_3	1	0,8	0,51
Eu	Fe	O	A_2O_3-B_2O_3	1	0,86	0,44
Gd	Fe	O	A_2O_3-B_2O_3	1	0,86	0,44
Ho	Fe	O	A_2O_3-B_2O_3	1	0,84	0,44
La	Mn	O	A_2O_3-B_2O_3	1	0,88	0,46
La	Ti	O	A_2O_3-B_2O_3	1	0,84	0,53
Nd	Fe	O	A_2O_3-B_2O_3	1	0,88	0,44
Nd	Ni	O	A_2O_3-B_2O_3	1	0,87	0,44
Nd	Ti	O	A_2O_3-B_2O_3	1	0,82	0,53
Nd	V	O	A_2O_3-B_2O_3	1	0,83	0,51
Pr	Fe	O	A_2O_3-B_2O_3	1	0,88	0,44
Pr	Mn	O	A_2O_3-B_2O_3	1	0,86	0,46
Pr	Ni	O	A_2O_3-B_2O_3	1	0,87	0,44
Sm	Fe	O	A_2O_3-B_2O_3	1	0,87	0,44
Sm	Ni	O	A_2O_3-B_2O_3	1	0,86	0,44

Sm	Ti	O	A_2O_3-B_2O_3	1	0,81	0,53
Tb	Fe	O	A_2O_3-B_2O_3	1	0,85	0,44
Tb	V	O	A_2O_3-B_2O_3	1	0,81	0,51
Tm	Fe	O	A_2O_3-B_2O_3	1	0,84	0,44
Tm	V	O	A_2O_3-B_2O_3	1	0,8	0,51
Yb	Fe	O	A_2O_3-B_2O_3	1	0,83	0,44
Yb	V	O	A_2O_3-B_2O_3	1	0,79	0,51
Y	Cr	O	A_2O_3-B_2O_3	1	0,81	0,49
Y	Fe	O	A_2O_3-B_2O_3	1	0,84	0,44
Lu	Al	O	A_2O_3-B_2O_3	1	0,83	0,43
Y	Ti	O	A_2O_3-B_2O_3	1	0,79	0,53
Gd	Ti	O	A_2O_3-B_2O_3	1	0,81	0,53
Yb	Al	O	A_2O_3-B_2O_3	1	0,83	0,43
La	Al	O	A_2O_3-B_2O_3	1	0,9	0,43
Nd	Al	O	A_2O_3-B_2O_3	1	0,88	0,43
Bi	Fe	O	A_2O_3-B_2O_3	1	0,89	0,44
La	Co	O	A_2O_3-B_2O_3	1	0,89	0,44
La	Cu	O	A_2O_3-B_2O_3	1	0,81	0,58
La	Ni	O	A_2O_3-B_2O_3	1	0,89	0,44
Dy	Fe	O	A_2O_3-B_2O_3	1	0,85	0,44
Ce	Al	O	A_2O_3-B_2O_3	1	0,89	0,43
Ce	Cr	O	A_2O_3-B_2O_3	1	0,85	0,49
Eu	Cr	O	A_2O_3-B_2O_3	1	0,83	0,49
Gd	Cr	O	A_2O_3-B_2O_3	1	0,83	0,49
Lu	Fe	O	A_2O_3-B_2O_3	1	0,83	0,44
Nd	Cr	O	A_2O_3-B_2O_3	1	0,84	0,49
Sm	V	O	A_2O_3-B_2O_3	1	0,83	0,51
Bi	Al	O	A_2O_3-B_2O_3	1	0,9	0,43
Dy	Cr	O	A_2O_3-B_2O_3	1	0,82	0,49
Er	Cr	O	A_2O_3-B_2O_3	1	0,81	0,49
Yb	Cr	O	A_2O_3-B_2O_3	1	0,8	0,49
Ho	Cr	O	A_2O_3-B_2O_3	1	0,81	0,49
Pr	Al	O	A_2O_3-B_2O_3	1	0,88	0,43
Ho	Cr	O	A_2O_3-B_2O_3	1	0,81	0,49
Tm	Al	O	A_2O_3-B_2O_3	1	0,84	0,43
La	Y	O	A_2O_3-B_2O_3	1	0,75	0,71
Tm	Cr	O	A_2O_3-B_2O_3	1	0,8	0,49
Lu	Cr	O	A_2O_3-B_2O_3	1	0,8	0,49

Gd	Al	O	A_2O_3-B_2O_3	1	0,86	0,43
Sm	Al	O	A_2O_3-B_2O_3	1	0,87	0,43
La	Ga	O	A_2O_3-B_2O_3	1	0,86	0,49
Eu	Al	O	A_2O_3-B_2O_3	1	0,87	0,43
Er	Al	O	A_2O_3-B_2O_3	1	0,84	0,43
Y	Al	O	A_2O_3-B_2O_3	1	0,85	0,43
Dy	Al	O	A_2O_3-B_2O_3	1	0,85	0,43
Nd	Ga	O	A_2O_3-B_2O_3	1	0,84	0,49
Gd	Ga	O	A_2O_3-B_2O_3	1	0,83	0,49
Eu	Ga	O	A_2O_3-B_2O_3	1	0,83	0,49
Ho	Al	O	A_2O_3-B_2O_3	1	0,84	0,43

Table A2.1. Dataset of ABO_3 compounds

A	**B**	**X**	**GROUP**	**PEROVSKITE**	**t**	**m**
Li	Mg	F	ABX_3	0	0,849	0,541
Li	Zn	F	ABX_3	0	0,84	0,556
Li	Mn	F	ABX_3	0	0,805	0,624
Li	Ca	F	ABX_3	0	0,747	0,752
Li	Pb	F	ABX_3	0	0,69	0,895
Na	Ni	F	ABX_3	1	0,952	0,519
Na	Mg	F	ABX_3	1	0,938	0,541
Na	Cu	F	ABX_3	1	0,934	0,549
Na	Zn	F	ABX_3	1	0,929	0,556
Na	Co	F	ABX_3	1	0,927	0,56
Na	Fe	F	ABX_3	1	0,912	0,586
Na	V	F	ABX_3	1	0,907	0,594
Na	Cr	F	ABX_3	1	0,903	0,602
Na	Mn	F	ABX_3	1	0,89	0,624
Na	Cd	F	ABX_3	0	0,844	0,714
Na	Ca	F	ABX_3	0	0,825	0,752
Na	Pb	F	ABX_3	0	0,763	0,895
Na	Ba	F	ABX_3	0	0,718	1,01
Ag	Co	F	ABX_3	1	1,007	0,489
Ag	Ni	F	ABX_3	1	0,987	0,519
Ag	Mg	F	ABX_3	1	0,973	0,541
Ag	Zn	F	ABX_3	1	0,963	0,556
Ag	Mn	F	ABX_3	1	0,923	0,624
Ag	Pb	F	ABX_3	0	0,791	0,895

K	Co	F	ABX_3	1	1,061	0,489
K	Ni	F	ABX_3	1	1,04	0,519
K	Mg	F	ABX_3	1	1,024	0,541
K	Cu	F	ABX_3	1	1,019	0,549
K	Zn	F	ABX_3	1	1,015	0,556
K	Fe	F	ABX_3	1	0,995	0,586
K	V	F	ABX_3	1	0,991	0,594
K	Cr	F	ABX_3	1	0,986	0,602
K	Mn	F	ABX_3	1	0,972	0,624
K	Cd	F	ABX_3	1	0,921	0,714
K	Ca	F	ABX_3	1	0,901	0,752
K	Hg	F	ABX_3	1	0,894	0,767
K	Ba	F	ABX_3	0	0,784	1,015
Tl	Co	F	ABX_3	1	1,082	0,489
Tl	Cu	F	ABX_3	1	1,04	0,549
Tl	Fe	F	ABX_3	1	1,015	0,586
Tl	Cr	F	ABX_3	1	1,006	0,602
Tl	Mn	F	ABX_3	1	0,992	0,624
Tl	Cd	F	ABX_3	1	0,94	0,714
Rb	Be	F	ABX_3	0	1,212	0,338
Rb	Co	F	ABX_3	1	1,089	0,489
Rb	Cu	F	ABX_3	1	1,047	0,549
Ag	Cu	F	ABX_3	1	1,047	0,549
Rb	Zn	F	ABX_3	1	1,042	0,556
Rb	Fe	F	ABX_3	1	1,022	0,586
Rb	V	F	ABX_3	1	1,017	0,594
Rb	Cr	F	ABX_3	1	1,013	0,602
Rb	Mn	F	ABX_3	1	0,998	0,624
Rb	Cd	F	ABX_3	1	0,946	0,714
Rb	Ca	F	ABX_3	1	0,926	0,752
Rb	Hg	F	ABX_3	1	0,918	0,767
Rb	Sr	F	ABX_3	0	0,859	0,887
Rb	Pb	F	ABX_3	1	0,856	0,895
Cs	Be	F	ABX_3	1	1,275	0,338
Cs	Mg	F	ABX_3	1	1,107	0,541
Cs	Mn	F	ABX_3	0	1,051	0,624
Cs	Cd	F	ABX_3	1	0,996	0,714
Cs	Ca	F	ABX_3	1	0,974	0,752
Cs	Hg	F	ABX_3	1	0,966	0,767
Cs	Sr	F	ABX_3	1	0,904	0,887

Cs	Pb	F	ABX_3	1	0,901	0,895
Cs	Ba	F	ABX_3	0	0,847	1,015
Li	Be	Cl	ABX_3	0	0,92	0,249
Li	Ni	Cl	ABX_3	0	0,832	0,381
Li	Mg	Cl	ABX_3	0	0,822	0,398
Cu	Zn	Cl	ABX_3	0	0,815	0,409
Li	V	Cl	ABX_3	0	0,8	0,436
Li	Cr	Cl	ABX_3	0	0,797	0,442
Cu	Cd	Cl	ABX_3	0	0,753	0,525
Cu	Ca	Cl	ABX_3	0	0,74	0,552
Li	Ca	Cl	ABX_3	0	0,74	0,552
Li	Pb	Cl	ABX_3	0	0,693	0,657
Li	Ba	Cl	ABX_3	0	0,658	0,746
Na	Be	Cl	ABX_3	0	1,001	0,249
Na	Ni	Cl	ABX_3	0	0,905	0,381
Na	Zr	Cl	ABX_3	0	0,894	0,398
Na	Zn	Cl	ABX_3	0	0,887	0,409
Na	Cr	Cl	ABX_3	0	0,867	0,442
Na	Mn	Cl	ABX_3	0	0,857	0,459
Na	Cd	Cl	ABX_3	0	0,82	0,525
Na	Ca	Cl	ABX_3	0	0,805	0,552
Na	Sn	Cl	ABX_3	0	0,778	0,608
Na	Sr	Cl	ABX_3	0	0,757	0,652
Na	Pb	Cl	ABX_3	0	0,754	0,657
Na	Ba	Cl	ABX_3	0	0,716	0,746
Ag	Mg	Cl	ABX_3	0	0,922	0,398
Ag	Ca	Cl	ABX_3	0	0,83	0,552
Ag	Sn	Cl	ABX_3	0	0,802	0,608
K	Be	Cl	ABX_3	0	1,079	0,249
K	Ni	Cl	ABX_3	0	0,976	0,381
K	Zr	Cl	ABX_3	0	0,964	0,398
K	Mg	Cl	ABX_3	0	0,964	0,398
K	Fe	Cl	ABX_3	1	0,942	0,431
K	Mn	Cl	ABX_3	1	0,924	0,459
K	Cd	Cl	ABX_3	1	0,884	0,525
K	Ca	Cl	ABX_3	1	0,868	0,552
K	Sr	Cl	ABX_3	0	0,816	0,652
K	Sm	Cl	ABX_3	0	0,805	0,674
K	Ba	Cl	ABX_3	0	0,772	0,746
Tl	Be	Cl	ABX_3	0	1,098	0,249

Tl	Mg	Cl	ABX_3	0	0,981	0,398
Tl	Zn	Cl	ABX_3	0	0,973	0,409
Tl	Mn	Cl	ABX_3	1	0,94	0,459
Tl	Cd	Cl	ABX_3	1	0,899	0,525
Tl	Eu	Cl	ABX_3	0	0,833	0,646
Tl	Sr	Cl	ABX_3	0	0,83	0,652
Tl	Pb	Cl	ABX_3	0	0,827	0,657
Rb	Be	Cl	ABX_3	0	1,104	0,249
Rb	Mg	Cl	ABX_3	0	0,987	0,398
Rb	Zn	Cl	ABX_3	0	0,979	0,409
Rb	Co	Cl	ABX_3	0	0,977	0,412
Rb	Fe	Cl	ABX_3	0	0,964	0,431
Rb	Cr	Cl	ABX_3	1	0,956	0,442
Rb	Mn	Cl	ABX_3	1	0,945	0,459
Rb	Cd	Cl	ABX_3	1	0,904	0,525
Rb	Ca	Cl	ABX_3	1	0,888	0,552
Rb	Eu	Cl	ABX_3	0	0,838	0,646
Rb	Sr	Cl	ABX_3	0	0,835	0,652
Cs	Ni	Cl	ABX_3	0	1,044	0,381
Cs	Mg	Cl	ABX_3	0	1,031	0,398
Cs	Ge	Cl	ABX_3	0	1,027	0,403
Cs	Zn	Cl	ABX_3	0	1,023	0,409
Cs	Co	Cl	ABX_3	0	1,021	0,412
Cs	Fe	Cl	ABX_3	0	1,007	0,431
Cs	V	Cl	ABX_3	0	1,004	0,436
Cs	Cr	Cl	ABX_3	0	1	0,442
Cs	Mn	Cl	ABX_3	1	0,988	0,459
Cs	Cd	Cl	ABX_3	1	0,945	0,525
Cs	Ca	Cl	ABX_3	1	0,929	0,552
Cs	Hg	Cl	ABX_3	1	0,922	0,564
Cs	Sn	Cl	ABX_3	1	0,897	0,608
Cs	Eu	Cl	ABX_3	1	0,876	0,646
Cs	Sr	Cl	ABX_3	1	0,873	0,652
Cs	Pb	Cl	ABX_3	1	0,87	0,657
Cs	Ba	Cl	ABX_3	0	0,826	0,746
Li	Mg	Br	ABX_3	0	0,815	0,367
Li	Co	Br	ABX_3	0	0,808	0,38
Li	Ca	Br	ABX_3	0	0,738	0,51
Li	Sr	Br	ABX_3	0	0,696	0,602
Li	Pb	Br	ABX_3	0	0,694	0,607

Li	Ba	Br	ABX_3	0	0,66	0,689
Na	Mg	Br	ABX_3	0	0,884	0,367
Na	Cd	Br	ABX_3	0	0,814	0,485
Na	Ca	Br	ABX_3	0	0,8	0,51
Na	Sr	Br	ABX_3	0	0,754	0,602
Na	Ba	Br	ABX_3	0	0,716	0,689
Ag	Cd	Br	ABX_3	0	0,838	0,485
Ag	Pb	Br	ABX_3	0	0,774	0,607
K	Co	Br	ABX_3	0	0,941	0,38
K	Ba	Br	ABX_3	0	0,769	0,689
Rb	Ni	Br	ABX_3	0	0,982	0,352
Rb	Mn	Br	ABX_3	0	0,933	0,423
Rb	Cd	Br	ABX_3	1	0,894	0,485
Rb	Ba	Br	ABX_3	0	0,786	0,689
Cs	Ni	Br	ABX_3	0	1,025	0,352
Cs	Mn	Br	ABX_3	0	0,973	0,423
Cs	Ti	Br	ABX_3	0	0,963	0,439
Cs	Cd	Br	ABX_3	1	0,933	0,485
Cs	Hg	Br	ABX_3	1	0,911	0,52
Cs	Sn	Br	ABX_3	1	0,887	0,561
Cs	Pb	Br	ABX_3	1	0,862	0,607
Cs	Ba	Br	ABX_3	0	0,82	0,689
Cu	Cd	I	ABX_3	0	0,741	0,432
Li	Mg	I	ABX_3	0	0,806	0,327
Li	Mn	I	ABX_3	0	0,777	0,377
Na	Mg	I	ABX_3	0	0,869	0,327
Na	Cd	I	ABX_3	0	0,806	0,432
Na	Ca	I	ABX_3	0	0,793	0,455
Na	Hg	I	ABX_3	0	0,788	0,464
K	Mg	I	ABX_3	0	0,93	0,327
K	Co	I	ABX_3	0	0,922	0,339
K	Mn	I	ABX_3	0	0,896	0,377
K	Cd	I	ABX_3	0	0,862	0,432
K	Hg	I	ABX_3	0	0,843	0,464
Tl	Mn	I	ABX_3	1	0,91	0,377
Tl	Pb	I	ABX_3	1	0,813	0,541
Rb	Mg	I	ABX_3	0	0,949	0,327
Rb	Mn	I	ABX_3	0	0,915	0,377
Rb	Sn	I	ABX_3	1	0,84	0,5
Cs	Mg	I	ABX_3	0	0,988	0,327

Cs	Mn	I	ABX_3	0	0,952	0,377
Cs	Sn	I	ABX_3	1	0,874	0,5

Table A2.2. Dataset of ABX_3 compounds

Compound	n	n ri	n ri xsi	n ri rc	n ri xsi rc	n q ri xsi rc
Training subset						
$AgBiO_3$	x					
$CsVO_3$	x					
$PbSiO_3$	x					
$SrGeO_3$	x					
$CdGeO_3$	x	x				
$SmYO_3$	x	x	x	x	x	x
$BiSmO_3$	x					
$EuSiO_3$	x					
$RbTaO_3$	x					x
$CaVO_3$	x					
$SnPbO_3$	x					
$InFeO_3$	x					
$NaVO_3$	x			x		
$TlSbO_3$	x					
$GdYO_3$	x		x			x
$BaMnO_3$	x					
$BaSiO_3$	x					
$YAlO_3$	x					
$BaGeO_3$	x					
$NaBiO_3$	x	x	x	x		
$CsNbO_3$	x					
$PbGeO_3$	x					
$BaMoO_3$			x			
$AgSbO_3$						x
Test subset						
$CaTiO_3$	x					
$NaNbO_3$	x					
$SmSiO_3$	x					
$CaMnO_3$	x					
$InCrO_3$	x					
$RbNbO_3$	x					
$KSbO_3$	x					

$SrMnO_3$	x		x	x	x	x
$NaSbO_3$		x				
$AgTaO_3$			x			

Table A2.3. Mistakes of models for ABO3 dataset

Compounds	n	n ri	n ri xsi	n ri rc	n ri xsi rc	n q ri xsi rc
Training subset						
$RbEuCl_3$	x					
$RbSnI_3$	x	x				
$TlMnI_3$	x	x		x		x
$TlSrCl_3$	x					
$NaCaF_3$	x					
$CsCaCl_3$	x	x				x
$RbSrF_3$	x	x		x		
$RbCrCl_3$	x	x	x	x	x	x
$CsCdBr_3$	x					
$RbMnCl_3$	x	x	x	x		x
$CsMnF_3$	x	x	x	x	x	x
$CsBaCl_3$	x					
$TlEuCl_3$	x					
$TlMnCl_3$	x	x				
$AgSnCl_3$	x					
$KCdCl_3$	x	x				
$CsSnI_3$	x	x				
$CsBaF_3$	x	x				
$KCaCl_3$	x	x	x	x	x	x
$RbCdCl_3$	x					
$CsSnBr_3$	x					
$RbCdBr_3$	x	x				
$AgPbF_3$	x					
$KHgF_3$		x			x	
$CsPbCl_3$		x				
$CsBeF_3$		x	x	x	x	x
$AgMgF_3$		x				
$CsGeCl_3$				x		
$RbZnCl_3$					x	
$TlPbI_3$					x	
Test subset						
$KBaF_3$	x					

$TlPbCl_3$	x					
$RbCaCl_3$	x	x				
$KFeCl_3$	x	x	x	x	x	x
$RbBeF_3$	x					x
$KMnCl_3$	x	x	x	x		
$CsMnCl_3$	x	x	x	x	x	x
$NaMgF_3$		x				
$TlZnCl_3$			x	x	x	x
$TlMgCl_3$					x	

Table A2.4. Mistakes of models for ABh3 dataset

Compound	n	n ri	n ri xsi	n ri rc	n ri xsi rc	n q ri xsi rc
Training subset						
$AgBiO_3$	x	x				x
$CsVO_3$	x					
$PbSiO_3$	x					
$SrGeO_3$	x					
$CdGeO_3$	x					
$SmYO_3$	x					
$BiSmO_3$	x					
$BiAlO_3$	x					
$SrSiO_3$	x					
$EuSiO_3$	x					
$RbTaO_3$	x	x	x	x	x	
$KAsO_3$	x					
$NaAsO_3$	x					
$ScCrO_3$	x					
$SnPbO_3$	x					
$InFeO_3$	x	x				
KVO_3	x					
$TlSbO_3$	x					
$GdYO_3$	x					
$BaMnO_3$	x					
$BaSiO_3$	x					
$MgGeO_3$	x					
$BaGeO_3$	x					
$NaBiO_3$	x	x	x	x	x	
$CsNbO_3$	x					

$PbGeO_3$	x					
$RbEuCl_3$	x					
$TlSrCl_3$	x					
$NaCaF_3$	x					
$CsCaCl_3$	x					
$KNiCl_3$	x					
$RbSrF_3$	x					
$RbCrCl_3$	x	x	x	x	x	x
$KMgF_3$	x					
$RbMnCl_3$	x	x	x	x	x	x
$CsMnF_3$	x	x	x			x
$CsSrCl_3$	x					
$CsBaCl_3$	x					
$TlEuCl_3$	x					
$KCdCl_3$	x					
$CsBeF_3$	x	x	x	x	x	x
$CsBaF_3$	x					
$NaPbF_3$	x					
$RbCdCl_3$	x					
$RbCdBr_3$	x					
$AgPbF_3$	x					
$NaVO_3$		x				x
$YTiO_3$		x				
$TlMnI_3$		x		x		x
$TlMnCl_3$		x		x		x
$PbLaO_3$			x	x		
$BaMoO_3$			x			
$KCaCl_3$			x			
$CaUO_3$				x		
$BaAlO_3$				x		
$BaTiO_3$						x
$CsIO_3$						x
Test subset						
$NaNbO_3$	x					
$SmSiO_3$	x					
$InCrO_3$	x					
$RbNbO_3$	x			x	x	
$KSbO_3$	x					
$MgTiO_3$	x					
$SrMnO_3$	x		x	x	x	x

$KBaF_3$	x					
$TlPbCl_3$	x					
$AgPbBr_3$	x					
$CsBaBr_3$	x					
$TlZnCl_3$	x		x			
$RbCaCl_3$	x					
$NaMgF_3$	x					
$CsMnCl_3$	x	x	x	x	x	x
$CaMnO_3$		x				
$KFeCl_3$		x	x	x	x	x
$CsTiBr_3$		x				
$KMnCl_3$		x	x	x	x	x
$AgTaO_3$			x			
$TlMgCl_3$			x		x	
$NaCdF_3$					x	x

Table A2.5. Mistakes of models for ABh_3+ABO_3 merged dataset

MODEL FAMILY	**COMPOUND**	**PREDICTION**	**ICSD**	**Google Scholar**	**Refernce**
abx	$RbSnI_3$	0	0	1	[310]
abx/abx+abo	$TlMnI_3$	0	0	contradiction	[106]
abx	$CsCaCl_3$	0	not found	1	[311]
abx	$RbSrF_3$	1	not found	1	[312]
abx/abx+abo	$RbCrCl_3$	0	1		
abx/abx+abo	$RbMnCl_3$	0	0	1	[106,313]
abx/abx+abo	$CsMnF_3$	1	0	perovskite report not found	
abx/abx+abo	$TlMnCl_3$	0	1		
abx	$KCdCl_3$	0	0	unstable	[314]
abx	$CsSnI_3$	0	1		
abx	$CsBaF_3$	1	not found	1	[315]
abx/abx+abo	$KCaCl_3$	0	not found	1	[316]
abx	$RbCdBr_3$	0	0	1	[317]
abx	$KHgF_3$	0	1		
abx	$CsPbCl_3$	0	1		
abx/abx+abo	$CsBeF_3$	0	0	1	[106]
abx	$AgMgF_3$	0	not found	1	[106,318]
abx	$CsGeCl_3$	1	1		
abx	$RbZnCl_3$	1	not found	unstable	[319]
abx	$TlPbI_3$	0	0	1	[320]

abx	$RbCaCl_3$	0	not found	1	[316]
abx/abx+abo	$KFeCl_3$	0	0	contradiction	[321]
abx/abx+abo	$KMnCl_3$	0	1		
abx/abx+abo	$CsMnCl_3$	0	0	1	[106,322]
abx	$NaMgF_3$	0	1		
abx	$TlZnCl_3$	1	not found	structure report not found	
abx/abx+abo	$TlMgCl_3$	1	not found	1	[323]
abo	$CdGeO_3$	1	1		
abo	$SmYO_3$	1	0	perovskite report not found	
abo/abx+abo	$RbTaO_3$	1	0	1	[324,325]
abo/abx+abo	$NaVO_3$	0	0	1	[326]
abo	$GdYO_3$	1	0	perovskite report not found	
abo/abx+abo	$NaBiO_3$	1	0	perovskite report not found	
abo	$BaMoO_3$	0	1		
abo	$AgSbO_3$	0	0	contradiction	[327]
abo	$SrMnO_3$	1	1		
abo	$NaSbO_3$	1	1		
abo/abx+abo	$AgTaO_3$	0	1		
abx+abo	$AgBiO_3$	1	0	1	[328]
abx+abo	$InFeO_3$	1	0	1	[329]
abx+abo	$YTiO_3$	0	1		
abx+abo	$PbCeO_3$	0	not found	structure report not found	
abx+abo	$BaMoO_3$	0	1		
abx+abo	$CaUO_3$	0	0	1	[330]
abx+abo	$LaAlO_3$	0	1		
abx+abo	$BaTiO_3$	0	1		
abx+abo	$CsIO_3$	0	1		
abx+abo	$CaMnO_3$	0	1		
abx+abo	$CsTiBr_3$	1	0	perovskite report not found	
abx+abo	$NaCdF_3$	1	not found	1	[113]

Table A2.6. Mistake analysis

Appendix C

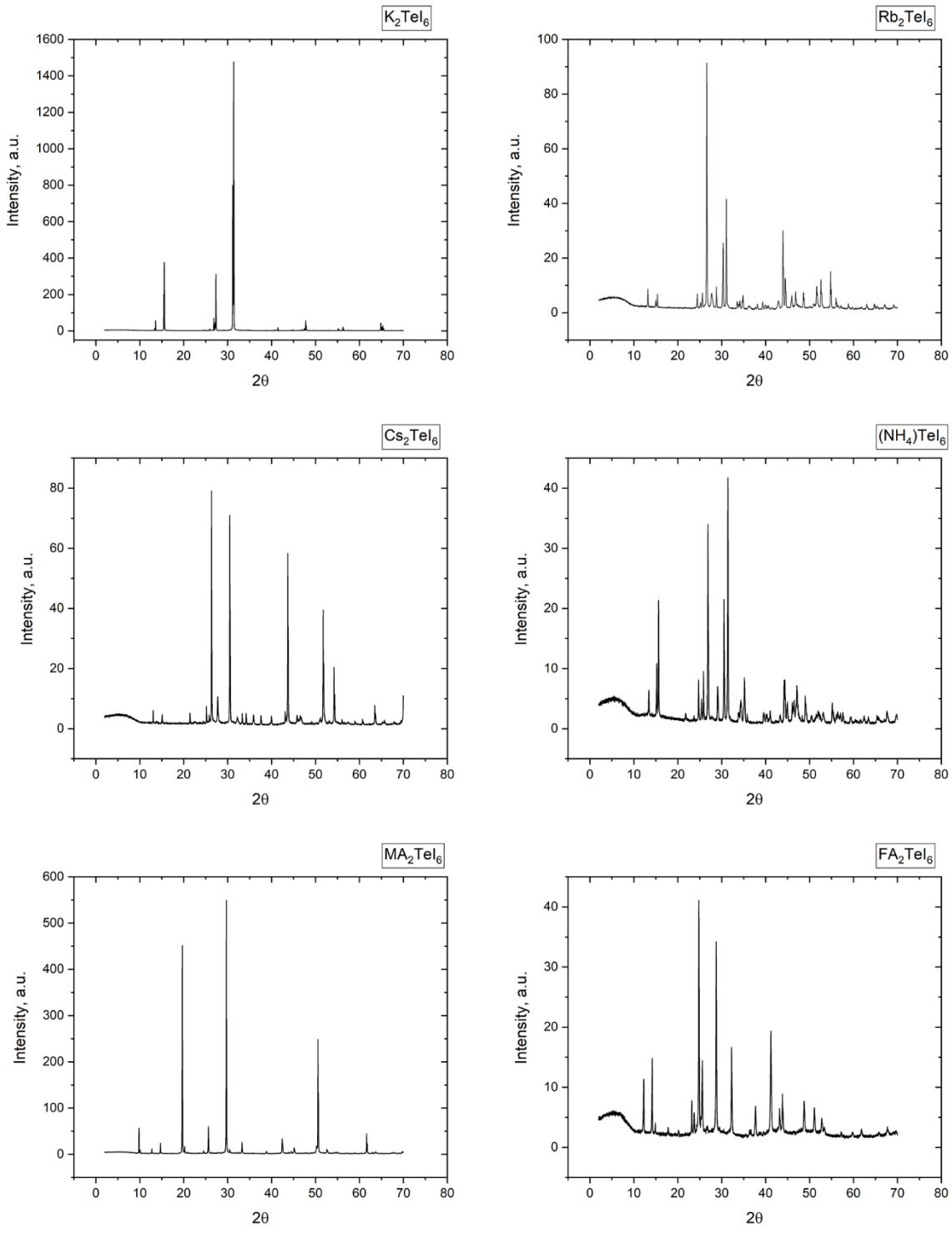

Figure A3.1 A_2TeI_6 powder XRD patterns

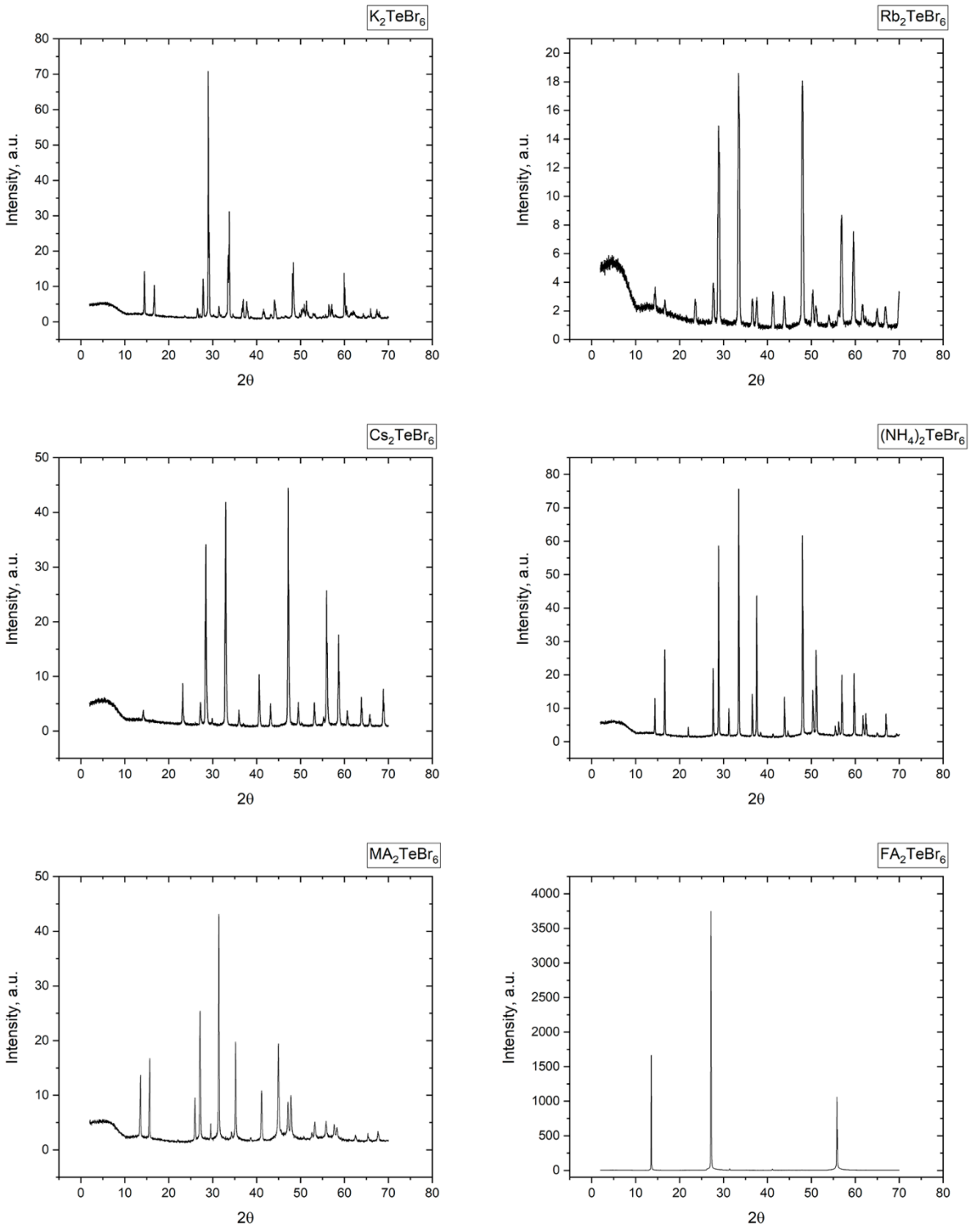

Figure A3.2 A_2TeBr_6 powder XRD patterns

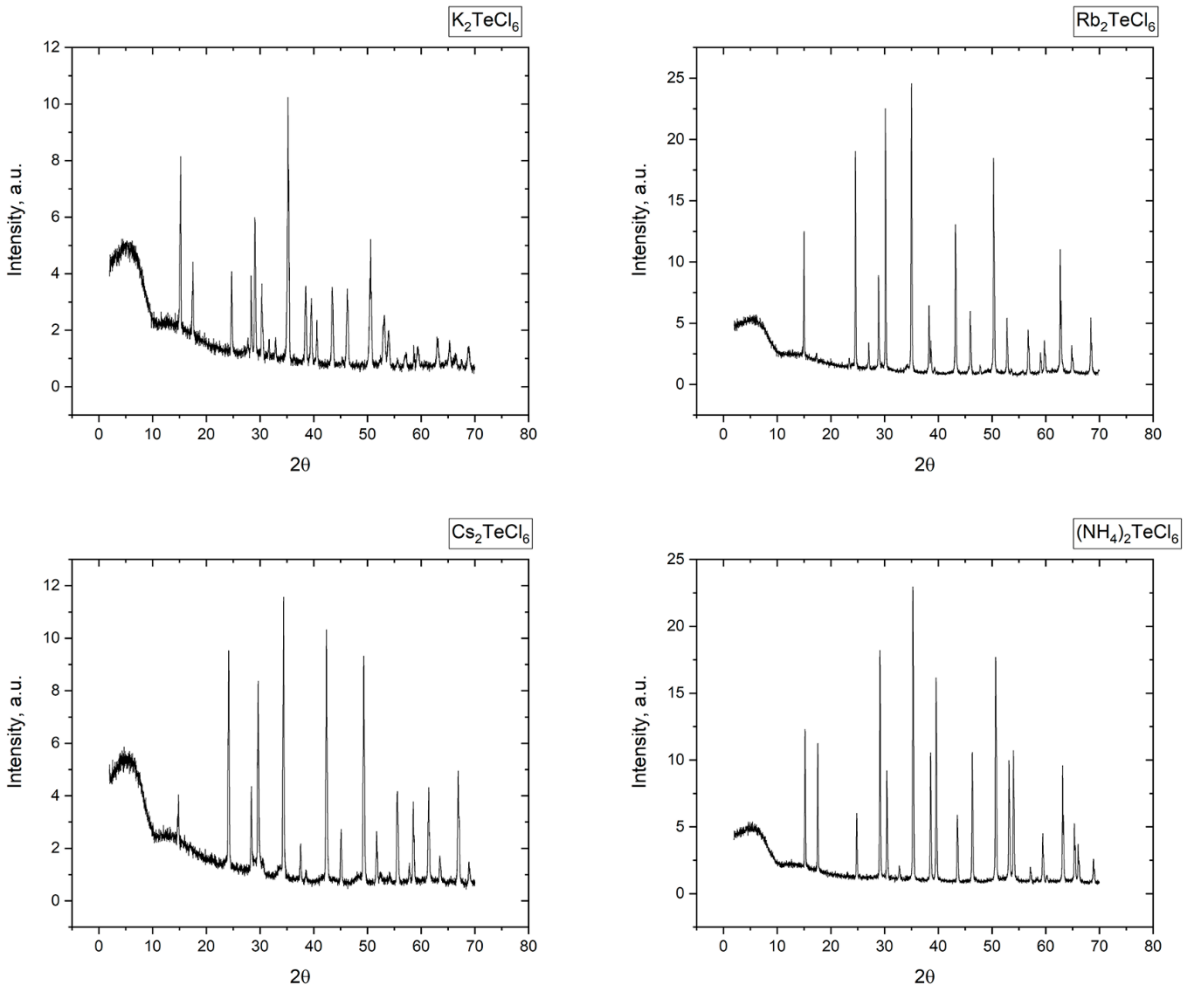

Figure A3.3 A_2TeCl_6 powder XRD patterns

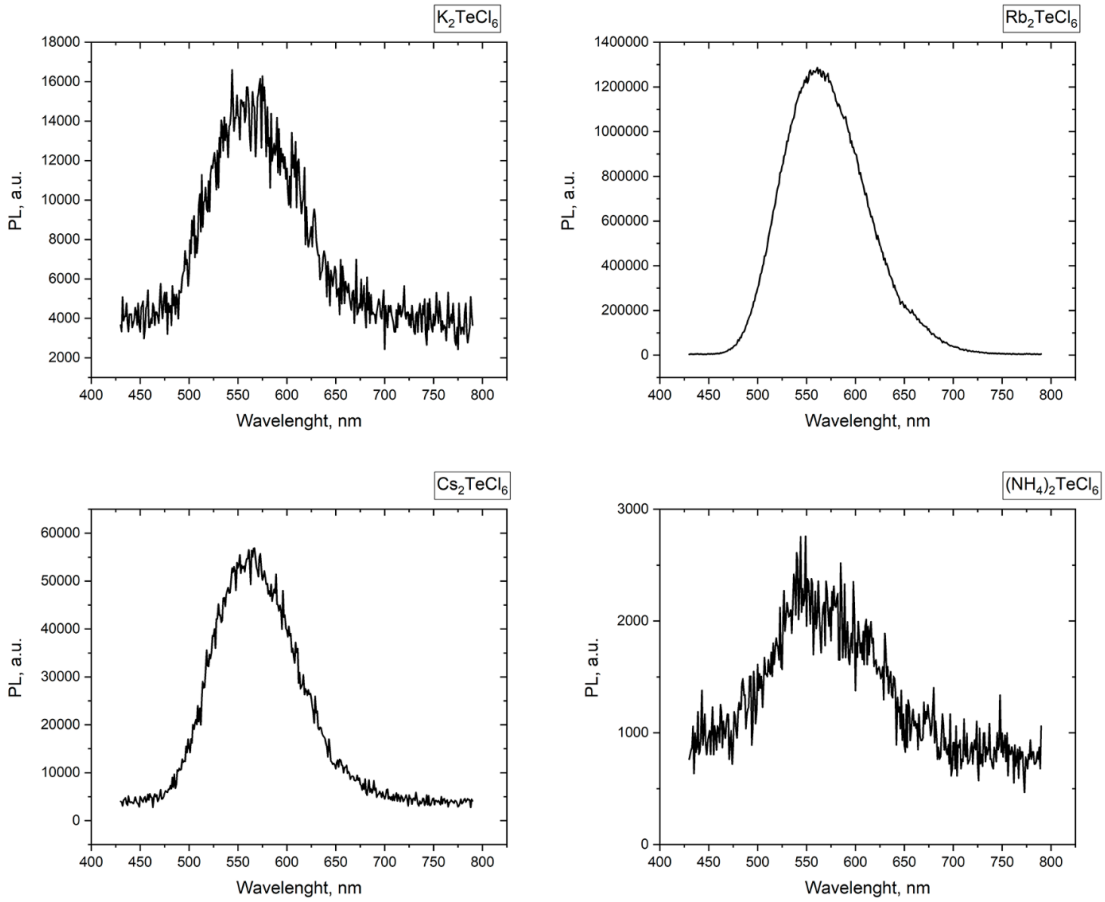

Figure A3.4. A_2TeCl_6 photoluminicece spectra.

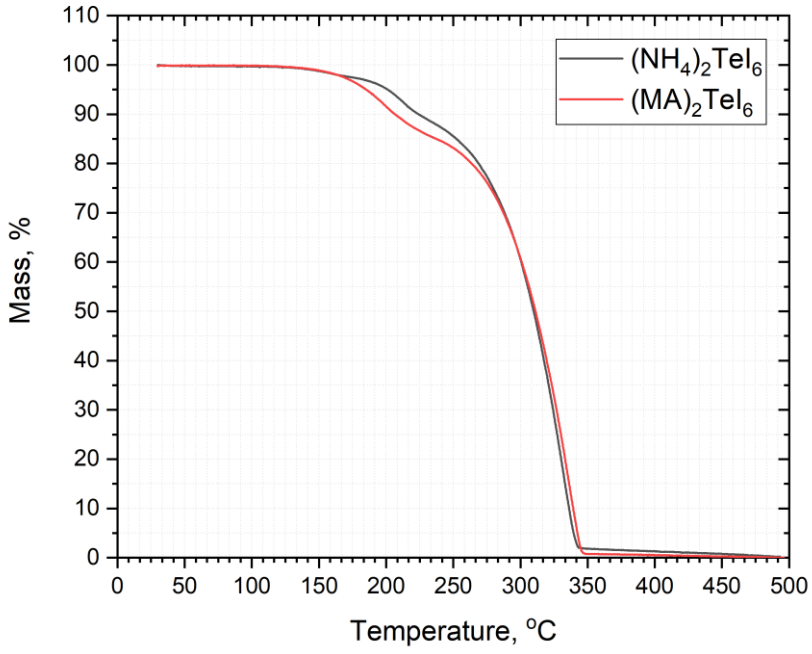

Figure A3.5 Thermogravimetric analysis of the synthesized powders

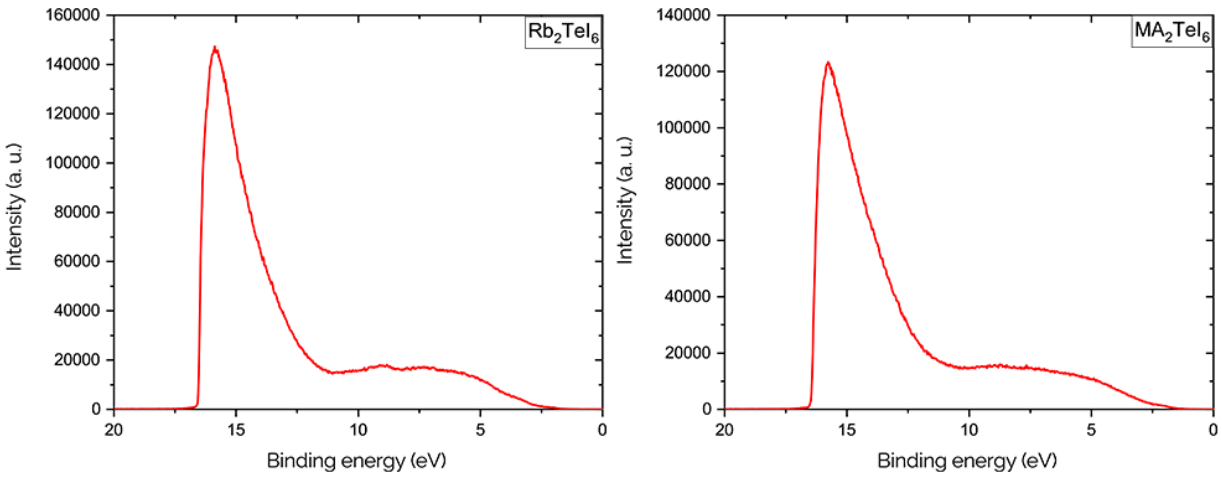

Figure A3.6 Ultraviolet photoelectron spectroscopy of the thin films

Compound	MA_2TeI_6	FA_2TeI_6	MA_2TeBr_6
Formula	$C_2H_6I_6N_2Te$	$C_2H_{10}I_6N_4Te$	$C_2H_{10}Br_6N_4Te$
Crystal system	Cubic	Cubic	Cubic
Space group	F*m*-3*m*	F*m*-3*m*	F*m*-3*m*
Temperature / K	294(2)	297(2)	294(2)
Lattice constants / Å and °	*a* = 12.0493(13)	*a* = 12.364(5)	*a* = 11.442(2)
Volume / Å^3	1749.4(6)	1890(2)	1497.8(8)
Z	4	4	4
$D_{calculated}$ / g·cm^{-3}	3.62	3.44	4.13
Radiation	Mo-K_α (λ = 0.71069 Å)	Mo-K_α (λ = 0.71069 Å)	Mo-K_α (λ = 0.71069 Å)
Crystal habit	Black block	Black block	Red block
Θ range / °	2.93 – 26.19	2.85 – 26.2	3.08 – 26.33
Min. / max. *h k l*	–14 ≤ *h* ≤ 14 –14 ≤ *k* ≤ 14 –14 ≤ *l* ≤ 14	–14 ≤ *h* ≤ 15 –15 ≤ *k* ≤ 13 –15 ≤ *l* ≤ 9	–11 ≤ *h* ≤ 14 –7 ≤ *k* ≤ 14 –13 ≤ *l* ≤ 13
Reflections, measured / independent	1274 / 122	2380 /	578 / 104
Refined parameters / restraints	14 / 1	14 / 3	15 / 3
R1 [I > 2σ(I)]	0.0205	0.035	0.1227
R_{sym}	0.028	0.0958	0.0753
Max. / min. Residual Density / e$^-$/Å^3	0.33 and -0.365	0.861 and -0.522	2.551 and -1.786

Table A3.1 Crystallographic parameters and refinement statistics from single-crystal diffraction experiments.

eV	K_2TeBr_6	Rb_2TeBr_6	Cs_2TeBr_6	$(NH_4)_2TeBr$	MA_2TeBr	FA_2TeBr_6
$(\alpha_{BLB}E)^2$	2.16	2.15	2.26	2.1	2.11	2.23
$(\alpha_{simp}E)^2$	2.14	2.1	2.19	2.09	2.09	2.19
$(\alpha_{comp}E)^2$	2.16	2.19	2.28	2.14	2.15	2.18
$(\alpha_{SKM}E)^{1/2}$	2.06	2.16	2.21	2.16	2.09	2.03
E_{Boltz}^{dir}	2.18	2.19	2.23	2.14	22.16	2.22
E_{Boltz}^{indir}	1.78	1.79	1.89	1.74	1.76	1.82

Table A3.2 Summary of the band-gap calculations for A_2TeBr_6 compounds.

eV	K_2TeCl_6	Rb_2TeCl_6	Cs_2TeCl_6	$(NH_4)_2TeCl$
$(\alpha_{BLB}E)^2$	2.6	2.56	2.65	2.57
$(\alpha_{simp}E)^2$	2.55	2.49	2.58	2.49
$(\alpha_{comp}E)^2$	2.6	2.58	2.65	2.56
$(\alpha_{SKM}E)^{1/2}$	2.5	2.54	2.6	2.48
E_{Boltz}^{dir}	2.61	2.59	2.67	2.58
E_{Boltz}^{indir}	2.21	2.19	2.27	2.18

Table A3.3 Summary of the band-gap calculations for A_2TeCl_6 compounds.

Experiment derails

Materials

List of chemicals and were purchased: Hydroiodic acid (HI) 57% Pure AppliChem Panreac; Hydrobromic acid (HBr) 47% for analysis Merck KGaA; Tellurium dioxide (TeO_2) 99.999%-Te Puraterm ABCR; Hydrochloride acid (HCl) 32% tech Reactolab SA; Tellurium(IV) iodide (TeI_4) 99.9%-Te Puraterm ABCR; Tellurium(IV) bromide ($TeBr_4$) 99.9%-Te Puraterm ABCR; Potassium iodide (KI) 99%+ ReagentPlus Sigma-Aldrich; Potassium bromide (KBr) 99%+ Sigma-Aldrich; Potassium chloride (KCl) 99%+ ACS Reagent Grade Sigma-Aldrich; Rubidium iodide (RbI) 99.8%-Rb ABCR; Rubidium bromide ($RbBr$) 99.8%-Rb (metals basis) ABCR; Rubidium chloride ($RbCl$) 99.8% trace metals basis Sigma-Aldrich; Cesium iodide (CsI) 99.9% trace metals basis Sigma-Aldrich; Cesium bromide ($CsBr$) 99.999% (metals basis) ABCR; Cesium chloride ($CsCl$) 99.999% trace metals basis Sigma-Aldrich; Ammonium iodide (NH_4I) 99+%, for analysis Acros; Ammonium bromide (NH_4Br) 99.999% (metal basis) Puraterm ABCR; Ammonium chloride (NH_4Cl) 99.999% Puraterm ABCR; Methylammonium iodide (CH_3NH_3I) Dyesol; Methylammonium bromide (CH_3NH_3Br) Dyesol; Methylammonium chloride (CH_3NH_3Cl) for synthesis Merck; Formamidinium iodide ($CH(NH_2)_2I$) Dyesol; Formamidinium bromide ($CH(NH_2)_2Br$) Dyesol; Formamidine hydrochloride ($CH(NH_2)_2Cl$) Sigma-Aldrich; *Solvents:* Chlorobenzene 99.5%, Extra Dry Sigma-Aldrich; Isopropanol () 99.8%, Extra Dry ACROS Organics; N,N-Dimethylformamide 99.8%, Extra Dry ACROS Organics; Dimethyl sulfoxide 99.7% Extra Dry ACROS Organics; Acetone, 99.8%, Extra Dry ACROS Organics; Methanol 99.9% Extra Dry ACROS Organics; Acetonitrile 99.9% Extra Dry ACROS Organics; Propylene carbonate, anhydrous 99.7% Sigma-Aldrich; Ethylene carbonate, anhydrous 99% Sigma-Aldrich; Gamma-Butyrolactone anhydrous 99% Sigma-Aldrich;

All chemicals were used without extra purification.

Synthesis

All compounds were tried to synthesis in two ways.

Direct: Tellurium halide (TeX_4) was dissolved in halide acid (1mmol of TeX_4 per 2.5ml of acid) and mixed with a stoichiometric amount of AX dissolved in HX (1 mmol of AX per 1.25 ml of acid) and after drying at 95C and dry airflow overnight. All processes happened during continuous mixing (~200 rpm by magnetic stirrer).

Throw TeO_2: Tellurium oxide (TeO_2) was dissolved halide acid (1mmol of TeO_2 per 2.5ml of acid) and mixed with a stoichiometric amount of AX dissolved in HX (1 mmol of AX per 1.25 ml of acid) and after drying at 95C and dry airflow overnight. All processes happened during continuous mixing (~200 rpm by magnetic stirrer).

Single crystal diffraction experiments

Suitable single crystals were manually transferred into immersion oil and fixed on a Kapton tip. The data collection was performed at room temperature on a Bruker D8 Venture diffractometer using Mo Kα radiation. (λ=0.71069 Å) Data reduction and absorption correction were made with SAINT and SADABS integrated with the APEX 3 software package. The structure solution was carried out with SHELXS and the refinement with SHELXL-2014 in the WINGX environment. Tellurium and iodide/bromide atoms were refined anisotropically. The organic cations were found to be fully disordered in the inorganic cage and were added manually using geometrical restraints.

Powder diffraction experiments

Crystalline powders were measured using a Bruker D8 Advance diffractometer in Bragg-Brentano geometry under Cu Kα radiation. The powders were dispersed onto a low background silicon holder. Unit cell refinements were performed using Jana2006.

Sample preparation

100mg of each material in powder state were mixed with $100\mu l$ of the corresponding hydrohalic acid to get a wet gel-like substance. These substances were deposited on microscope glass slides and dried under a vacuum. XRD patterns of the samples have no difference with powders.

UV-Vis-NIR spectrometry

Steady-state absorption and diffuse-reflection spectra were acquired with a Perkins Elmer lambda 950s UV/Vis spectrophotometer using an integrating sphere for accounting for optical losses outside of the active layer.

PL measurements

Steady-state and time-resolved photoluminescence measurements were carried out on Horiba a Fluorolog-3, with a PMT as the detector.

Thermogravimetric analysis

The experiments were done by Perkins Elmer TGA 8000 Thermogravimetric analyzer. Powders have been placed in aluminum crucibles and heated up to $450°C$ with a rate $10°C/min$ in N_2 atmosphere.

Radiofrequency Magnetron Sputtering

Thin films have been deposited on amorphous silica substrates (MaTek, roughness ca. 1 nm), Si interdigitated with gold substrates, FTO substrates, and MoO_3 substrates by means of radiofrequency (RF) magnetron sputtering starting from a stoichiometric mixture of the respective halide precursors: CsI/TeI_4 (Aldrich, > 99.9%) for Cs_2TeI_6, RbI/TeI_4 (Aldrich, > 99.9%) for Rb_2TeI_6, and MAI/TeI_4 (Aldrich, > 99.9%) for MA_2TeI_6 (MA = methylammonium iodide).

FTO and MoO_3 substrates have been pre-cleaned just before deposition by a vacuum treatment at 200°C for 15 minutes.

The targets (diameter 5.08 cm, thickness 1 cm) were made of pressed powders of the mixtures mentioned above. Deposition parameters were: (i) target-to-substrate distance, 10 cm, (ii) RF-power, 50 W (iii) argon pressure, $2 \cdot 10^{-2}$ mbar (iv) argon flux 20 SCCM. The depositions have been carried out in power-control mode. Film thickness has been determined by means of a P-6 stylus profilometer KLA Tencor.

References

1 V. Smil, *Energy and Civilization: A History*, MIT Press, Cambridge, MA, USA, 2017.
2 R. H. Gray, *AJ*, 2020, **159**, 228.
3 Data tables – Data & Statistics, https://www.iea.org/data-and-statistics/data-tables, (accessed August 12, 2021).
4 Global energy demand and CO2 emissions trends in the Stated Policies Scenario, 2019-2030 – Charts – Data & Statistics, https://www.iea.org/data-and-statistics/charts/global-energy-demand-and-co2-emissions-trends-in-the-stated-policies-scenario-2019-2030, (accessed August 12, 2021).
5 World Energy Outlook 2020 – Analysis, https://www.iea.org/reports/world-energy-outlook-2020, (accessed August 12, 2021).
6 Global Warming of 1.5 °C —, https://www.ipcc.ch/sr15/, (accessed August 12, 2021).
7 Global warming will happen faster than we think, https://www.nature.com/articles/d41586-018-07586-5, (accessed August 12, 2021).
8 R. Perez and M. Perez, .
9 E. G. Carayannis, J. Draper and I. A. Iftimie, *IEEE Transactions on Engineering Management*, 2020, 1–15.
10 C. Wu, T. W. Kim, T. Guo and F. Li, *Nano Energy*, 2017, **32**, 367–373.
11 A. Cabrera-Tobar, E. Bullich-Massagué, M. Aragüés-Peñalba and O. Gomis-Bellmunt, *Renewable and Sustainable Energy Reviews*, 2016, **59**, 309–319.
12 D. Murphy and C. Hall, *Annals of the New York Academy of Sciences*, 2010, **1185**, 102–18.
13 J. R. Bolton and D. O. Hall, *Photochemistry and Photobiology*, 1991, **53**, 545–548.
14 R. L. House, N. Y. M. Iha, R. L. Coppo, L. Alibabaei, B. D. Sherman, P. Kang, M. K. Brennaman, P. G. Hoertz and T. J. Meyer, *Journal of Photochemistry and Photobiology C: Photochemistry Reviews*, 2015, **25**, 32–45.
15 S. E. Hosseini and M. A. Wahid, *International Journal of Energy Research*, 2020, **44**, 4110–4131.
16 I. Dincer and C. Acar, *International Journal of Hydrogen Energy*, 2015, **40**, 11094–11111.
17 H. L. Zhang, J. Baeyens, J. Degrève and G. Cacères, *Renewable and Sustainable Energy Reviews*, 2013, **22**, 466–481.
18 A. Peinado Gonzalo, A. Pliego Marugán and F. P. García Márquez, *Applied Energy*, 2019, **255**, 113893.
19 G. L. Araújo and A. Martí, *Solar Energy Materials and Solar Cells*, 1994, **33**, 213–240.
20 A. D. Vos, *J. Phys. D: Appl. Phys.*, 1980, **13**, 839–846.
21 A. De Vos and H. Pauwels, *Appl. Phys.*, 1981, **25**, 119–125.
22 W. Shockley and H. J. Queisser, *Journal of Applied Physics*, 1961, **32**, 510–519.
23 Best Research-Cell Efficiency Chart, https://www.nrel.gov/pv/cell-efficiency.html, (accessed August 12, 2021).
24 S. Rühle, *Solar Energy*, 2016, **130**, 139–147.
25 A. Kojima, K. Teshima, Y. Shirai and T. Miyasaka, *J. Am. Chem. Soc.*, 2009, **131**, 6050–6051.
26 M. Yuan, L. N. Quan, R. Comin, G. Walters, R. Sabatini, O. Voznyy, S. Hoogland, Y. Zhao, E. M. Beauregard, P. Kanjanaboos, Z. Lu, D. H. Kim and E. H. Sargent, *Nature Nanotech*, 2016, **11**, 872–877.
27 N.-G. Park, *Materials Today*, 2015, **18**, 65–72.
28 F. F. Y. Wang and K. P. Gupta, *Metall Mater Trans B*, 1973, **4**, 2767–2779.
29 J. A. Steele, M. Lai, Y. Zhang, Z. Lin, J. Hofkens, M. B. J. Roeffaers and P. Yang, *Acc. Mater. Res.*, 2020, **1**, 3–15.
30 A. S. Bhalla, R. Guo and R. Roy, *Materials Research Innovations*, 2000, **4**, 3–26.
31 H. Nan, X. Hu and H. Tian, *Materials Science in Semiconductor Processing*, 2019, **94**, 35–50.
32 J. Liang, C. Wang, Y. Wang, Z. Xu, Z. Lu, Y. Ma, H. Zhu, Y. Hu, C. Xiao, X. Yi, G. Zhu, H. Lv, L. Ma, T. Chen, Z. Tie, Z. Jin and J. Liu, *J. Am. Chem. Soc.*, 2016, **138**, 15829–15832.
33 N. Klipfel, C. Momblona, H. Kanda, N. Shibayama, Y. Nakamura, M. D. Mensi, C. Liu, C. Roldán-Carmona and M. K. Nazeeruddin, *Solar RRL*, 2021, **5**, 2100191.

34 Defect Tolerant Semiconductors for Solar Energy Conversion | The Journal of Physical Chemistry Letters, https://pubs.acs.org/doi/10.1021/jz5001787, (accessed August 12, 2021).
35 R. E. Brandt, V. Stevanović, D. S. Ginley and T. Buonassisi, *MRS Communications*, 2015, **5**, 265–275.
36 Champion Photovoltaic Module Efficiency Chart, https://www.nrel.gov/pv/module-efficiency.html, (accessed August 12, 2021).
37 B. Dou, J. B. Whitaker, K. Bruening, D. T. Moore, L. M. Wheeler, J. Ryter, N. J. Breslin, J. J. Berry, S. M. Garner, F. S. Barnes, S. E. Shaheen, C. J. Tassone, K. Zhu and M. F. A. M. van Hest, *ACS Energy Lett.*, 2018, **3**, 2558–2565.
38 J. B. Whitaker, D. Hoe Kim, B. W. Larson, F. Zhang, J. J. Berry, M. F. A. M. van Hest and K. Zhu, *Sustainable Energy & Fuels*, 2018, **2**, 2442–2449.
39 E. Tenuta, C. Zheng and O. Rubel, *Sci Rep*, 2016, **6**, 37654.
40 G. P. Nagabhushana, R. Shivaramaiah and A. Navrotsky, *PNAS*, 2016, **113**, 7717–7721.
41 S. Yang, H. Zhao, M. Wu, S. Yuan, Y. Han, Z. Liu, K. Guo, S. (Frank) Liu, S. Yang, H. Zhao, S. Yuan, Y. Han, Z. Liu, S. Liu, M. Wu and K. Guo, *Solar Energy Materials and Solar Cells*, 2019, **201**, 110052.
42 G. Grancini, C. Roldán-Carmona, I. Zimmermann, E. Mosconi, X. Lee, D. Martineau, S. Narbey, F. Oswald, F. De Angelis, M. Graetzel and M. K. Nazeeruddin, *Nature Communications*, 2017, **8**, 15684.
43 G. Flora, D. Gupta and A. Tiwari, *Interdiscip Toxicol*, 2012, **5**, 47–58.
44 A. Babayigit, A. Ethirajan, M. Muller and B. Conings, *Nature Materials*, 2016, **15**, 247–251.
45 RS 814.81 - Ordonnance du 18 mai 2005 sur la réduction des risques liés à l'utilisation de substances, de préparations et d'objets particulièrement dangereux (Ordonnance sur la réduction des risques liés aux produits chimiques, ORRChim), https://www.fedlex.admin.ch/eli/cc/2005/478/fr, (accessed August 12, 2021).
46 EUR-Lex - 32002L0095 - EN - EUR-Lex, https://eur-lex.europa.eu/legal-content/en/ALL/?uri=CELEX%3A32002L0095, (accessed August 12, 2021).
47 Total Primary Energy Supply, https://www.ez2c.de/ml/solar_land_area/, (accessed August 12, 2021).
48 Spatial and temporal variability of global surface solar irradiance - NASA Technical Reports Server (NTRS), https://ntrs.nasa.gov/citations/19910068668, (accessed August 12, 2021).
49 J. H. Heo, H. J. Han, D. Kim, T. K. Ahn and S. H. Im, *Energy Environ. Sci.*, 2015, **8**, 1602–1608.
50 M. Szafrański and A. Katrusiak, *J. Phys. Chem. Lett.*, 2016, **7**, 3458–3466.
51 ATSDR - Case Studies in Environmental Medicine, https://www.atsdr.cdc.gov/csem/csem.html, (accessed August 12, 2021).
52 S. L. Postel, G. C. Daily and P. R. Ehrlich, *Science*, 1996, **271**, 785–788.
53 A. Babayigit, D. Duy Thanh, A. Ethirajan, J. Manca, M. Muller, H.-G. Boyen and B. Conings, *Sci Rep*, 2016, **6**, 18721.
54 M. R. Filip and F. Giustino, *PNAS*, 2018, **115**, 5397–5402.
55 S. M. Woodley and R. Catlow, *Nature Mater*, 2008, **7**, 937–946.
56 Y. Wang, J. Lv, L. Zhu and Y. Ma, *Computer Physics Communications*, 2012, **183**, 2063–2070.
57 M. S. Kuklin and A. J. Karttunen, *J. Phys. Chem. C*, 2018, **122**, 24949–24957.
58 National Renewable Energy Laboratory, N.R.E.L., https://www.nrel.gov/pv/assets/pdfs/best-reserch-cell-efficiencies.20190327.pdf.
59 W. Xu, Q. Hu, S. Bai, C. Bao, Y. Miao, Z. Yuan, T. Borzda, A. J. Barker, E. Tyukalova, Z. Hu, M. Kawecki, H. Wang, Z. Yan, X. Liu, X. Shi, K. Uvdal, M. Fahlman, W. Zhang, M. Duchamp, J.-M. Liu, A. Petrozza, J. Wang, L.-M. Liu, W. Huang and F. Gao, *Nature Photonics*, 2019, 1.
60 S. D. Stranks, G. E. Eperon, G. Grancini, C. Menelaou, M. J. P. Alcocer, T. Leijtens, L. M. Herz, A. Petrozza and H. J. Snaith, *Science*, 2013, **342**, 341–344.
61 S. Kazim, M. K. Nazeeruddin, M. Grätzel and S. Ahmad, *Angewandte Chemie International Edition*, 2014, **53**, 2812–2824.
62 W.-J. Yin, T. Shi and Y. Yan, *Appl. Phys. Lett.*, 2014, **104**, 063903.
63 K. X. Steirer, P. Schulz, G. Teeter, V. Stevanovic, M. Yang, K. Zhu and J. J. Berry, *ACS Energy Lett.*, 2016, **1**, 360–366.
64 H. J. Snaith, *J. Phys. Chem. Lett.*, 2013, **4**, 3623–3630.

65 A. Dubey, N. Adhikari, S. Mabrouk, F. Wu, K. Chen, S. Yang and Q. Qiao, *Journal of Materials Chemistry A*, 2018, **6**, 2406–2431.
66 M. I. H. Ansari, A. Qurashi and M. K. Nazeeruddin, *Journal of Photochemistry and Photobiology C: Photochemistry Reviews*, 2018, **35**, 1–24.
67 Y. Jiang, M. R. Leyden, L. Qiu, S. Wang, L. K. Ono, Z. Wu, E. J. Juarez-Perez and Y. Qi, *Advanced Functional Materials*, 2018, **28**, 1870007.
68 Y. Rong, Y. Ming, W. Ji, D. Li, A. Mei, Y. Hu and H. Han, *J. Phys. Chem. Lett.*, 2018, **9**, 2707–2713.
69 F. Mathies, H. Eggers, B. S. Richards, G. Hernandez-Sosa, U. Lemmer and U. W. Paetzold, *ACS Appl. Energy Mater.*, 2018, **1**, 1834–1839.
70 F. Di Giacomo, S. Shanmugam, H. Fledderus, B. J. Bruijnaers, W. J. H. Verhees, M. S. Dorenkamper, S. C. Veenstra, W. Qiu, R. Gehlhaar, T. Merckx, T. Aernouts, R. Andriessen and Y. Galagan, *Solar Energy Materials and Solar Cells*, 2018, **181**, 53–59.
71 S. Mashhoun, Y. Hou, H. Chen, F. Tajabadi, N. Taghavinia, H.-J. Egelhaaf and C. J. Brabec, *Advanced Energy Materials*, 2018, **8**, 1802085.
72 J. A. Christians, P. Schulz, J. S. Tinkham, T. H. Schloemer, S. P. Harvey, B. J. T. de Villers, A. Sellinger, J. J. Berry and J. M. Luther, *Nature Energy*, 2018, **3**, 68.
73 W. Ke and M. G. Kanatzidis, *Nature Communications*, 2019, **10**, 965.
74 F. Hao, C. C. Stoumpos, D. H. Cao, R. P. H. Chang and M. G. Kanatzidis, *Nature Photonics*, 2014, **8**, 489–494.
75 A. E. Maughan, A. M. Ganose, M. M. Bordelon, E. M. Miller, D. O. Scanlon and J. R. Neilson, *J. Am. Chem. Soc.*, 2016, **138**, 8453–8464.
76 M. Chen, M.-G. Ju, A. D. Carl, Y. Zong, R. L. Grimm, J. Gu, X. C. Zeng, Y. Zhou and N. P. Padture, *Joule*, 2018, **2**, 558–570.
77 A. Jodlowski, D. Rodríguez-Padrón, R. Luque and G. de Miguel, *Advanced Energy Materials*, , DOI:10.1002/aenm.201703120.
78 J. Breternitz and S. Schorr, *Advanced Energy Materials*, 2018, **8**, 1802366.
79 L. Schade, A. D. Wright, R. D. Johnson, M. Dollmann, B. Wenger, P. K. Nayak, D. Prabhakaran, L. M. Herz, R. Nicholas, H. J. Snaith and P. G. Radaelli, *ACS Energy Lett.*, 2019, **4**, 299–305.
80 Y. Cai, W. Xie, H. Ding, Y. Chen, K. Thirumal, L. H. Wong, N. Mathews, S. G. Mhaisalkar, M. Sherburne and M. Asta, *Chem. Mater.*, 2017, **29**, 7740–7749.
81 D. Ju, X. Zheng, J. Yin, Z. Qiu, B. Türedi, X. Liu, Y. Dang, B. Cao, O. F. Mohammed, O. M. Bakr and X. Tao, *ACS Energy Lett.*, 2019, **4**, 228–234.
82 A. E. Maughan, A. M. Ganose, M. A. Almaker, D. O. Scanlon and J. R. Neilson, *Chem. Mater.*, 2018, **30**, 3909–3919.
83 T. Takabatake, M. Ishikawa, Y. Nakazawe and K. Koga, *Physica C: Superconductivity*, 1988, **152**, 424–430.
84 T. Komoda and S. Sakata, *J Electron Microsc (Tokyo)*, 1959, **7**, 27–32.
85 R. E. Cohen, *Nature*, 1992, **358**, 136.
86 S. C. Abrahams, J. Ihringer and P. Marsh, *Acta Crystallographica Section B*, 1989, **45**, 26–34.
87 V. M. Goldschmidt, *Naturwissenschaften*, 1926, **14**, 477–485.
88 C. Li, K. C. K. Soh and P. Wu, *Journal of Alloys and Compounds*, 2004, **372**, 40–48.
89 C. Li, X. Lu, W. Ding, L. Feng, Y. Gao and Z. Guo, *Acta Cryst B*, 2008, **64**, 702–707.
90 P. Gao, M. Grätzel and M. K. Nazeeruddin, *Energy & Environmental Science*, 2014, **7**, 2448–2463.
91 G. Kieslich, S. Sun and A. K. Cheetham, *Chemical Science*, 2015, **6**, 3430–3433.
92 M. T. Anderson, K. B. Greenwood, G. A. Taylor and K. R. Poeppelmeier, *Progress in Solid State Chemistry*, 1993, **22**, 197–233.
93 I. M. Reaney, E. L. Colla and N. Setter, *Jpn. J. Appl. Phys.*, 1994, **33**, 3984.
94 C. Shi, C.-H. Yu and W. Zhang, *Angewandte Chemie International Edition*, 2016, **55**, 5798–5802.
95 G. Volonakis, A. A. Haghighirad, R. L. Milot, W. H. Sio, M. R. Filip, B. Wenger, M. B. Johnston, L. M. Herz, H. J. Snaith and F. Giustino, *J. Phys. Chem. Lett.*, 2017, **8**, 772–778.
96 H. D. Megaw, *Proc. Phys. Soc.*, 1946, **58**, 133–152.
97 ICSD - Details on Search Result, https://icsd.fiz-karlsruhe.de/display/details.xhtml, (accessed March 14, 2019).

98 R. D. Shannon, *Acta Cryst A*, 1976, **32**, 751–767.
99 H. Boysen and A. W. Hewat, *Acta Cryst B*, 1978, **34**, 1412–1418.
100 T. B. Brill, R. C. Gearhart and W. A. Welsh, *Journal of Magnetic Resonance (1969)*, 1974, **13**, 27–37.
101 H. Henke, *Zeitschrift für Kristallographie*, 2009, **222**, 477–486.
102 I. P. Swainson, B. M. Powell and R. D. Weir, *Journal of Solid State Chemistry*, 1997, **131**, 221–230.
103 W. Abriel, *Materials Research Bulletin*, 1983, **18**, 1419–1423.
104 W. L. Jolly, *Preparative Inorganic Reactions*, Interscience Publishers, 1964, vol. 1.
105 S. R. Taylor, *Geochimica et Cosmochimica Acta*, 1964, **28**, 1273–1285.
106 W. Travis, E. N. K. Glover, H. Bronstein, D. O. Scanlon and R. G. Palgrave, *Chemical Science*, 2016, **7**, 4548–4556.
107 A. R. Verma and P. Krishna, *Polymorphism and polytypism in crystals*, Wiley, 1966.
108 P. K. Panda and B. Sahoo, *Ferroelectrics*, 2015, **474**, 128–143.
109 T. He, Q. Huang, A. P. Ramirez, Y. Wang, K. A. Regan, N. Rogado, M. A. Hayward, M. K. Haas, J. S. Slusky, K. Inumara, H. W. Zandbergen, N. P. Ong and R. J. Cava, *Nature*, 2001, **411**, 54–56.
110 C. Sun, Z. Gao, H. Liu, L. Wang, Y. Deng, P. Li, H. Li, Z.-H. Zhang, C. Fan and W. Bi, *Chem. Mater.*, 2019, **31**, 5116–5123.
111 A. R. Oganov, C. J. Pickard, Q. Zhu and R. J. Needs, *Nature Reviews Materials*, 2019, **4**, 331–348.
112 J. Graser, S. K. Kauwe and T. D. Sparks, *Chem. Mater.*, 2018, **30**, 3601–3612.
113 K. Kim, B.-C. Zhou and C. Wolverton, *Acta Materialia*, 2018, **145**, 337–346.
114 T. Yamashita, N. Sato, H. Kino, T. Miyake, K. Tsuda and T. Oguchi, *Phys. Rev. Materials*, 2018, **2**, 013803.
115 P. V. Balachandran, A. A. Emery, J. E. Gubernatis, T. Lookman, C. Wolverton and A. Zunger, *Phys. Rev. Materials*, 2018, **2**, 043802.
116 R. Vargas, A. Mosavi and R. Ruiz, *Deep learning: A review*, 2017.
117 K. Ryan, J. Lengyel and M. Shatruk, *J. Am. Chem. Soc.*, 2018, **140**, 10158–10168.
118 K. T. Schütt, H. E. Sauceda, P.-J. Kindermans, A. Tkatchenko and K.-R. Müller, *J. Chem. Phys.*, 2018, **148**, 241722.
119 Q. Xu, Z. Li, M. Liu and W.-J. Yin, *J. Phys. Chem. Lett.*, 2018, **9**, 6948–6954.
120 G. Pilania, P. V. Balachandran, C. Kim and T. Lookman, *Front. Mater.*, , DOI:10.3389/fmats.2016.00019.
121 D. Turaga, F. Nargesian, H. Samulowitz, U. Khurana and E. B. Khalil, 2017, 2529–2535.
122 D. C. Elton, Z. Boukouvalas, M. D. Fuge and P. W. Chung, *Mol. Syst. Des. Eng.*, 2019, **4**, 828–849.
123 H. Wang, Z. Lei, X. Zhang, B. Zhou and J. Peng, *Energy Conversion and Management*, 2019, **198**, 111799.
124 Z. Zhao, P. Zheng, S. Xu and X. Wu, *IEEE Transactions on Neural Networks and Learning Systems*, 2019, **30**, 3212–3232.
125 S. Feng, H. Zhou and H. Dong, *Materials & Design*, 2019, **162**, 300–310.
126 K. Pasupa and W. Sunhem, in *2016 8th International Conference on Information Technology and Electrical Engineering (ICITEE)*, 2016, pp. 1–6.
127 A. Fedorovskiy, project "BTF_ABX3", GitHub repository, https://github.com/AlexanderFedorovskiy/BTF_ABX3, (accessed December 29, 2020).
128 R. Ouyang, *Chem. Mater.*, 2020, **32**, 595–604.
129 R. P. Iczkowski and J. L. Margrave, *J. Am. Chem. Soc.*, 1961, **83**, 3547–3551.
130 B. Cordero, V. Gómez, A. E. Platero-Prats, M. Revés, J. Echeverría, E. Cremades, F. Barragán and S. Alvarez, *Dalton Trans.*, 2008, 2832–2838.
131 *Nat Energy*, 2019, **4**, 1–1.
132 J. Jeong, M. Kim, J. Seo, H. Lu, P. Ahlawat, A. Mishra, Y. Yang, M. A. Hope, F. T. Eickemeyer, M. Kim, Y. J. Yoon, I. W. Choi, B. P. Darwich, S. J. Choi, Y. Jo, J. H. Lee, B. Walker, S. M. Zakeeruddin, L. Emsley, U. Rothlisberger, A. Hagfeldt, D. S. Kim, M. Grätzel and J. Y. Kim, *Nature*, 2021, **592**, 381–385.
133 C. Zhang, D.-B. Kuang and W.-Q. Wu, *Small Methods*, 2020, **4**, 1900662.
134 K. Zhang, N. Zhu, M. Zhang, L. Wang and J. Xing, *J. Mater. Chem. C*, 2021, **9**, 3795–3799.
135 C. Duan, Z. Zhao and L. Yuan, *IEEE Journal of Photovoltaics*, 2021, 1–10.

136 L. Zhu, Q. Lu, C. Li, Y. Wang and Z. Deng, *Chinese Chemical Letters*, 2021, **32**, 2259–2262.
137 S. Shao, J. Dong, H. Duim, G. H. ten Brink, G. R. Blake, G. Portale and M. A. Loi, *Nano Energy*, 2019, **60**, 810–816.
138 Fernelius, W., *Inorganic Syntheses*, McGraw-Hill Book Company Inc., New-York, 1st edn., 1946, vol. 2.
139 I. B. Gorrell, Masters, Durham University, 1983.
140 T. V. Sedakova and A. G. Mirochnik, *Opt. Spectrosc.*, 2016, **120**, 268–273.
141 T. V. Sedakova and A. G. Mirochnik, *Opt. Spectrosc.*, 2015, **119**, 54–58.
142 A. A. Dotsenko, V. I. Vovna, V. V. Korochentsev, A. G. Mirochnik, O. L. Shcheka, T. V. Sedakova and V. I. Sergienko, *Inorg. Chem.*, 2019, **58**, 6796–6803.
143 ICSD -, https://icsd.fiz-karlsruhe.de/index.xhtml, (accessed August 13, 2021).
144 L. Yang and B. Kruse, *J. Opt. Soc. Am. A, JOSAA*, 2004, **21**, 1933–1941.
145 A. R. Zanatta, *Sci Rep*, 2019, **9**, 11225.
146 J. I. Pankove and D. A. Kiewit, *J. Electrochem. Soc.*, 1972, **119**, 156Ca.
147 I. Vázquez-Fernández, S. Mariotti, O. S. Hutter, M. Birkett, T. D. Veal, T. D. C. Hobson, L. J. Phillips, L. Danos, P. K. Nayak, H. J. Snaith, W. Xie, M. P. Sherburne, M. Asta and K. Durose, *Chem. Mater.*, 2020, **32**, 6676–6684.
148 S. Syoyama, K. Osaki and S. Kusanagi, *Inorganic and Nuclear Chemistry Letters*, 1972, **8**, 181–184.
149 V. I. Sidey, O. V. Zubaka, A. M. Solomon, S. V. Kun and E. Yu. Peresh, *Journal of Alloys and Compounds*, 2004, **367**, 115–120.
150 W. Abriel, *Materials Research Bulletin*, 1982, **17**, 1341–1346.
151 K. Małetka, P. Fischer, A. Murasik and W. Szczepaniak, *J Appl Cryst*, 1992, **25**, 1–5.
152 W. A. Andre du Bois, *Zeitschrift für Naturforschung - Section B*, **44**, 1187–1194.
153 K. Maz.xl;letka, R. Tellgren, H. Rundlöf, W. Szczepaniak and L. Rycerz, *Solid State Ionics*, 1996, **90**, 67–74.
154 S. V. Kryuchkov, M. S. Grigor'ev, A. F. Kuzina and V. I. Spitsyn, *Zhurnal Neorganicheskoj Khimii*, 1987, **32**, 2944–2947.
155 G. Thiele, C. Mrozek, D. Kämmerer and K. Wittmann, *Zeitschrift für Naturforschung B*, 2014, **38**, 905–910.
156 R. González, R. Chiozzone, C. Kremer, G. De Munno, F. Nicolò, F. Lloret, M. Julve and J. Faus, *Inorg. Chem.*, 2003, **42**, 2512–2518.
157 W. Werker, *Recueil des Travaux Chimiques des Pays-Bas*, 1939, **58**, 257–258.
158 L. M. Manojlovic, *Bull. Inst. Nuclear Sci.*
159 D. Sinram, C. Brendel and B. Krebs, *Inorganica Chimica Acta*, 1982, **64**, L131–L132.
160 C. C. Stoumpos, C. D. Malliakas and M. G. Kanatzidis, *Inorg. Chem.*, 2013, **52**, 9019–9038.
161 A. E. Maughan, A. M. Ganose, A. M. Candia, J. T. Granger, D. O. Scanlon and J. R. Neilson, *Chem. Mater.*, 2018, **30**, 472–483.
162 B. Schüpp, P. Heines and H.-L. Keller, *Zeitschrift für anorganische und allgemeine Chemie*, 2000, **626**, 202–207.
163 B. Schüpp, P. Heines, A. Savin and H.-L. Keller, *Inorg. Chem.*, 2000, **39**, 732–735.
164 K. W. Bagnall, R. W. M. D'Eye and J. H. Freeman, *J. Chem. Soc.*, 1956, **0**, 3385–3389.
165 A. K. Das and I. D. Brown, *Can. J. Chem.*, 1966, **44**, 939–943.
166 A. Bogacz, J. Bros, M. Gaune-Escard, A. W. Hewat and J. C. Taylor, *J. Phys. C: Solid State Phys.*, 1980, **13**, 5273–5278.
167 K. Małetka, E. Ressouche, H. Rundlöf, R. Tellgren, R. Delaplane, W. Szczepaniak and M. Zabłocka-Malicka, *Solid State Ionics*, 1998, **106**, 55–69.
168 K. W. Bagnall, R. W. M. D'Eye and J. H. Freeman, *J. Chem. Soc.*, 1955, **0**, 3959–3963.
169 W. Abriel and J. Ihringer, *Journal of Solid State Chemistry*, 1984, **52**, 274–280.
170 V. M. Vdovenko, I. I. Kozhina, I. G. Suglobova and D. E. Chirkst, *Radiokhimiya*, 1973, **15**, 54–57.
171 K. Maletka, E. Ressouche, W. Szczepaniak, L. Rycerz and A. Murasik, Neutron Diffraction Studies of Me2UX6 Ionic Conductors, https://www.scientific.net/MSF.228-231.711, (accessed March 14, 2019).
172 I. D. Brown, *Can. J. Chem.*, 1964, **42**, 2758–2767.

173 J. a. A. Ketelaar, A. A. Rietdijk and C. H. van Staveren, *Recueil des Travaux Chimiques des Pays-Bas*, 1937, **56**, 907–908.
174 T. Higashi, S. Syoyama and K. Osaki, *Acta Cryst B*, 1979, **35**, 144–146.
175 *Zeitschrift für Kristallographie - Crystalline Materials*, 2010, **212**, 53–53.
176 Y.-Q. Zheng, K. Peters and H. G. von Schnering, *Zeitschrift fur Kristallographie*, 1997, **212**, 55–55.
177 D. H. Templeton and C. H. Dauben, *J. Am. Chem. Soc.*, 1951, **73**, 4492–4493.
178 H. D. Grundy and I. D. Brown, *Can. J. Chem.*, 1970, **48**, 1151–1154.
179 J. D. McCullough, *Zeitschrift für Kristallographie - Crystalline Materials*, 2015, **94**, 143–149.
180 A. Ferrari and L. Coghi, *Gazzetta Chimica Italiana*, 1941, 440–445.
181 P. Stoll, Doctoral Thesis, ETH Zurich, 1926.
182 N. Sakai, A. A. Haghighirad, M. R. Filip, P. K. Nayak, S. Nayak, A. Ramadan, Z. Wang, F. Giustino and H. J. Snaith, *J. Am. Chem. Soc.*, 2017, **139**, 6030–6033.
183 W. Abriel and M. A. White, *J. Chem. Phys.*, 1990, **93**, 8321–8327.
184 M. Simon and G. Meyer, *European Journal of Solid State and Inorganic Chemistry*, 1997, **34**, 73–84.
185 J. Jander, H. Machatzke and D. Mecke, *Zeitschrift für anorganische und allgemeine Chemie*, 1958, **294**, 181–182.
186 L. Sieg, *Zeitschrift für anorganische und allgemeine Chemie*, 1932, **207**, 93–96.
187 W. Abriel, *Zeitschrift für Naturforschung B*, 2014, **42**, 415–420.
188 G. Engel, *Zeitschrift für Kristallographie - Crystalline Materials*, 2015, **90**, 341–373.
189 T. Kaatz and M. Marcovich, *Acta Cryst*, 1966, **21**, 1011–1011.
190 S. Siegel, *Acta Cryst*, 1956, **9**, 827–827.
191 P. J. Bendall, A. N. Fitch and B. E. F. Fender, *J Appl Cryst*, 1983, **16**, 164–170.
192 T. Schleid, G. Meyer and L. R. Morss, *Journal of the Less Common Metals*, 1987, **132**, 69–77.
193 G. Engel, *Naturwissenschaften*, 1933, **21**, 704–704.
194 M. Webster and P. H. Collins, *Journal of the Chemical Society, Dalton Transactions*, 1973, **0**, 588–594.
195 L. Jongen and G. Meyer, *Acta Cryst E*, 2004, **60**, i91–i92.
196 H. Yun and G.-J. Jang, *Acta Cryst E*, 2007, **63**, i22–i23.
197 Crystal structure of dipotassium hexachlorotungstate(IV), K2[WCl6], https://www.degruyter.com/view/j/ncrs.2005.220.issue-3/ncrs.2005.220.3.323/ncrs.2005.220.3.323.xml, (accessed January 25, 2019).
198 Y.-Q. Zheng, J. Nuss and H. G. von Schnering, *Zeitschrift für Kristallographie - New Crystal Structures*, 1998, **213**, 500–500.
199 P. Wang, W. Xu and Y.-Q. Zheng, *Zeitschrift für Kristallographie - New Crystal Structures*, 2002, **217**, 301–301.
200 P. Wang, W. Xu and Y.-Q. Zheng, *Zeitschrift für Kristallographie - New Crystal Structures*, 2003, **218**, 25–25.
201 A. J. Edwards, R. D. Peacock and A. Said, *J. Chem. Soc.*, 1962, **0**, 4643–4648.
202 J. Beck and M. Hengstmann, *Zeitschrift für anorganische und allgemeine Chemie*, 1998, **624**, 1943–1950.
203 B. Hu, P. Wang, Y. Xiao and L.-P. Song, *Zeitschrift für Kristallographie - New Crystal Structures*, 2005, **220**, 318–318.
204 M. Elder, J. E. Fergusson, G. J. Gainsford, J. H. Hickford and B. R. Penfold, *J. Chem. Soc. A*, 1967, **0**, 1423–1425.
205 J. Martínez-Lillo, D. Armentano, G. De Munno, F. Lloret, M. Julve and J. Faus, *Crystal Growth & Design*, 2006, **6**, 2204–2206.
206 B. Aminoff, *Zeitschrift fuer Kristallographie*, 1936, 246–248.
207 G. Sperka and F. A. Maunter, *Crystal Research and Technology*, 1988, **23**, K109–K111.
208 R. K. Coll, S. E. Fergusson, B. R. Penfold, D. A. Rankin and W. T. Robinson, *Inorganica Chimica Acta*, 1990, **177**, 107–114.
209 R. J. Williams, D. R. Dillin and W. O. Milligan, *Acta Cryst B*, 1973, **29**, 1369–1372.
210 J. Schefer, D. Schwarzenbach, P. Fischer, T. Koetzle, F. K. Larsen, S. Haussühl, M. Rüdlinger, G. McIntyre, H. Birkedal and H.-B. Bürgi, *Acta Cryst B*, 1998, **54**, 121–128.

211 H. Takazawa, S. Ohba and Y. Saito, *Acta Cryst B*, 1988, **44**, 580–585.
212 J. R. Hester, E. N. Maslen, N. Spadaccini, N. Ishizawa and Y. Satow, *Acta Cryst B*, 1993, **49**, 967–973.
213 J. A. Bland and S. N. Flengas, *Can. J. Phys.*, 1961, **39**, 941–944.
214 P. C. Moews, *Inorg. Chem.*, 1966, **5**, 5–8.
215 R. A. Lalancette, N. Elliott and I. Bernal, *Journal of Crystal and Molecular Structure*, 1972, **2**, 143–149.
216 A. W. Laubengayer, O. B. Billings and A. E. Newkirk, *J. Am. Chem. Soc.*, 1940, **62**, 546–548.
217 W. H. Zachariasen, *Acta Cryst*, 1948, **1**, 265–268.
218 A. Grzechnik, M. Fechtelkord, W. Morgenroth, J. M. Posse and K. Friese, *J. Phys.: Condens. Matter*, 2007, **19**, 266219.
219 A. Grzechnik, C. C. Underwood, J. W. Kolis and K. Friese, *Journal of Fluorine Chemistry*, 2013, **150**, 8–13.
220 L. A. Harris, *Acta Cryst*, 1960, **13**, 502–502.
221 A. Cousson, A. Tabuteau, M. Pagès and M. Gasperin, *Acta Cryst B*, 1979, **35**, 1198–1200.
222 G. Brunton, *Acta Cryst B*, 1969, **25**, 2163–2164.
223 F. H. Kruse, *Journal of Inorganic and Nuclear Chemistry*, 1971, **33**, 1625–1627.
224 Y. Laligant, A. Le Bail, G. Ferey, D. Avignant and J. C. Cousseins, *European Journal of Solid State and Inorganic Chemistry*, 1988, **25**, 551–563.
225 M. Josse, M. El-Ghozzi, D. Avignant, G. André and F. Bourée, *Journal of Solid State Chemistry*, 2007, **180**, 1623–1635.
226 A. Grzechnik and J.-Y. Gesland, *Zeitschrift für Kristallographie - New Crystal Structures*, 2003, **218**, 3–4.
227 R. Hoppe and W. Dähne, *Naturwissenschaften*, 1960, **47**, 397–397.
228 G. Brunton, *Acta Cryst B*, 1973, **29**, 2294–2296.
229 R. Hoppe and B. Mehlhorn, *Zeitschrift für anorganische und allgemeine Chemie*, 1976, **425**, 200–208.
230 A. V. Gerasimenko, I. A. Tkachenko, V. Ya. Kavun, N. A. Didenko and V. I. Sergienko, *Russ. J. Inorg. Chem.*, 2006, **51**, 9–22.
231 H. Bode and G. Teufer, *Acta Cryst*, 1956, **9**, 929–933.
232 H. Bode, *Acta Crystallographica*, 1954, **7**, 35.
233 H. Bode and G. Teufer, *Zeitschrift für anorganische und allgemeine Chemie*, 1956, **283**, 18–25.
234 C. C. Underwood, C. D. McMillen, H. Chen, J. N. Anker and J. W. Kolis, *Inorg. Chem.*, 2013, **52**, 237–244.
235 E. Weise and W. Klemm, *Zeitschrift für anorganische und allgemeine Chemie*, 1953, **272**, 211–220.
236 G. Benner and R. Hoppe, *Journal of Fluorine Chemistry*, 1990, **48**, 219–227.
237 Ch. Hebecker, H. G. von Schnering and R. Hoppe, *Naturwissenschaften*, 1966, **53**, 154–154.
238 J.-H. Chang and J. Köhler, *Materials Research Bulletin*, 2000, **35**, 25–32.
239 Mm. J. Durand, J. L. Galigne and A. Lari-Lavassani, *Journal of Solid State Chemistry*, 1976, **16**, 157–160.
240 L. J. Downie, C. Black, E. I. Ardashnikova, C. C. Tang, A. N. Vasiliev, A. N. Golovanov, P. S. Berdonosov, V. A. Dolgikh and P. Lightfoot, *CrystEngComm*, 2014, **16**, 7419–7425.
241 M. B. de Bournonville, D. Bizot, J. Chassaing and M. Quarton, *Journal of Solid State Chemistry*, 1986, **62**, 212–219.
242 J. Chassaing, M. B. D. Bournonville, D. Bizot and M. Quarton, *ChemInform*, , DOI:10.1002/chin.199125038.
243 W. H. Baur, *Acta Cryst B*, 1994, **50**, 141–146.
244 G. Brunton, *Materials Research Bulletin*, 1971, **6**, 555–560.
245 S. M. Balasekaran, M. Molski, J. Spandl, A. Hagenbach, R. Alberto and U. Abram, *Inorg. Chem.*, 2013, **52**, 7094–7099.
246 G. R. Clark and D. R. Russell, *Acta Cryst B*, 1978, **34**, 894–895.
247 J. Louis-Jean, S. Mariappan Balasekaran, D. Smith, A. Salamat, C. T. Pham and F. Poineau, *Acta Cryst E*, 2018, **74**, 646–649.

248 H. Fitz, B. G. Müller, O. Graudejus and N. Bartlett, *Zeitschrift für anorganische und allgemeine Chemie*, 2002, **628**, 133–137.
249 A. I. Smolentsev, A. I. Gubanov, D. Y. Naumov and A. M. Danilenko, *Acta Cryst E*, 2007, **63**, i200–i200.
250 A. I. Smolentsev, A. I. Gubanov, D. Y. Naumov and A. M. Danilenko, *Acta Cryst E*, 2007, **63**, i201–i201.
251 H. Henkel and R. Hoppe, *Zeitschrift für anorganische und allgemeine Chemie*, 1968, **359**, 160–177.
252 S. V. Zemskov, V. D. Zamozhskii, Yu. I. Mironov, V. N. Mitkin and S. P. Gabuda, *Zhurnal Strukturnoi Khimii*, 1980, **21**, 156–161.
253 D. P. Mellor and N. C. Stephenson, *Aust. J. Chem.*, 1951, **4**, 406–411.
254 L. Große and R. Hoppe, *Naturwissenschaften*, 1982, **69**, 447–447.
255 O. Graudejus, A. P. Wilkinson, L. C. Chacón and N. Bartlett, *Inorg. Chem.*, 2000, **39**, 2794–2800.
256 N. Bartlett and J. W. Quail, *J. Chem. Soc.*, 1961, **0**, 3728–3732.
257 G. Siebert and R. Hoppe, *Zeitschrift für anorganische und allgemeine Chemie*, 1972, **391**, 113–116.
258 S. Kaskel and J. Strähle, *Zeitschrift für anorganische und allgemeine Chemie*, 1997, **623**, 1259–1263.
259 J. Portier, A. Tressaud, F. Menil, J. Claverie, R. De Pape and P. Hagenmuller, *Journal of Solid State Chemistry*, 1969, **1**, 100–102.
260 *Zeitschrift für Kristallographie - Crystalline Materials*, 2010, **175**, 269–276.
261 C. Cipriani, *Period. Mineral*, 1955, **24**, 361–376.
262 J. A. Ibers and C. H. Holm, *Acta Cryst*, 1957, **10**, 139–140.
263 O. Göbel, *Acta Cryst C*, 2000, **56**, 521–522.
264 V. Wilhelm and R. Hoppe, *Zeitschrift für anorganische und allgemeine Chemie*, 1974, **405**, 193–196.
265 Hinteregger, W. Wurst, Niederwieser, H. Heymann and Huppertz, *Zeitschrift für Kristallographie – Crystalline Materials*, 2014, **229**, 77–82.
266 S. Nakhal, D. Weber and M. Lerch, *Zeitschrift für Naturforschung B*, 2014, **68**, 121–126.
267 R. M. Metzger, N. E. Heimer, C. S. Kuo, R. F. Williamson and W. O. J. Boo, *Inorg. Chem.*, 1983, **22**, 1060–1064.
268 K. Waltersson, K. A. Wilgelmi, A. Carpy and J. Galy, *Waltersson Bulletin de la Societe Francaise de Mineralogie et de Cristallographie*, 1974, **97**, 13–17.
269 A. Zalkin, D. Eimerl and S. P. Velsko, *Acta Cryst C*, 1988, **44**, 2050–2051.
270 B. V. Bukvetskii, A. V. Gerasimenko and R. L. Davidovich, *Koordinatsionnaya Khimiya*, 1991, **17**, 35–43.
271 Z. Tun and I. D. Brown, *Acta Cryst B*, 1982, **38**, 1792–1794.
272 A. Zalkin, J. D. Forrester and D. H. Templeton, *Acta Cryst*, 1964, **17**, 1408–1412.
273 D. Babel, in *Structure and Bonding*, eds. C. K. Jørgensen, J. B. Neilands, R. S. Nyholm, D. Reinen and R. J. P. Williams, Springer Berlin Heidelberg, 1967, pp. 1–87.
274 W. Zhang, Q. Jing, Y. Fang and Z. Chen, *Zeitschrift für anorganische und allgemeine Chemie*, 2017, **643**, 1739–1743.
275 C. Cipriani, *Rendiconti della Societa Mineralogica Italiana*, 1955, **11**, 58–77.
276 R. Hoppe, W. Liebe and W. Dähne, *Zeitschrift für anorganische und allgemeine Chemie*, 1961, **307**, 276–289.
277 J. L. Hoard and W. B. Vincent, *J. Am. Chem. Soc.*, 1939, **61**, 2849–2852.
278 H. Bode and R. Brockmann, *Zeitschrift für anorganische und allgemeine Chemie*, 1952, **269**, 173–178.
279 J. Portier, F. Menil and J. Grannec, *Comptes Rendus des Seances de l'Academie des Sciences, Serie C: Sciences Chimiques*, 1969, **269**, 327–330.
280 *Zeitschrift für anorganische und allgemeine Chemie*, 1990, **582**, 111–120.
281 *Zeitschrift für Kristallographie - New Crystal Structures*, 2001, **216**, 20–20.
282 I. N. Flerov, A. V. Kartashev, M. V. Gorev, E. V. Bogdanov, S. V. Mel'nikova, M. S. Molokeev, E. I. Pogoreltsev and N. M. Laptash, *Journal of Fluorine Chemistry*, 2016, **183**, 1–9.
283 B. K. Vainshtein and R. N. Kurdyumova, *Kristallografiya*, 1958, **3**, 29–31.
284 O. F. Göbel, E. J. E. ten and J. Smits, *Zeitschrift für Kristallographie Crystalline Materials*, 2011, **226**, 531–534.

285 H. Bode and W. Wendt, *Zeitschrift für anorganische und allgemeine Chemie*, 1952, **269**, 165–172.
286 R. Hoppe and B. Hofmann, *Zeitschrift für anorganische und allgemeine Chemie*, 1977, **436**, 65–74.
287 P. Bukovec and R. Hoppe, *Journal of Fluorine Chemistry*, 1988, **38**, 107–114.
288 J. A. A. Ketelaar, *Zeitschrift für Kristallographie - Crystalline Materials*, 2015, **92**, 155–156.
289 J. H. Loehlin, *Acta Cryst C*, 1984, **40**, 570–570.
290 C. M. Gramaccioli and I. Campostrini, *The Canadian Mineralogist*, 2007, **45**, 1275–1280.
291 P. Bukovec and R. Hoppe, *Journal of Fluorine Chemistry*, 1983, **23**, 579–587.
292 F. Averdunk and R. Hoppe, *Journal of Fluorine Chemistry*, 1990, **47**, 481–488.
293 W. B. Vincent and J. L. Hoard, *J. Am. Chem. Soc.*, 1942, **64**, 1233–1234.
294 *Zeitschrift für Kristallographie - Crystalline Materials*, 2010, **175**, 159–164.
295 M. Bork and R. Hoppe, *Zeitschrift für anorganische und allgemeine Chemie*, 1996, **622**, 417–424.
296 J. C. Taylor and P. W. Wilson, *Journal of Inorganic and Nuclear Chemistry*, 1974, **36**, 1561–1563.
297 A comparison of profile decomposition and Rietveld methods for structural refinement with powder diffraction data, https://www.degruyter.com/view/j/zkri.1987.181.issue-1-4/zkri.1987.181.1-4.151/zkri.1987.181.1-4.151.xml, (accessed March 15, 2019).
298 H. Bode and E. Voss, *Zeitschrift für anorganische und allgemeine Chemie*, 1956, **286**, 136–141.
299 R. W. G. Wyckoff and J. H. Mueller, *Am J Sci*, 1927, **Series 5 Vol. 13**, 347–352.
300 M. Tabet, *Gazzetta Chimica Italiana*, 1933, **63**, 679–680.
301 W. Schütz, *Zeitschrift für Physikalische Chemie*, 1936, **31B**, 292–308.
302 J. W. Quail and G. A. Rivett, *Can. J. Chem.*, 1972, **50**, 2447–2450.
303 J. Fawcett, J. H. Holloway, D. C. Puddick and D. R. Russell, *Acta Cryst B*, 1980, **36**, 1921–1922.
304 R. Hoppe and W. Klemm, *Zeitschrift für anorganische und allgemeine Chemie*, 1952, **268**, 364–371.
305 R. M. Bozorth, *J. Am. Chem. Soc.*, 1922, **44**, 1066–1070.
306 E. O. Schlemper, W. C. Hamilton and J. J. Rush, *J. Chem. Phys.*, 1966, **44**, 2499–2505.
307 J. Fábry, J. Chval and V. Petříček, *Acta Cryst E*, 2001, **57**, i90–i91.
308 B. Goßner and O. Kraus, *Zeitschrift für Kristallographie - Crystalline Materials*, 2015, **88**, 223–225.
309 E. O. Schlemper and W. C. Hamilton, *J. Chem. Phys.*, 1966, **45**, 408–409.
310 G. Gou, J. Young, X. Liu and J. M. Rondinelli, *Inorg. Chem.*, 2017, **56**, 26–32.
311 K. Ephraim Babu, N. Murali, K. Vijaya Babu, Paulos Taddesse Shibeshi, and V. Veeraiah, *ACTA PHYSICA POLONICA A*, , DOI:http://dx.doi.org/10.12693/APhysPolA.125.1179.
312 S. V. Syrotyuk and V. M. Shved, *Eur. Phys. J. B*, 2015, **88**, 229.
313 A. N. Vtyurin, S. V. Goryainov, N. G. Zamkova, V. I. Zinenko, A. S. Krylov and S. N. Krylova, *Computational Materials Science*, 2006, **36**, 79–83.
314 A. Horowitz, M. Amit, J. Makovsky, L. B. Dor and Z. H. Kalman, *Journal of Solid State Chemistry*, 1982, **43**, 107–125.
315 M. Harmel, H. Khachai, A. Haddou, R. Khenata, G. Murtaza, B. Abbar, S. Bin Omran, and M. Khalfa, *ACTA PHYSICA POLONICA A*, , DOI:http://dx.doi.org/10.12693/APhysPolA.128.34.
316 M. Midorikawa, Y. Ishibashi and Y. Takagi, *J. Phys. Soc. Jpn.*, 1979, **46**, 1240–1244.
317 R. Demirbilek, A. Ç. Bozdoğan, M. Çalışkan and G. Özen, *physica status solidi (b)*, 2011, **248**, 1723–1726.
318 G. A. Geguzina and V. P. Sakhnenko, *Crystallogr. Rep.*, 2004, **49**, 15–19.
319 G. Pilania and B. P. Uberuaga, *Journal of Applied Physics*, 2015, **117**, 114103.
320 I. Hany, G. Yang, Q. V. Phan and H. J. Kim, *Materials Science in Semiconductor Processing*, 2021, **121**, 105392.
321 R. H. Mitchell, M. D. Welch and A. R. Chakhmouradian, *Mineralogical Magazine*, 2017, **81**, 411–461.
322 J. M. Longo and J. A. Kafalas, *Journal of Solid State Chemistry*, 1971, **3**, 429–433.
323 Y. Fujimoto, M. Koshimizu, T. Yanagida, G. Okada, K. Saeki and K. Asai, *Japanese Journal of Applied Physics*, 2016, **55**, 090301.
324 M. Sarwan, P. Shukla and S. Singh, *AIP Conference Proceedings*, 2020, **2265**, 030341.
325 A. I. Lebedev, *Phys. Solid State*, 2015, **57**, 331–336.
326 M. Andansari, F. Latief, U. Nuraini and S. Suasmoro, *AIP Conference Proceedings*, 2020, **2296**, 020122.
327 A. W. Sleight, *Materials Research Bulletin*, 1969, **4**, 377–380.

328 J. Gong, C.-S. Lee, E.-J. Kim, J.-H. Kim, W. Lee and Y.-S. Chang, *ACS Appl. Mater. Interfaces*, 2017, **9**, 28426–28432.
329 K. Fujita, T. Kawamoto, I. Yamada, O. Hernandez, N. Hayashi, H. Akamatsu, W. Lafargue-Dit-Hauret, X. Rocquefelte, M. Fukuzumi, P. Manuel, A. J. Studer, C. S. Knee and K. Tanaka, *Chem. Mater.*, 2016, **28**, 6644–6655.
330 A. Pialoux and B. Touzelin, *Comptes Rendus de l'Academie des Sciences. Serie 2, Mecanique, Physique, Chimie, Astronomie*, 1996, **323**, 687–693.

Glossary

PSC – perovskite solar cell

IEA – International Energy Agency

IPCC – Intergovernmental Panel on Climate Change

EROI – energy returned on energy invested

PV – photovoltaic

CSP – concentrated solar power

AM – atmospheric mass

HTM – hole transport material

DFT – density functional theory

MD – Molecular dynamics

PCE – power conversion efficiency

EQE – external quantum efficiency

MA – methylammonium

FA – formamidinium

LT – low temperature

ML – machine learning

ANN – artificial neural network

SVM – support vector machine

DL – deep learning

DMF – Dimethylformamid

XRD – X-Ray diffraction

PL – photoluminescence

UV-Vis – ultraviolet-visible

SKM – Schuster-Kubelka-Munk

LR-TDDFT – linear-response time-dependent density functional theory

LFE – local field effects

t – tolerance factor

α – absorption coefficient

R – reflectance coefficient

T – transmission coefficient

Curriculum Vitae

Scientist

Alexander Fedorovskiy

Birthdate: 4 Jan 1994

+41787438424

fedorovskiy.alexander@gmail.com

Key skills:

Applied Science and Engineering: semiconductor and thin-film manufacturing & coating, characterization techniques (AFM, SEM, IR-VIS-near UV spectroscopy, XPS, TGA, etc), CAD, electrical engineering, equipment maintaining.

Software development:

Java (Spring, Vaadin), Python (NumPy, TensorFlow, Keras), MongoDB, Git, Bash

Languages:

English: Fluent

Russian: Native

Summary:

The applied researcher with 5+ years of experience with focus on materials science. Some previous projects:

- Creating deep learning models for crystal formation forecasting
- Full-stack research of novel Tellurium-based halide semiconductor materials for optoelectronics
- Developing web-service for collecting, standardization, and analyzing group experimental data
- Designing, modification, and maintaining various laboratory equipment, including automation tasks

Education:

Nov.2017-Oct.2021, **Doctoral** School of Materials Science and Engineering, École polytechnique fédérale de Lausanne (EPFL), Lausanne, Switzerland.

Ph.D.'s thesis: Investigation of Lead-free perovskites for Optoelectronic Application.

Sept.2015-July 2017 Department of Modern Functional Materials, Department of Laser and Light Engineering, ITMO University, Saint Petersburg, Russia. **Master's degree in Technical Physics**.

Master's thesis: Nanotribology modification of GaAs epitaxial layers.

Sept.2011-July 2015 Department of Technical Physics, Faculty of Physics, Southern Federal University, Rostov-na-Donu, Russia. **Bachelor of Science in Physics**.

Bachelor's thesis: The frequency dependence in the piezoresponse force microscopy of the dense piezoelectric ceramics surface.

Employment:

Nov.2017-present **Doctoral assistant** in Institute of Chemical Sciences and Engineering, Group for molecular engineering of functional materials, École Polytechnique Fédérale de Lausanne (EPFL), Sion, Switzerland.

Feb 2016-May 2017 **Laboratory assistant** in Centre of Nanoheterostructure Physics, Ioffe Institute, Saint Petersburg, Russia.

Internships:

January 2017-April 2017, C2N, CNRS, Université Paris-Sud et Université Paris-Saclay, France.

March 2016-June 2016, Institut des nanosciences de Paris, Université Pierre et Marie Curie, Paris, France.

Publications:

Fedorovskiy, A. E., Queloz, V. I. E., & Nazeeruddin, M. K. (2021). Beyond Tolerance Factor: Using Deep Learning for prediction Formability of ABX3 Perovskite Structures. *Advanced Theory and Simulations, https://doi.org/10.1002/adts.202100021*

Fedorovskiy, A. E., Drigo, N. A., & Nazeeruddin, M. K. (2020). The role of Goldschmidt's tolerance factor in the formation of A2BX6 double halide perovskites and its optimal range. *Small Methods, https://doi.org/10.1002/smtd.201900426*

Queloz, V. I., Bouduban, M. E., García-Benito, I., **Fedorovskiy, A.**, Orlandi, S., Cavazzini, M., ... & Grancini, G. (2020). Spatial charge separation as the origin of anomalous stark effect in fluorous 2d hybrid perovskites. *Advanced functional materials, https://doi.org/10.1002/adfm.202000228*

Bunin, M. A., Rybyanets, A. N., Naumenko, A. A., Sukhomlinov, D. I., & **Fedorovskiy, A. E.** (2015). Piezoelectric Response from Porous Ferroelectric Ceramics at Low Drive Voltage. *Ferroelectrics, https://doi.org/10.1080/00150193.2015.995531*